Angle-Dependent Strong Field Ionization of Oriented Carbonyl Sulfide

Sanjay Khatri

San Jose, CA

B.S. California Polytechnic State University-San Luis Obispo, June 2014

A Dissertation presented to the Graduate Faculty

of the University of Virginia in Candidacy for the Degree of

Doctor of Philosophy

Department of Physics

University of Virginia

May 2022

Abstract

We have developed a method for extracting the angle-dependent single ionization probability of molecules and demonstrated it on carbonyl sulfide (OCS). The method utilizes phase-locked bi-chromatic laser fields to induce orientation via coherent rotational redistribution from non-ionizing Raman and hyper-Raman transitions, and through angle-dependent ionization. These coherent interactions create rotational wavepackets within the ionized molecules and surviving neutrals. A time-delayed intense probe pulse fragments the neutrals and ions via Coulomb explosion, and the delay-dependent S^{+3} yields are used to monitor the field-free evolution of the ionic and neutral rotational wavepackets. The wavepackets exhibit unique rotational revival structure near their characteristic rotational revival times. Using a model that includes the non-ionizing Raman, hyper-Raman, and angle-dependent single ionization interactions, we fit the delay-dependent evolution of the neutral and ionic wavepackets to extract the angle-dependent single ionization rate. More generally, the approach should be directly applicable to measurements of the angle dependence of other strong-field processes, e.g. multiple and dissociative ionization, in molecules.

Contents

List of Figures

List of Tables

Acknowledgements

I have many people to thank for completing my PhD. First and foremost, I want to dedicate this dissertation to my parents, who have been my biggest cheerleaders since arriving in Charlottesville on August 2014. They have supported and encouraged me to pursue my interests. Through the best and most challenging of times, they have always been there for me. Thank you mom and dad for your support.

I also would like to acknowledge Professor Tom Bensky and Kat Gillen at Cal Poly San Luis Obispo, who both inspired me to pursue a PhD in physics. Thank you for listening to me when I would come to your office to discuss physics, careers, and concerns over whether I would even be admitted into graduate school. More people would pursue physics if they had professors like you, so thank you for inspiring me and others.

After working in Bob Jones' lab for the past 7 years, I have learned the true meaning of persistence and perseverance. Completing the work in this dissertation was by far one of the most challenging and rewarding experiences of my life. This dissertation would not have been possible without his guidance and expertise. Thank you Bob for your guidance, as your wisdom and expertise turned seemingly impossible problems into being more manageable to solve.

I would like to thank current and former lab members for their assistance. Thank you Sachin Sharma for being a great friend and member of the lab. I enjoyed yours and Shivani's company, and of course the delicious homemade authentic dosa, channa masala, and paneer! Thank you Ali Azarm for the insightful physics discussions and your help in troubleshooting equipment in the lab. Thank you P*é*ter S*á*ndor for taking the time to discuss your methodologies for performing various laser-based measurements in the lab and your code for simulating molecular alignment. Thanks Chengxing and Lingyun for playing tennis with me. It was a fun way to relieve stress.

I would like to also thank our collaborators at Louisiana State University and the Ohio State University. Thank you Francois Mauger for organizing the collaboration meetings.

Finally, I would like to thank my amazing and beautiful wife, Monisha. I could not have asked for a more supportive wife, who always picked me up and helped me to find the benefit of every challenge I faced throughout my PhD. The best feeling was knowing that after a tough day in the lab or working on simulations that we could chat and take walks around the neighborhood. I look forward to seeing where our

next adventure takes us.

1 Introduction

1.1 Motivation

The creation of ultrashort laser pulses with durations on the order of picosecond (10^{-12} s), femtosecond (10^{-15} s), or more recently attosecond (10^{-18} s) timescales has fueled interest in probing ultrafast dynamics in atoms and molecules. For context, Figure 1.1 shows a cartoon portraying estimates of the various timescales for dynamics in atoms and molecules.

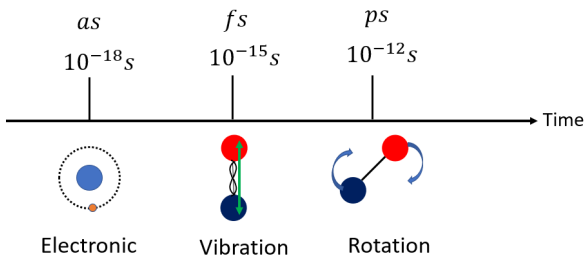

Figure 1.1: Cartoon of the timescale of dynamics in atoms and molecules. Adapted from [1].

With laser pulse durations now entering the attosecond regime, there has been interest in the research community to probe electron dynamics and understand the role ionization plays in initiating or probing these dynamics.

Several experimental studies have shown that controlling the rotational degrees of the freedom with respect to the polarization of a strong ionizing field can vary the ionization probability [2–5]. Methods for creating rotationally controlled molecular ensembles such as aligned (exhibits a preferential order along a space-fixed axis) and oriented (exhibits a preferential direction along a space-fixed axis) molecules will be discussed further in Section 1.4. The difference between molecular alignment and orientation is summarized in Figure 1.2.

Our studies of strong field ionization (SFI) of oriented molecules focus on carbonyl sulfide (OCS). OCS is a linear molecule that has been well studied in the context of laser induced alignment and orientation [2, 3, 6–10]. Previous measurements of SFI of OCS have shown that the primary ionization channels are non-dissociative, simplifying measurements and their comparison with theory. The results of experiments studying SFI of aligned OCS have been well-described by time-dependent density functional theory (TDDFT)

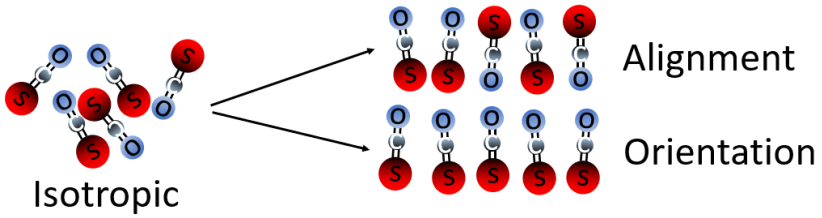

Figure 1.2: Cartoon comparing an isotropic sample with 2 controlled molecular ensembles. Aligned molecules have a definite order with a particular axis aligned to a laboratory fixed axis, but with no preferential direction. Oriented molecules additionally exhibit a preferential direction along a lab-fixed axis.

calculations[4, 5], but those same calculations (assuming linearly polarized laser light) predict an orientation dependence that is opposite to that observed for SFI with circularly polarized light. Obtaining the first measurements of angle-dependent SFI of oriented OCS using linearly polarized laser light, to compare with these previous results, is the central goal of this dissertation.

The next section will introduce ionization mechanisms and consider the influence of ionization on the remaining electrons within a molecular ion.

1.2 Ionization

The information presented in this section regarding ionization of atoms and molecules was adapted from previous PhD students, Kelsie Betsch[11] and Sha Li[12].

Laser-induced ionization of atoms and molecules can occur via two different methods: photoionization and field ionization. For photoionization, the incoming laser can be treated as a flux of photons that have a negligible effect on the structure of an atom or molecule, such that the binding potential is not distorted by their presence as shown in Figure 1.3. For an electron to be removed, the ground state electron must overcome the ionization potential I_p. If a photon has angular frequency ω (and, thus, energy $\hbar\omega$) such that $\hbar\omega \geq I_p$, then the electron can be removed from the atom or molecule upon absorption of that photon. This is known as single photon ionization. If $\hbar\omega < I_p$, then ionization is still possible but requires that the atom or molecule, "simultaneously", absorbs at least n photons so that $n\hbar\omega \geq I_p$. This is known as multiphoton

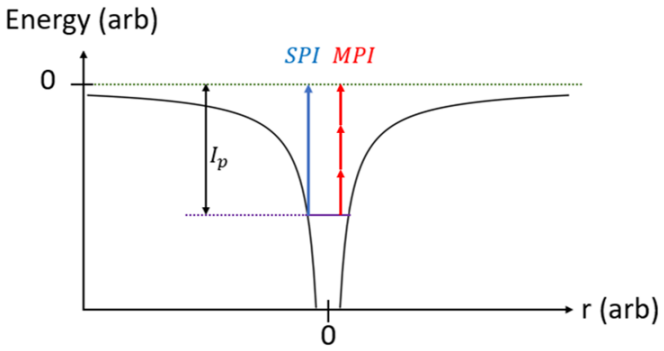

Figure 1.3: A cartoon illustrating the difference between single photon ionization (SPI) and multiphoton ionization (MPI) in an atom. The solid black line shows the binding potential. I_p is the ionization potential. The arrows indicate the number of photons absorbed for the electron to enter the continuum. Adapted from [12].

ionization (MPI) [13].

When the laser becomes sufficiently intense that the net electronic potential is significantly distorted then the interaction with the atom can no longer be treated as perturbative. This is coined the "strong-field" regime, where field-driven ionization can occur as shown in Figure 1.4. The laser's electric field suppresses the binding potential on one side of the atom, which provides a pathway for the electron to tunnel into the continuum. This is known as tunnelling ionization (TI). If the binding potential has been suppressed below the electron's initial energy level, then the electron can directly leave the atom without tunneling. This is known as over-the barrier ionization (OBI), which is also portrayed in Figure 1.4. Unless otherwise stated, atomic units are used throughout this dissertation.

The boundary between multiphoton and tunneling ionization was determined by Leonid Keldysh. He introduced a tunnelling frequency (ω_t) and defined a parameter now known as the Keldysh parameter (γ) [14],

$$\gamma = \frac{\omega}{\omega_t} = \frac{\omega}{F}\sqrt{2I_p} \tag{1}$$

where ω is the angular frequency of the ionizing laser field, F is the strength of the laser field, and I_p is the ionization potential of the atom. The tunneling domain is defined by $\gamma \ll 1$, and multiphoton ionization occurs when $\gamma \gg 1$. Photoionization and field ionization can occur for molecules as well. Unlike atoms, molecules also possess rotational and vibrational degrees of freedom, which can influence the relevant

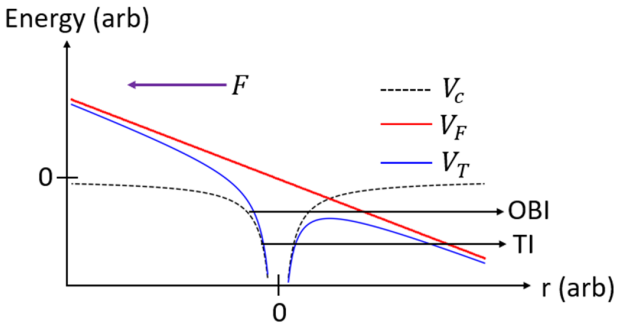

Figure 1.4: A cartoon of the combined potential of an atom and a laser field (V_T, blue solid curve) at the instant of time where the atom experiences the laser field's maximum amplitude. The dashed black curve shows the binding potential of the atom in the absence of the laser field, and r is the electron's position relative to the atom's center along the field axis. The red line shows the electric potential of the laser field (V_F) at one instant in time, where F is the electric field strength of the laser. A laser field of sufficient strength can distort the binding potential such that a bound electron can tunnel (TI) or directly exit over the barrier (OBI) into the continuum. Adapted from [12].

dynamics.

1.2.1 Post-Ionization Processes in Strong Laser Fields

After the electron leaves the molecule, its subsequent trajectory can become dictated by the strong laser field. The interaction has been described by a 3-step model[15–17].

The first step is tunnel ionization, where the electron can tunnel through the potential barrier into the continuum. The second step involves the electron's propagation in the presence of the strong laser field. Upon entering the continuum, the freed electron is accelerated away from the ionic core. For a linearly polarized laser field, once the direction of the field reverses sign and is now directed toward the ionic core, the direction of acceleration changes with it and the electron maybe driven back toward the ionic core. While propagating in the continuum, the electron gains energy from the laser field. The final step is where the electron returns to the ionic core where the following may occur:

1) The electron recombines with the parent ion emitting a photon whose energy is the sum of the kinetic energy gained by the electron in the laser field and the ionization potential. This process is known as high harmonic generation (HHG)[18, 19] depicted in Figure 1.5.

2) The electron elastically scatters off the parent ion.

3) The electron inelastically scatters with the parent ion and causes ionic core excitation and/or emission of additional electrons and/or molecular fragmentation.

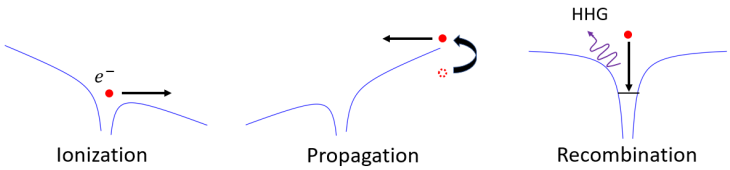

Figure 1.5: A cartoon summarizing the 3-step model, where the final step shows the recombination step in HHG.

Beyond exploring the freed electron's dynamics upon ionization, probing the dynamics of the hole residing in the parent ion has become an active area of research. The ionization process represents the removal of an electron from a molecule, or the creation of a "hole" in the multi-electron wavefunction. This newly created hole can be spatially localized and may not be an eigenstate of the ionic Hamiltonian. In that case, the hole will move about the molecule. The evolution of the hole typically occurs over timescales of one to several femtoseconds. When the hole dynamics are the result of electron correlation, the process is known as charge migration (CM), which should not be confused with charge transfer, i.e. hole dynamics driven by nuclear motion. Charge migration has become a hot topic in recent years with two research groups detecting its impact on multiple ionization and HHG, respectively. [20, 21]. Beyond measuring CM in the laboratory, theoretical research efforts are geared toward understanding the factors that determine how and if CM is initiated through various ionization processes (e.g. strong field ionization of valence electrons vs X-ray photoionization of core electrons) for different types of molecules as well as the characteristics (degree of hole localization and speed of the hole motion) in different molecules. Not surprisingly, the details of the ionization process are important in determining whether charge migration occurs. As an example, our theory collaborators from Louisiana State University (LSU) have performed simulations of hole dynamics in iodotoluene (C_7H_7I)[22] following the removal of an electron. Figure 1.6 illustrates the evolution of a localized hole created on the iodine atom as shown in purple. The hole density oscillates from the iodine atom to the other end of the molecule and back with a period of approximately 2fs.

The details of the hole creation and its degree of spatial localization are believed to be critical param-

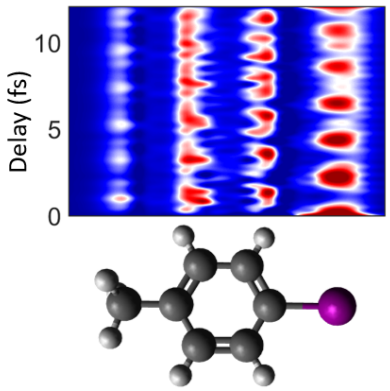

Figure 1.6: A simulation performed by our LSU theory collaborators[22] depicting the hole density as a function of delay after a localized hole is created on the iodine-atom (purple atom on the right) of iodotoluene (C_7H_7I). The red portions highlight areas of higher hole density and show that the hole oscillates back and forth across the molecule.

eters governing the ensuing dynamics[4, 23]. Our experimental efforts have focused on measuring strong field ionization of molecules as a potential mechanism for creating and controlling CM, and as a test of theory used to guide strong-field experiments that aim to view ultrafast hole dynamics in molecules. Unlike atoms, molecules also possess rotational and vibrational degrees of freedom, which can influence the relevant dynamics. In the next section, we explore the sensitivity of the strong field ionization probability on the molecule's rotational degrees of freedom.

1.2.2 Angular Dependence of Strong Field Ionization

For molecules exposed to intense low frequency (near-infrared and below) fields, the single and multiple ionization rates can depend critically on the alignment or orientation of the molecule relative to the direction of the applied field at the instant of ionization[2–5, 23–31]. The ability to control molecular alignment or orientation in the laboratory and accurately simulate the collective electronic response from an intense laser interaction are crucial for exploring ultrafast electronic processes in molecules.

Recall from Figure 1.2 that aligned molecules have a definite order along a space-fixed axis. Oriented molecules also exhibit a preferential direction along that axis. One approach for measuring alignment dependent strong field ionization is to pre-align molecules with a non-ionizing laser pulse and use a second intense short laser pulse to ionize the molecules. By measuring the ionization yield while varying the ionizing laser

polarization direction with respect to the molecular axis, one can determine the alignment-dependent strong field ionization yields. This approach was used by the Stapelfeldt group[5], where their measured results are depicted in Figure 1.7 as green dots. The alternative method used by P. Sandor[4] has a similar two-pulse setup where one pulse induces transient alignment (see Section 1.4.4) and the other produces ionization, but the ionization yield is recorded as a function of delay between the aligning and ionizing pulse. Information regarding the alignment-dependent ionization yields can be extracted from the measured delay-dependent ionization yields (see Section 3.4.1). The results of P. Sandor's measurement is shown in Figure 1.7 as a solid red line. Measurements and calculations of the angular dependence of strong field single ionization of aligned carbonyl sulfide (OCS)[4, 5] are depicted in Figure 1.7a. The measurements indicate a minimum in the ionization probability for an ionizing field polarized along the molecular axis, which resembles the highest occupied molecular orbital (HOMO). However, the maximum ionization probability measured at θ=90° does not match the shape of the HOMO [5]. This difference is attributed to ionization from multiple orbitals [4]. Note that the angle dependent measurements do not divulge the location of the ionized electron

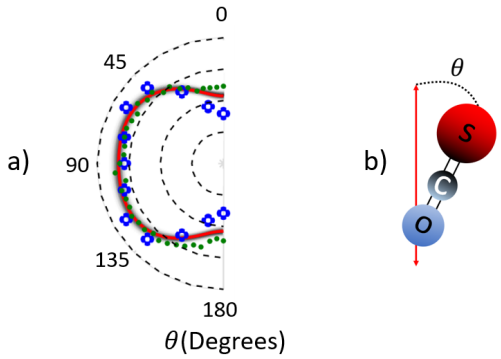

Figure 1.7: a) Single ionization probability of aligned OCS vs θ, the angle between the ionizing laser polarization and the molecular axis. The red solid curve with gray shading is the result of measurements made by P. Sandor at UVa[4]. The blue crosses are time-dependent density functional theory (TDDFT) calculations performed by LSU theory collaborators. The green circles are previous measurements performed by the Stapelfeldt group[5]. Both the simulations and measurements conclude that OCS preferentially ionizes when the molecular axis is perpendicular to the ionizing laser polarization.

from the molecule, only the field direction or axis relative to the molecular frame that produces the most ionization. These angle-dependent measurements performed at UVa (red solid line) and by the Stapelfeldt group (green dots) are in good agreement with simulations (blue crosses) of strong-field single ionization of

OCS performed by our LSU collaborators.

Since the LSU group's theoretical approach based on time-dependent density functional theory (TDDFT) reproduced the experimental results, we employ them to provide additional insight on the charge dynamics that occur in OCS in the presence of an intense, ionizing laser field. Given that hole localization is an important parameter for determining if ultrafast charge migration occurs and its characteristics, the LSU group performed calculations exploring the dependence of hole localization as a function of θ, the angle between the molecular axis and the laser polarization, in strong-field ionized OCS. Their calculation uses a model, that separates the OCS molecule into two centers (S and OC), and the electron densities on the S and OC centers are tracked as the system is driven by a strong 800nm laser field. To determine the degree of hole localization, changes in the electron density due to polarization in the strong ionizing field are carefully modeled and eliminated from the time-dependent electron density. The results of the calculation are shown in Figure 1.8, where the hole portion on the S-atom of OCS is plotted as a function of θ. The calculation shows

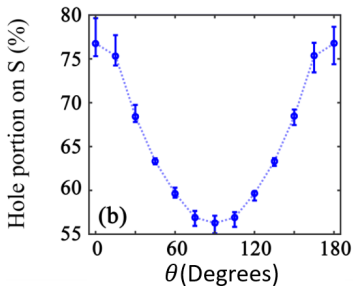

Figure 1.8: Calculation performed by the LSU group of the cycle-averaged portion of the electron hole on the cation S center as a function of θ[4].

that the hole localization exhibits a strong alignment dependence and that the most localized hole is created when the ionizing laser polarization direction and molecular axis of OCS are parallel (θ=0). Interestingly, this is also the angle where the single ionization yield has its lowest probability. The predicted molecular alignment dependence on hole localization on the S-atom demonstrates the impact that strong field ionization could have on the hole creation and its ensuing dynamics.

By tracking the ionization yield with sub-cycle temporal resolution throughout a linearly polarized laser pulse, the LSU group has predicted the full angle-dependent single ionization rate of OCS. Figure 1.9 shows the calculated angle dependent ionization rate at an instant of time where the ionizing 800nm laser field is

pointing upward. Here θ is defined as the angle between the laser polarization and the permanent molecular dipole moment, which points from the center of the molecule toward the S atom. The rate has been normalized so that the angle integrated rate is equal to one. The LSU group's calculations predict a higher

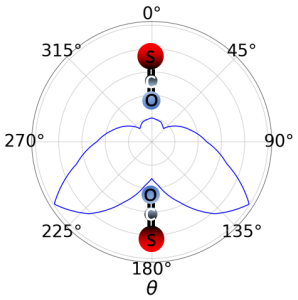

Figure 1.9: TDDFT calculation performed by the LSU group of the angle-dependent single ionization rate of OCS in a linearly polarized 800nm field directed along θ=0. θ is the angle between the laser polarization and the permanent dipole of OCS.[4] The rate has been normalized so that the angle integrated rate is equal to one.

probability of ionization when the ionizing laser field generally opposes the permanent dipole moment (i.e. for $90° < \theta < 270°$). Interestingly, measurements performed by the Stapelfeldt group[32] using a circularly polarized ionizing laser field determined that OCS preferentially ionizes, at times when the laser field was generally aligned with the permanent molecular dipole moment (i.e. for $-90° < \theta < 90°$). The two different results are summarized in Figure 1.10.

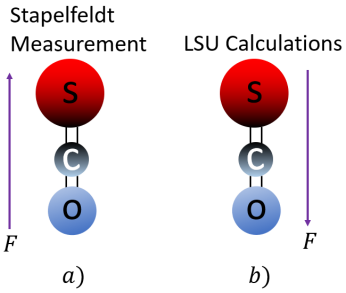

Figure 1.10: Instantaneous Field direction (F) parallel to the molecular axis which produces more OCS^+. a) Stapelfeldt group's measurements using circularly polarized laser pulses. b) TDDFT results from the LSU group for a linearly polarized laser field.

As noted above, the Stapelfeldt group's measurement used a circularly polarized laser field to singly ionize OCS. They then used the momentum imparted to the ionized electrons to determine the direction of

the field at which preferential ionization of the oriented OCS ensemble occurred. Exploiting the transverse momentum transfer to an ionized electron in a circular or elliptically polarized field has become a fairly common approach for determining the field direction or time at which strong-field ionization occurs. The striking difference between the TDDFT calculations and previous measurements could be the result of an error in either the simulations or experiment (although the simulations accurately reproduced the alignment dependent ionization yields), or it could indicate that different non-adiabatic dynamics can play an important role in the strong field ionization with linear vs circularly polarized laser pulses. Accordingly, a primary goal of this dissertation is to measure the angle-dependent strong-field ionization yield for molecules (particularly OCS) in a linearly polarized field.

This dissertation focuses on measurements of the single ionization probability of OCS versus θ. Orienting molecules requires an interaction that defines a preferential direction for the molecular dipole. As with alignment, that orientation can be steady state, based on the rotational energy-level structure in the presence of an external field, or transient, relying on coherent rotational dynamics induced by a short laser pulse. We use ionization in an asymmetric linearly polarized laser pulse (in which the sub-cycle field maxima in one direction are larger than in the other) to preferentially ionize molecules in some orientations over others and, thereby, induce transient orientation. By measuring the time-dependent orientation of the resulting molecular ions and remaining neutrals, we recover the angle-dependent ionization probability.

1.3 Asymmetric Laser Fields

A laser pulse can be decomposed into 2 pieces: a carrier wave, which oscillates at the central frequency and the envelope, which sets the shape of the pulse. The time-dependent electric field of a linearly-polarized pulse can be expressed mathematically:

$$E(t) = E_0(t)\cos(\omega t + \Phi), \tag{2}$$

where $E_0(t)$ is the envelope function, ω is the angular frequency of the light, and Φ is the carrier-envelope phase (CEP). For long pulse durations (τ) such that $\frac{1}{\omega} \ll \tau/2\pi$, the carrier wave oscillates through many cycles within the duration of the pulse. This results in a pulse with negligible differences in the amplitudes of the positive and negative field maxima. A change in the CEP in this regime does not have any influence

over the pulse shape, the peak intensity, or the yields of any laser induced processes.

However, linearly polarized laser pulses in which the electric field has a larger field amplitude for one polarity as compared to the other can be produced. These are known as "asymmetric" laser fields. There are two common types of asymmetric linearly polarized laser fields. The first is a few-cycle pulse in which the CEP is controlled so that the field amplitude during one half-cycle can be substantially larger than any other. The second combines an optical field at frequency ω, with its phase-locked second harmonic. By varying the relative phase between the two components of this "two-color" field, one can create a pulse with larger field maxima for positive or negative polarity. The two-color field approach can create a field asymmetry without the need for extremely short pulses or CEP control. The two-color approach was used for creating asymmetric laser fields for the experiments described in this dissertation and is discussed in more detail below.

1.3.1 Two-Color Asymmetric Laser Fields

As noted above, combining a fundamental laser pulse with its second harmonic can produce an asymmetric laser field if the relative phase between the two frequencies can be controlled. Fortunately, a phase-locked second harmonic pulse can be readily produced by second harmonic generation (SHG) in a nonlinear crystal such as beta barium borate (BBO). By combining the fundamental with its second harmonic, the electric field of a linearly polarized two-color pulse can be expressed as,

$$E(t) = E_{\omega}(t)\cos(\omega t) + E_{2\omega}(t)\cos(2\omega t + \phi) \tag{3}$$

where $E_{\omega}(t)$ and $E_{2\omega}(t)$ are the time-dependent envelopes of the two components and ϕ is the phase difference between the two colors.

Control over the two-color phase ϕ determines the direction and magnitude of the field maxima. The effect of the two color phase on the field profile can be seen in Figure 1.11. Note that for $\phi = \frac{\pi}{2}$, the negative and positive cycles have equal amplitudes. In the next section, we will discuss how two-color laser fields can be used to induce coherent rotational dynamics, including transient orientation within molecules.

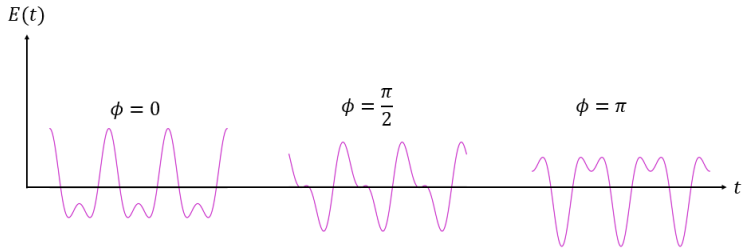

Figure 1.11: Three-cycles of the two-color electric field profile as a function of ϕ for $E_{2\omega}=\frac{E_\omega}{\sqrt{3}}$. For ease of comparison, the three field profiles each with a different ϕ have been temporally offset.

1.4 Controlling Molecular Rotational Degrees of Freedom

There are two common approaches for inducing molecular orientation. The first is a "brute force" method where static or optical fields alter the rotational level structure of the molecule resulting in preferential orientation while the field is on. Unfortunately, the orienting field can influence the primary measurements of interest if they alter the electronic or vibrational structure, induce additional dynamics, or complicate the detection of reaction products such as low energy electrons. The other method involves using a transient interaction, which can impart an angular "kick" or impulse to the molecules. The impulse causes the molecules to rotate and preferentially orient in the direction of the "kick" at particular times. After an initial preferential orientation period, the orientation is lost as the molecules continue rotating with a range of rotational velocities. Depending on the structure of the molecule, particularly for linear or symmetric tops, the initial orientation can fully or partially recur at integer multiples and rational fractions of a characteristic time known as the rotational revival time, T. Another transient interaction utilizes angle-dependent ionization to selectively ionize molecules in some orientations over others to induce transient orientation by filtering or depletion[33]. Both transient interactions were employed simultaneously in the experiments described in this dissertation and will be discussed in more detail in the next section.

1.4.1 Rotational Wavepackets

When an electromagnetic pulse has a temporal duration (τ) such that $2\pi/\tau \gg$ the relevant rotational constant(s) of the molecule, then it has sufficient spectral bandwidth to coherently excite a superposition of rotational states from a single initial rotational level, either via resonant excitation[7, 10] or through

stimulated Raman or hyper-Raman transitions[34]. The coherent superposition of rotational states, which is created in each molecule, is known as a rotational wavepacket. In a linear molecule like OCS, the wavepacket created from a single initial rotational state can be expressed mathematically,

$$\Psi(\theta, t) = \sum_{J,M} a_{J,M} e^{-iE_J t} |J, M\rangle \,, \tag{4}$$

where E_J is the rotational energy of state J and $a_{J,M}$ is the probability amplitude for state $|J, M\rangle$. Depending on its electronic ground state configuration, the linear molecule's rotational energy structure, E_J, and its corresponding rotational eigenfunctions can vary dramatically[35]. The electronic ground state configuration of OCS possesses no net electronic spin (S=0) and has no orbital angular momentum projection on the molecular axis(Λ=0). Molecules of this class are denoted as $^1\Sigma$ molecules, whereas molecules which have S=1/2 and Λ=1 are known as $^2\Pi$. Singly ionized OCS (OCS^+) will be relevant for the experiments performed in this dissertation, and since it has an electronic ground state with $^2\Pi$ symmetry[36], we compare the rotational structure of $^1\Sigma$ and $^2\Pi$ linear molecules below.

1.4.2 $^1\Sigma$ Molecules

In the rigid rotor approximation (i.e. ignoring vibrational excitation) molecules with an electronic ground state possessing $^1\Sigma$ symmetry (like OCS) have a rotational energy $E_J = BJ(J+1)$, where B is the rotational constant of the molecule, and J is the quantum number associated with the total angular momentum of the molecule, which, in this case, is equal to the rotational angular momentum. For $^1\Sigma$ molecules, such as OCS, the eigenfunctions $|J, M\rangle$ are spherical harmonics and J takes on integer values. Substituting for E_J, the wavepacket takes the form:

$$\Psi(\theta, t) = \sum_{J,M} a_{J,M} e^{-iBJ(J+1)t} |J, M\rangle \,. \tag{5}$$

In a thermal ensemble, the rotational state of each molecule prior to the aligning/orienting pulse can be described as an incoherent superposition of rotational states with occupation probabilities determined by the Boltzmann factor. During and/or immediately following an orienting pulse, the molecular ensemble exhibits preferential orientation. As time evolves, the preferential orientation of the ensemble is eventually lost for a distribution of initially thermally populated rotational states. Since the energy level difference

between rotational states is a multiple of $2B$ as shown in Figure 1.12, the phase difference between each rotational state within the wavepacket is a multiple of $2B$, and thus the wavepacket returns to its initial configuration immediately after the orientation pulse, at a characteristic revival time, T ($=\frac{\pi}{B}$ in a.u.).

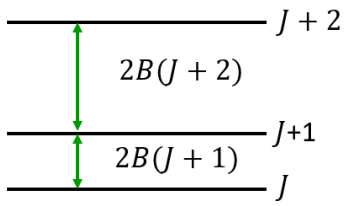

Figure 1.12: Rotational energy level diagram for a $^1\Sigma$ linear rigid rotor.

1.4.3 $^2\Pi$ Molecules

Molecular ground states may have non-zero electronic spin and orbital angular momentum. The electronic ground state (i.e the X-state) of OCS^+ has a $^2\Pi$ configuration with spin, S=1/2, and electronic angular momentum projected on the molecular axis, $|\Lambda| = 1$. Figure 1.13 depicts the electronic energy levels of the X-state of OCS^+[37] for total electronic angular momentum projected along the molecular axis, $|\Omega| = |\Lambda+S|$ = 3/2,1/2. The non-zero spin and electronic orbital angular momentum lead to a spin-orbit coupling that causes a splitting of the energy levels of the OCS^+ X-state. In general, the rotational energy levels for a linear $^2\Pi$ molecule are[38–40]:

$$E_{J'} = B_i[(J' - \frac{1}{2})(J' + \frac{3}{2}) \pm X_{J'}/2 \mp (Y - 2)], \tag{6}$$

where $X_{J'} = \sqrt{4(J' + 1/2)^2 + Y(Y - 4)}$ and $Y = A_0/B_i$. A_0 is the spin-orbit constant and, using the case of OCS^+ as an example, B_i is the rotational constant of the molecular ion. For a $^2\Pi$ molecule, the total angular momentum, J', takes on half-integer values in contrast to that of $^1\Sigma$ molecules. The two possible values of $E_{J'}$ correspond to the two different values of $|\Omega|$, which can be 3/2, (1/2) where the respective values of $|\Omega|$ correspond to the minus (plus) sign of $X_{J'}/2$ and plus (minus) in front of $(Y - 2)$ in equation 6. For the case of the X-state of OCS^+, $A_0 \simeq 1.69 \times 10^{-3}$ (a.u.)= 370 cm^{-1} [37] and $B_i \simeq 8.86 \times 10^{-7}$ (a.u.) = 0.1946 cm^{-1}[36] for $|\Omega|$=3/2 and $B_i \simeq 9.04 \times 10^{-7}$ (a.u.) = 0.1983 cm^{-1}[36] for $|\Omega|$=1/2. In this case, $Y \simeq 1900$,

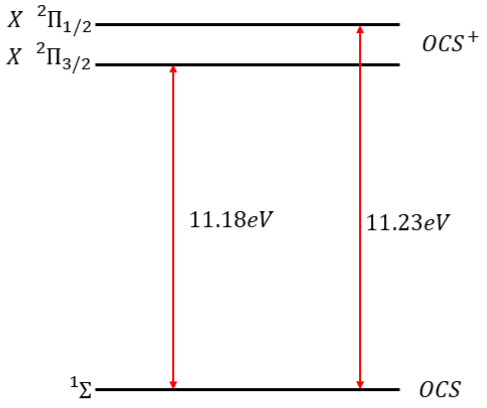

Figure 1.13: Diagram of the ground state energy level of OCS and the X-states of OCS^+[37]

and for $J' \ll Y$ (a very good approximation for the rotational states relevant to this work) equation 6 can be approximated as,

$$E_{J'} \approx B_i(1 \pm \frac{2}{Y})(J' - \frac{1}{2})(J' + \frac{3}{2}), \tag{7}$$

where the minus (plus) is for $|\Omega| = 3/2$ $(1/2)$. For half-integer J', the energy difference between states is an odd-multiple of B_i, so the wavepacket rephases at a revival time, T=$\frac{2\pi}{B_i}$, instead of $\frac{\pi}{B}$ for $^1\Sigma$ molecules. Both the $\Omega = 3/2, 1/2$ states are shown in Figure 1.13. For the case of the X-state of OCS^+, the spin-orbit coupling is much larger than the rotational energy level spacing (Hund's case (a)) for $J' \ll \sqrt{Y} \simeq 400$, and the relevant eigenstates can be approximated to be [38, 39],

$$|J', \overline{\Omega}, M'\rangle_s = \frac{1}{\sqrt{2}}[(-1)^{J'-M'}\,|J', \overline{\Omega}, M'\rangle + |J', -\overline{\Omega}, M'\rangle], \tag{8}$$

$$|J', \overline{\Omega}, M'\rangle_a = \frac{1}{\sqrt{2}}[(-1)^{J'-M'}\,|J', \overline{\Omega}, M'\rangle - |J', -\overline{\Omega}, M'\rangle], \tag{9}$$

where $\overline{\Omega}$ is the absolute value of Ω, and $|J', \overline{\Omega}, M'\rangle_{s,a}$ are constructed using superpositions of Wigner-D functions. Equations 8 and 9 describe two degenerate orthogonal states with even (symmetric states denoted with subscript s) and odd (antisymmetric states denoted with subscript a) symmetry, respectively. Note that only two angles, θ and ϕ, are necessary to describe the rotational state of a linear molecule. The quantum number, Ω, which specifies the molecular angular momentum along the molecular axis is purely electronic, and therefore is not associated with the rotational angular momentum of the ion. Therefore the coordinate, χ, which would ordinarily describe a rotation angle about the molecular axis in molecules that are not linear has a fixed value which we set to zero without loss of generality.

Despite having different rotational energy structure, rotational eigenfunctions, and rotational revival structures, the mechanism by which a laser field creates a rotational wavepacket that can exhibit transient alignment and/or orientation is the same for linear $^1\Sigma$ and $^2\Pi$ molecules. The following subsections will introduce how the parity of the wavepacket determines whether the wavepacket will exhibit preferential alignment and/or orientation using $^1\Sigma$ molecules as an example. The discussion is also relevant to $^2\Pi$ molecules.

1.4.4 Transient Alignment of $^1\Sigma$ molecules

An intense single color laser pulse can induce a series of stimulated Raman transitions within each molecule coupling rotational states of the same parity. For $^1\Sigma$ molecules, this leads to the following transition rule, $\Delta J = \pm 2, 0$. Figure 1.14 shows a cartoon of a laser pulse inducing a Raman transition in a $^1\Sigma$ molecule initially residing in rotational state J. These Raman transitions occur via the field's interaction with the molecule's polarizability. Since a photon is emitted and absorbed in this process, the parity of the initial rotational state must be conserved, so ΔJ must be even for a Raman transition. For example, a $^1\Sigma$ molecule initially residing in J=0 can either remain in J=0 or transition to J=2 following a Raman excitation. Since both J=0 and J=2 have even parity, any subsequent transitions from either will be to other even rotational states. Therefore, the overall parity of the wavepacket will remain even. An analogous argument for creating an odd parity wavepacket can be made for a $^1\Sigma$ molecule initially residing in an odd rotational state such as J=1. Since Raman transitions preserve the parity of the initial state, the newly created wavepacket's

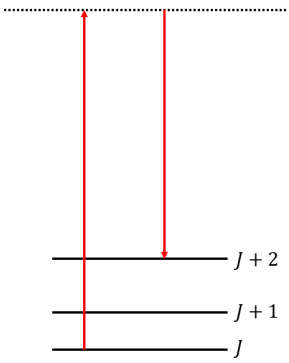

Figure 1.14: Cartoon of a Raman transition induced by a broadband laser pulse in a $^1\Sigma$ molecule initially residing in state J. A laser photon excites the molecule from J to a higher lying virtual state and within a femtosecond, a second photon de-excites the $^1\Sigma$ molecules from the virtual state to the J+2 state.

angular probability distribution ($|\Psi(\theta, T)|^2$) at the molecule's characteristic revival time will be symmetric along the laser polarization axes such that $|\Psi(\theta, t)|^2 = |\Psi(\pi - \theta, t)|^2$. For more information regarding the details of transient alignment, see the excellent discussion by previous PhD student, Dan Pinkham, in his dissertation[41].

1.4.5 Transient Orientation in $^1\Sigma$ molecules

A two-color laser field can induce field-free orientation by coherently exciting rotational states of opposite parity via hyper-Raman transitions[34]. A cartoon of a two-color laser pulse inducing a hyper-Raman transition in a molecule is illustrated in Figure 1.15. For $^1\Sigma$ molecules, these transitions are subject to the following selection rules: $\Delta J = \pm 3, 1$. Since the process absorbs and emits an odd number of photons, ΔJ must be odd for a hyper-Raman transition in a $^1\Sigma$ molecules, and therefore, the parity of the initial state changes after the interaction. This interaction creates a mixed parity rotational wavepacket within each molecule. To illustrate the connection between mixed parity rotational wavepackets and orientation, let us assume that a two-color laser pulse couples J=0 ($|0, 0\rangle$) and J=1 ($|1, 0\rangle$) states via a hyper-Raman transition.

Assuming equal amplitudes in two states, the wavepacket can be written as,

$$\Psi(\theta, t) = \frac{|0, 0\rangle + e^{-i2Bt}\,|1, 0\rangle}{\sqrt{2}}, \tag{10}$$

where $|0, 0\rangle$ and $|1, 0\rangle$ are spherical harmonics in the form $|J, M\rangle$. These states are of opposite parity, so when

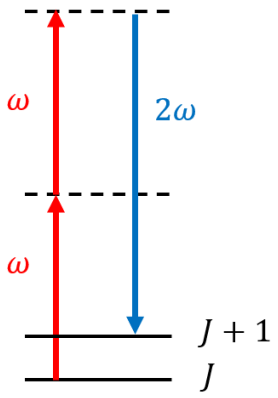

Figure 1.15: Cartoon of a hyper-Raman transition induced by a broadband laser pulse in a $^1\Sigma$ molecule initially residing in state J. A laser photon with frequency ω excites the molecule from J to a virtual intermediate state and a second photon at frequency ω excites the molecule to a higher lying virtual state. A second photon with a frequency near 2ω de-excites within a femtosecond from the virtual state to the J+1 state. The reverse order of excitation and emission can also occur, where one photon is absorbed and two photons are emitted.

combined coherently as shown in equation 10, the wavepacket $\Psi(\theta, t)$ has mixed-parity. The magnitude and direction of orientation is often quantified by computing the ensemble averaged expectation value of $\cos(\theta)$, $\langle \cos\theta \rangle$, where θ is the angle between the molecular axis and laser polarization direction. The time dependence of $\langle \cos\theta \rangle$ ($= \langle 0,0|\cos(\theta)|1,0\rangle \cos(2Bt)$) for the rotational wavepacket in equation 10 is plotted in upper right portion of Figure 1.16. The direction and magnitude of $\langle \cos\theta \rangle$ change with time and the initial orientation at t=0 is revived at the rotational revival time, T=$\frac{\pi}{B}$. For an oriented molecular ensemble, the angular probability distribution ($|\Psi(\theta, t)|^2$) demonstrates a preferential direction by having a higher probability at angle θ versus $\pi - \theta$ as shown at t=0 in Figure 1.16.

To illustrate the dependence of the magnitude of $\langle \cos\theta \rangle$ on rotational temperature, first consider a rotational wavepacket created from an initial $^1\Sigma$ rotational ensemble at $T_{rot} = 0K$, where all the molecules reside in J=0. Upon applying a transient two-color laser pulse, all the molecules initially in J=0 will preferentially orient along the laser polarization axis at the same time. For the case of a distribution of thermally populated rotational states, the contribution to the overall orientation from each initial state must be taken into account. Effectively, this lowers the overall orientation compared to the scenario for all the molecules initially residing in the J=0 state. Molecules initially residing in higher lying rotational states rotate faster, so upon excitation

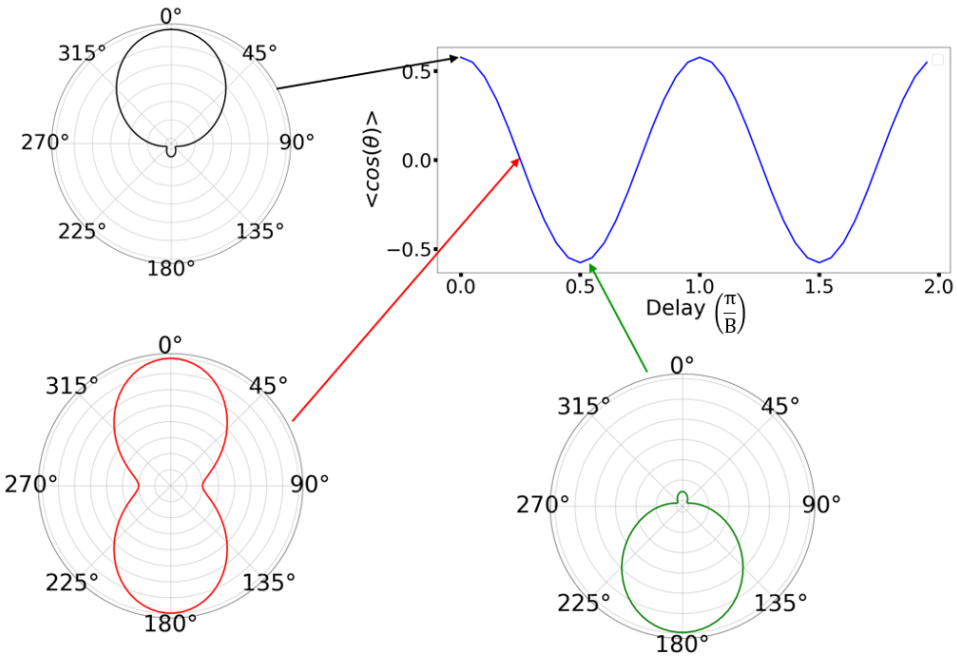

Figure 1.16: Calculated $\langle \cos\theta \rangle$ for the wavepacket in equation 10 as a function of delay. The computed angular probability distributions ($|\Psi(\theta,t)|^2$) are also shown at various delays.

by a two-color field, higher lying rotational states can reach the polarization axis sooner than the lower lying states, thus limiting the overall degree of orientation. Reducing the molecule's rotational energy (rotational temperature) is necessary but not sufficient for achieving higher degrees of orientation. Our experimental technique for lowering the rotational temperature of the molecular ensemble will be discussed in the Chapter 2, the experimental/apparatus section.

Angle-dependent ionization is another interaction which can create transient orientation[33]. The interaction selectively ionizes molecules of a given orientation with respect to the direction of the field at the instant of ionization, as depicted in Figure 1.17. This form of ionization creates a coherent "hole" in the angular probability distribution ($|\Psi(\theta,t)|^2$), where the field-free evolution of the "hole" is analogous to our description of the field-free evolution of the angular probability distribution formed via hyper-Raman transitions.

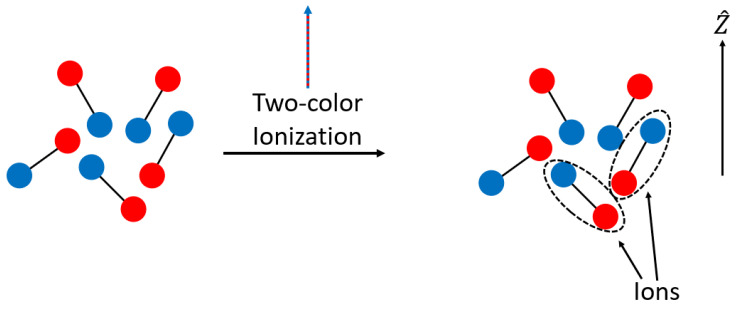

Figure 1.17: A cartoon portraying an isotropic rotational distribution of molecules that changes after an intense two-color ionizing laser field. The rotational distribution of the remaining neutrals and newly created ions exhibit a preferential orientation such that the ensemble average direction from the center of the molecule to the red atom is $+Z$ and $-Z$ for the remaining neutrals and ions, respectively.

1.4.6 Theoretical Rigid Rotor Dynamics of $^1\Sigma$ molecules

Upon exposure to an intense two-color laser pulse, a rotational wavepacket is launched within each molecule. For simplicity, we consider only an ensemble of $^1\Sigma$ molecules such as OCS. For a molecular ensemble with rotational temperature, T_{rot}, the initial distribution of the thermally populated states is dictated by the Boltzmann distribution. A plot of the distribution of thermally populated rotational states is shown in Figure 1.18 at two different rotational temperatures.

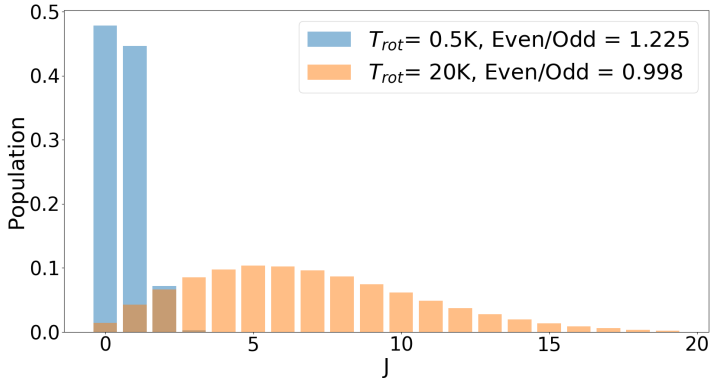

Figure 1.18: Calculation of the distribution of rotational states governed by the Boltzmann distribution at rotational temperatures of 0.5K and 20K in OCS. The legend shows the ratio of the even to the odd population at the two different rotational temperatures

For $T_{rot} = 20K$, there are approximately an equal number of even and odd populated rotational states;

therefore, after an orienting pulse, the rigid rotor dynamics of OCS can exhibit preferential orientation only at its full rotational revival time (T_{OCS}). This is because the contributions of the initially even and odd rotational states in the thermal distribution to the orientation perfectly cancel at the half rotational revival time ($T_{OCS}/2$) but add constructively at T_{OCS}[7]. One can qualitatively understand the rigid rotor dynamics by examining the angular probability distribution at various delays after the orienting field is off. A cartoon of this is shown in Figure 1.19. For a molecule residing in some state J, a two-color pulse couples J and J±1

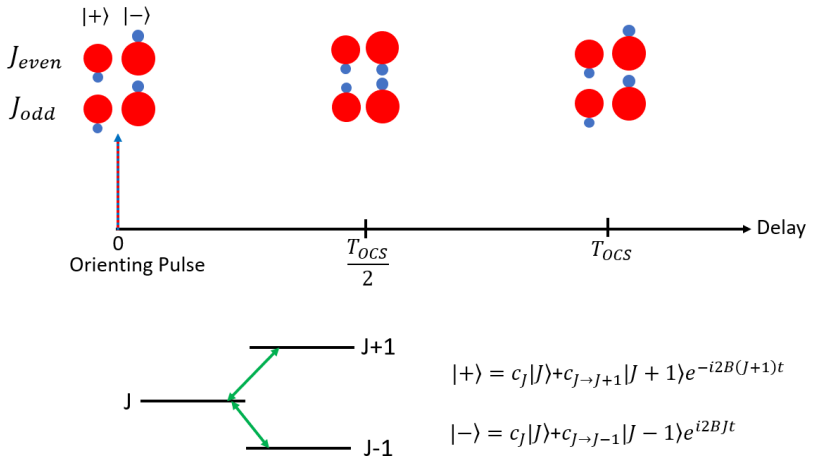

Figure 1.19: Cartoon of the rigid rotor dynamics in a $^1\Sigma$ molecule following a two-color orienting pulse. Above each delay, the angular probability distribution (shown in red/blue) is shown for each parity and superimposed state. The complex phase factors are the energy differences between the superimposed states.

via hyper-Raman transitions. For illustrative purposes, we can separately write the superpositions of J,J+1 and J,J-1 states as $|+\rangle$ and $|-\rangle$, respectively. A cartoon of the angular probability distribution for both $|+\rangle$ and $|-\rangle$ is shown for both even and odd rotational states. Immediately following the two-color interaction, the plus and minus angular probability distributions preferentially orient in opposite directions for both even and odd rotational states. However, there is not a perfect cancellation between the plus and minus states as the transition matrix elements ($c_{J\to J+1}$) and ($c_{J\to J-1}$) are not equal. So the combined even and odd angular probability distributions produce a small degree of orientation. This same probability distribution revives at T_{OCS}. Interestingly, at $T_{OCS}/2$, the $|+\rangle$ and $|-\rangle$ superpositions orient in the same direction. However, the initial even and odd rotational state contributions are opposite; therefore, the net orientation at half-integer revivals is nearly zero if the even and odd states have approximately the same weight in the initial thermal

distribution. With the application of a properly timed rotational pre-excitation pulse, field-free orientation at the half-integer revivals can be achieved and has been observed experimentally in other research groups[7, 8, 42] as well as in our lab. More information about the theory, techniques, and measurements of field-free orientation at half-integer revival times can be found in Appendix B.

1.5 Multiple Ionization and Coulomb Explosion

When a strong laser field simultaneously removes one or more electrons from a molecule, the molecular bonds weaken and stretch. If the distance between two molecular fragments reaches a critical value while the laser field is still present, additional electrons may be more easily removed. This process is known as enhanced ionization [43], and following the localization of electron holes in two or more molecular fragments, can ultimately lead to the strong repulsion of those fragments, resulting in what is known as a Coulomb explosion. When the laser field is polarized along the internuclear axis, it acts over the entire length of the molecule making it easier to distort the electric potential and increasing the ionization rate [2]. Therefore, Coulomb explosion is most effective when the laser pulse is polarized along the molecular axis. Detection of ion fragments from highly directional Coulomb explosion can be a very effective method for characterizing the molecular angular distribution at the instant of ionization [2, 7, 8]. The next section will discuss details of the laser system and apparatus used for creating and detecting aligned and oriented OCS molecules.

2 Experimental Apparatus Overview

This chapter focuses on the apparatus and techniques used to perform the experiments described in this dissertation. In particular, I will focus on the following:

- Laser Systems
- Vacuum Systems
- Data Acquisition and analysis

2.1 Femtosecond Laser Systems

Our femtosecond laser systems use Ti:sapphire as the gain medium. Its broad spectral emission makes it ideal for generating ultrashort laser pulses with pulse durations as short as 5 fs being possible. The experimental work described in this dissertation uses a femtosecond laser system which contains the following elements for producing ultrashort laser pulses at a 1kHz repetition rate:

- Broad-Bandwidth mode-locked oscillator
- Temporal Pulse stretcher
- Pulse Pickers
- Three-stage Amplifier
- Temporal Pulse compressor

This combination of elements for generating ultrashort pulses is known as chirped pulse amplification (CPA) [44]. The femtosecond laser system uses chirped-pulse amplification of 20 fs laser pulses from a mode-locked oscillator and outputs ultrashort laser pulses with durations $\approx$ 30 fs and pulse energy $\approx$ 2.5 mJ at a 1kHz repetition rate.

2.1.1 Ti:Sapphire Oscillator

A KM Labs Model MTS Ti:Sapphire oscillator [45] generates ultrashort seed pulses. The oscillator is pumped by 4.25W of 532nm light from a frequency doubled $Nd:YVO_4$ CW laser (Spectra-Physics Millennia Vs).

This oscillator employs Kerr lens mode-locking to generate a pulse train at 90MHz repetition rate. Typical mode-locked output has an average power of ≈ 400 mW with ≈ 5nJ per pulse. Typical spectra of the seed light (Fig.2.1) is centered about 790nm with a 50nm bandwidth.

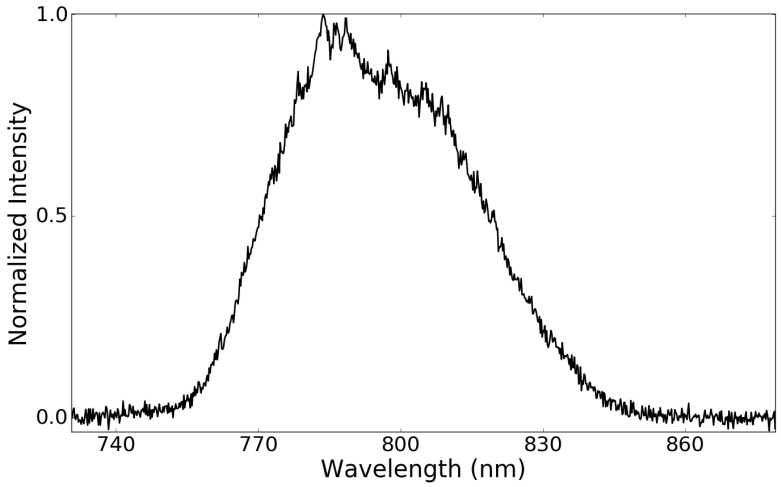

Figure 2.1: Oscillator spectra of the seed pulse measured before entering the temporal pulse stretcher

2.1.2 Ultrafast Temporal Pulse Stretcher

The grating stretcher spatially disperses the various frequencies of the ultrafast laser pulse. The stretcher is designed so that this spatial dispersion leads to different path lengths traveled by various wavelength components in the pulse as illustrated in Figure 2.2. The stretcher adds a temporal chirp to the pulse, increasing its pulse duration from ≈30 fs to ≈100 ps. Stretching the pulse allows greater pulse amplification while maintaining an intensity below the damage threshold of Ti:Sapphire and below that where the spatial and temporal characteristics of the pulse would be modified by non-linear effects upon propagation through the various amplifier components. This allows the seed pulses to be amplified without damaging the amplifier or altering the pulse in undesirable ways.

2.1.3 Dazzler

The Dazzler developed by Fastlite is an ultrafast pulse shaping system that makes both spectral phase and amplitude adjustments to ultrafast laser pulses. The Dazzler is based on an acousto optic interaction and

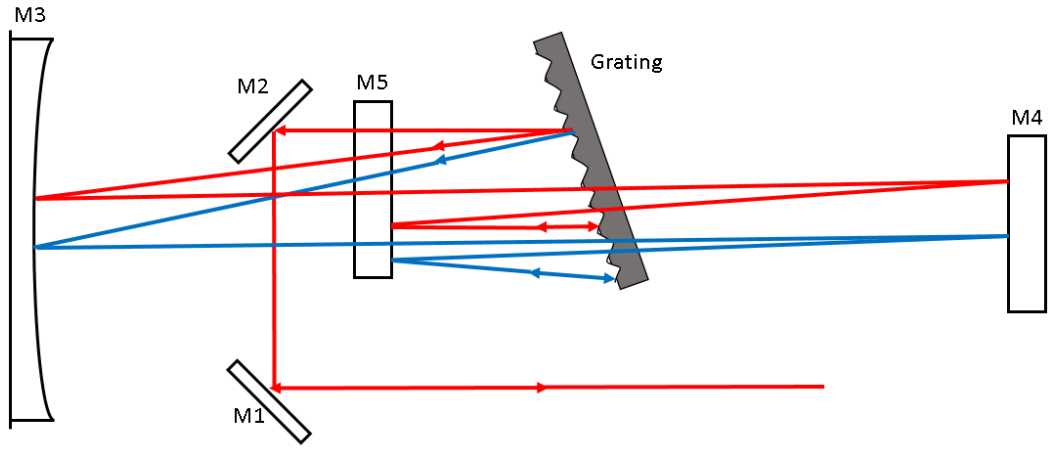

Figure 2.2: Pulse stretcher diagram (top view). The output stretched beam is vertically displaced slightly down and then sent to the Dazzler. Note that lines appearing to pass through mirrors represent beams passing over the optical element.

shapes ultrafast pulses within the bulk of a single acousto optic crystal. The primary purpose of the Dazzler is to shape our seed pulses to reduce the effects of gain narrowing and correct for nonlinear dispersion acquired upon transmission and reflection from various optical elements. This ensures that the pulses after amplification can be compressed to near their transform limit. Two beams exit the Dazzler with the shaped beam diffracted at the larger angle. The main screen of the Dazzler software control program is shown in Figure 2.3. A common use for the Dazzler is to modify the spectrum of the pulse to compensate for gain narrowing that occurs during three stages of amplification. For effective compensation, it is important to use a spectrometer to monitor the spectrum after each stage of amplification while varying the Dazzler settings. The settings shown in the image were in use at the time of writing this chapter. The orange section allows the user to insert a spectral dip of variable width and depth centered at the specified wavelength. The green section label "Derivatives" controls the various orders of dispersion compensation added to the pulse. As the pulse acquires nonlinear dispersion after traversing numerous optical elements, the user can correct for dispersion (out to the fourth order) by manually adjusting the values of the derivatives. Higher order dispersion compensation beyond fourth order is possible, but requires the user to manually input the values using a text file. The lower middle plot in Figure 2.3 shows the model spectrum imprinted onto the pulse after adjusting the various settings.

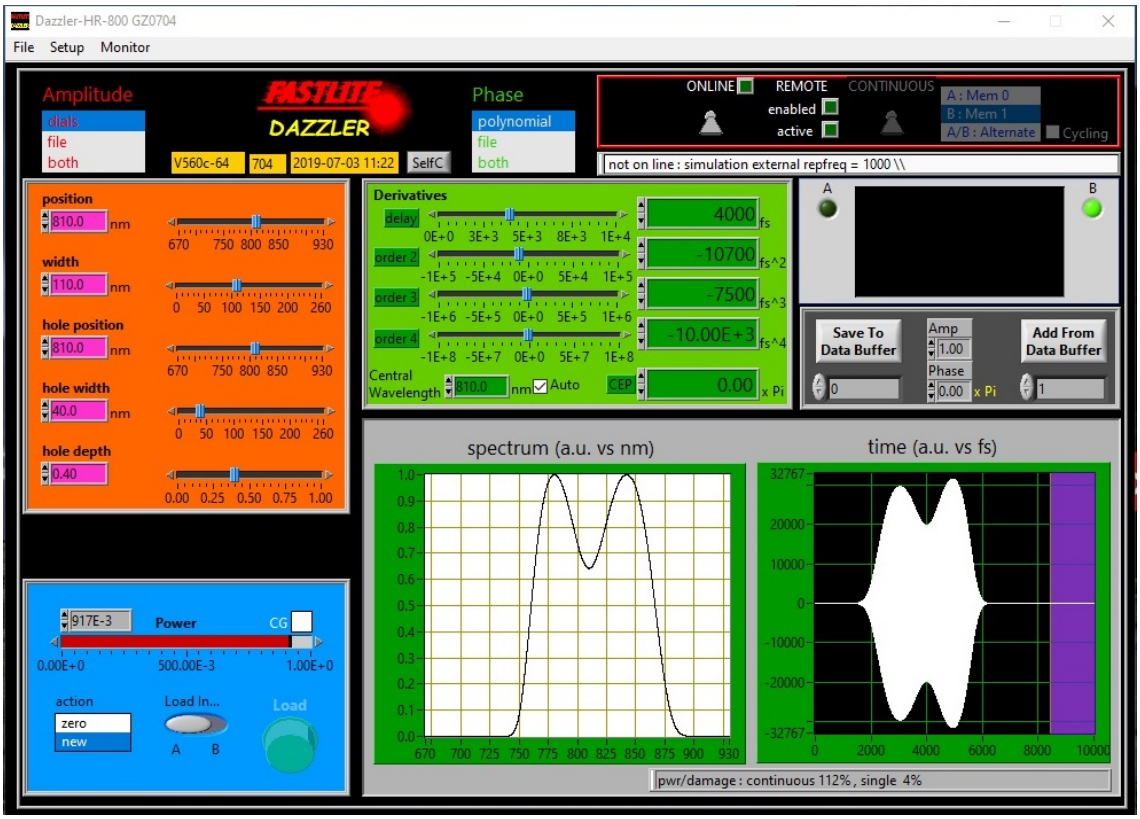

Figure 2.3: Dazzler control software program

The Dazzler can be run in continuous or shot-to-shot mode. When running experiments, it is important to synchronize the dazzler with the amplifier output, so running the Dazzler on shot-to-shot mode is required. The continuous mode is convenient for aligning the seed into the amplifier, so that the beam can be viewed by eye or with an IR card. When adjusting between modes, the RF power also needs to be adjusted as the Dazzler software is interlocked to prevent damage to the amplifier.

2.1.4 Timing Electronics

Fine temporal synchronization among the oscillator pulse train, pump lasers, and the various active optical elements is required for proper operation of the ultrafast laser system. Due to amplifier pump power limitations, the amplifier runs at a substantially reduced repetition rate as compared to the pulse frequency of the oscillator. A train of pulses at 1 kHz is selected for amplification from the 90 MHz oscillator output. To produce the 1 kHz seed pulse train, a photodiode first detects seed light scattered from the Ti:Sapphire crystal inside the KLM oscillator. The photocurrent is converted to a voltage that serves to synchronize a

variety of electronics as outlined in Figure 2.4. After being amplified and shaped into a sine wave, the 90 MHz mode-lock reference is sent to a synchronizing module. A standard clock (10 MHz) from a Stanford Research System Digital Delay Generator (DG645) and frequency divider generate trigger pulses (at 1 kHz) that are sent to the Spectra Physics synchronization module. After receiving each trigger pulse, the sync module produces a delayed trigger that is synchronized with a given phase of the 90 MHz mode-locker reference. The delayed trigger has a temporal jitter of <1 ns relative to the optical pulses from the Ti:Sapphire oscillator. This optically synchronized 1kHz pulse train is then used to synchronize trigger sensitive devices as outlined in Figure 2.4.

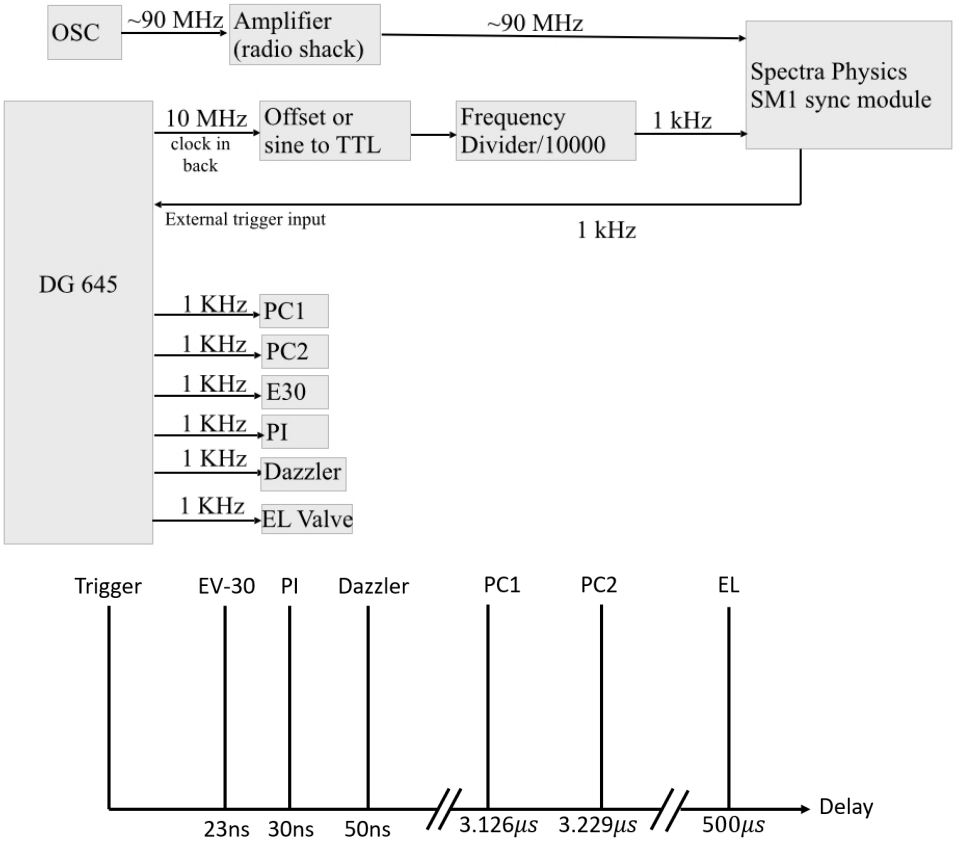

Figure 2.4: Timing diagram for synchronizing trigger sensitive equipment. Trigger: 1KHz pulse train output from the DG 645. EV-30: Evolution-30 Nd:YLF laser, PI: Photonics Industries Nd:YLF laser, PC1: Pockels cell as pulse picker into multipass amplifier, PC2: Pockels cell as a pulse cleaner, removing pre- and post- pulses as well as amplified spontaneous emission from the first amplifier stage, EL: Even-Lavie Pulsed Valve

2.1.5 Multi-Pass Amplifier

The output of the Dazzler is sent into a pulse picker that selects pulses to enter the amplifier. The pulse picker is composed of a polarizer (GLP) and Pockels cell (PC1), operated at near quarter wave voltage (2.35 kV). The pulse picker synchronized by the 1kHz trigger switches a single seed pulse every ms into a home built Ti:Sapphire multi-pass amplifier[46]. Details on the pulse picker's design and specifications can be found in Appendix A.

This amplifier is pumped by an Evolution-30 Nd:YLF laser. For the Nd:YLF laser, an array of diodes pumps a Nd:YLF laser rod. The cavity is acousto-optically Q-switched emitting light at 1053 nm, 200 ns pulses. A non-critically phase-matched LBO crystal is placed inside the cavity for second harmonic generation. The second harmonic light (λ = 527 nm) passes through a dichroic mirror, exiting the cavity with a typical average output power between 15-20W. The Ti:Sapphire crystal in the multi-pass amplifier is pumped with 8.5W of average power and situated at the center of a triangular cavity, whereby a single seed pulse makes 10 passes before being steered out of the amplifier (see Figure 2.5). Since the multipass amplifier is not configured as a laser cavity, aperture masks are inserted for each pass through the amplifying crystal, in order to limits the effects of thermal lensing on the spatial profile of the beam. Shot to shot stability can be checked using a photodiode. Depending on the Dazzler settings, the typical output from the multipass is $\approx$ 0.7-1 mJ per pulse.

2.1.6 2nd-Stage Amplfier

The second stage amplifier is pumped by the same Nd:YLF laser used for pumping the multi-pass amplifier. Prior to entering the 2nd stage amplifier, a second Pockels Cell and Glan-Laser polarizer are used to eliminate pre- and post-pulses and amplified spontaneous emission (ASE) from the output of the multipass amplifier. The time window for selecting the main pulse is 5ns. The second stage amplifier is a two-pass bowtie amplifier that can extract up to 1.4-1.5 mJ per pulse. At higher pump energies, the temperature of the water cooled Ti:Sapphire crystal becomes elevated, thus causing distortion in the spatial mode due to thermal lensing.

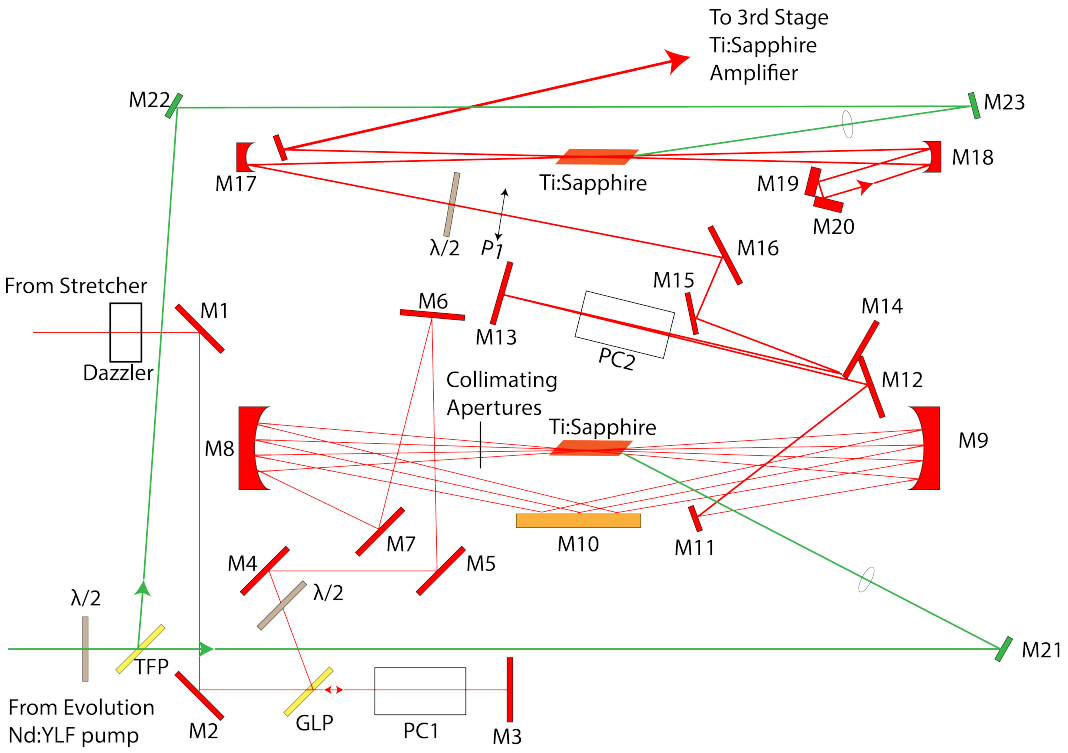

Figure 2.5: Multi-Pass Amplifier with a bow-tie two-pass amplifier. The seed light takes 10 passes before being steered out by M11. Both amplifiers are pumped from the same Evolution Nd:YLF system. The multipass is pumped with 8.5W of average power at 1kHz repetition rate. Note that the angle between M21 and M9 has been increased for display only in the figure.

2.1.7 3rd Stage Amplifier

After the multipass and second-stage amplifier, this 3rd stage of amplification is required to attain higher pulse energies. To avoid severe thermal lensing and damage, the Ti:sapphire crystal is placed under high vacuum and cooled with liquid nitrogen (LN_2). A LN_2 reservoir is placed in thermal contact with a copper housing holding the Ti:sapphire crystal in place within an ion-pumped vacuum chamber with a background pressure of 1×10^{-9} Torr.

Since the crystal is cooled with LN_2, the crystal (unfortunately) also acts like a cold trap, drawing any particulates to the surface. In addition, the reservoir contracts upon adding LN_2, so it is important to allow 20-30 minutes after filling the can to ensure the contraction stabilizes before seeding the amplifier. The amplifier is pumped with a Photonics Industries Nd:YLF laser that outputs 20W of average power at 1 kHz repetition rate. A thermal sensor placed in the copper housing monitors the crystal temperature and an interlock protects the crystal when its temperature rises above the setpoint. The experimental setup is

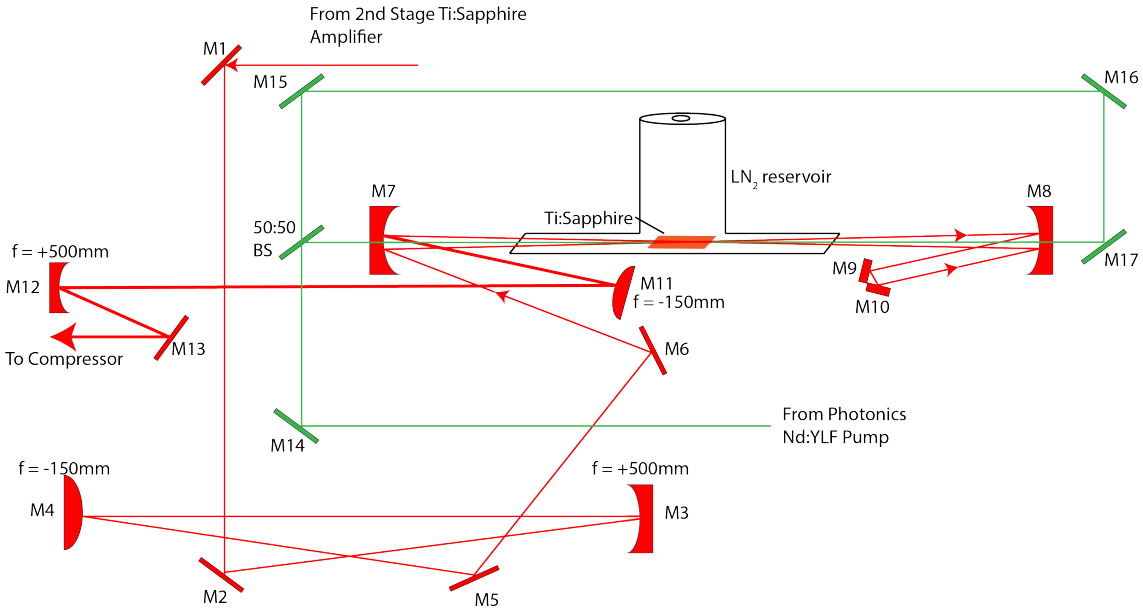

Figure 2.6: Schematic of the third stage amplifier.

shown in Figure 2.6, and a picture of the vacuum chamber is shown in Figure 2.7. Quartz brewster windows

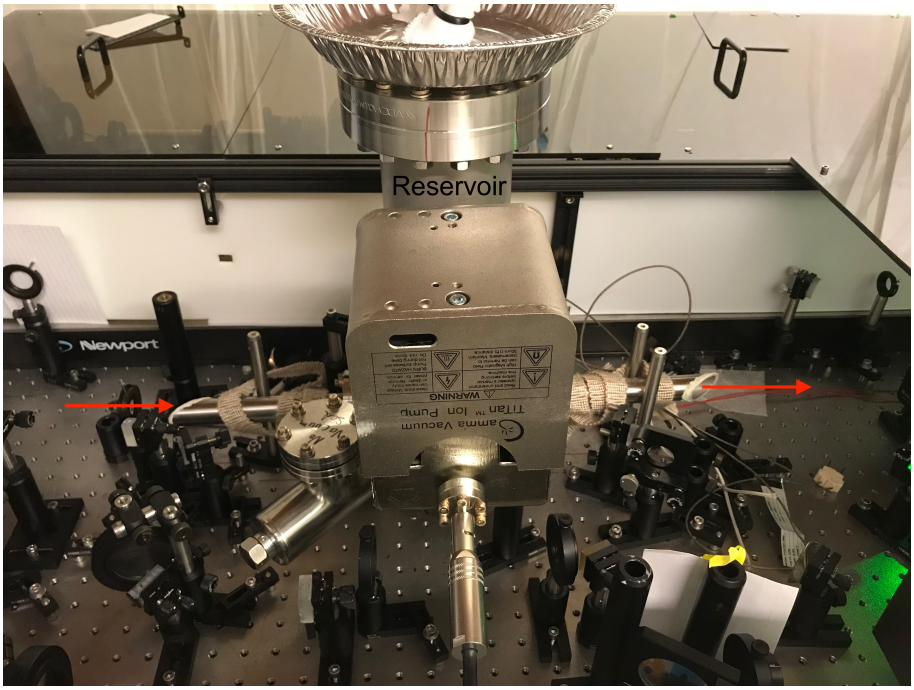

Figure 2.7: 3rd Stage amplifier's vacuum chamber holding a Ti:Sapphire crystal. LN_2 reservoir (labeled) situated above the Ti:Sapphire crystal (not shown). Red arrows indicate the direction of the seed pulse.

allow the amplified seed and pump pulses to pass through the Ti:Sapphire crystal. Typical output after the

3rd stage amplifier and before the compressor is between $3-4$ mJ per pulse assuming that the average power output of the Photonics Nd:YLF pump laser is $\approx$ 20W.

2.1.8 Compressor

The pulse compressor illustrated in Figure 2.8 acts similarly to that of the stretcher, except the arrangement removes the positive temporal chirp applied by the stretcher. The compressor gratings can also be angle tuned to compensate for third order dispersion. However, with the Dazzler in place, the dispersion can now be compensated, programmatically. The peak compression efficiency is around 70%. Typical compressed output power from all 3 amplifier stages is 2.3-2.8W, depending on the pulse energy requirements for a given experiment. The LN_2 cooled 3rd stage amplifier is fully pumped to extract the most amplification; whereas the 2nd stage amplifier is pumped partially to extract the remaining gain to attain the desired compressed output power. This sequence ensures that the effects of thermal lensing are minimized.

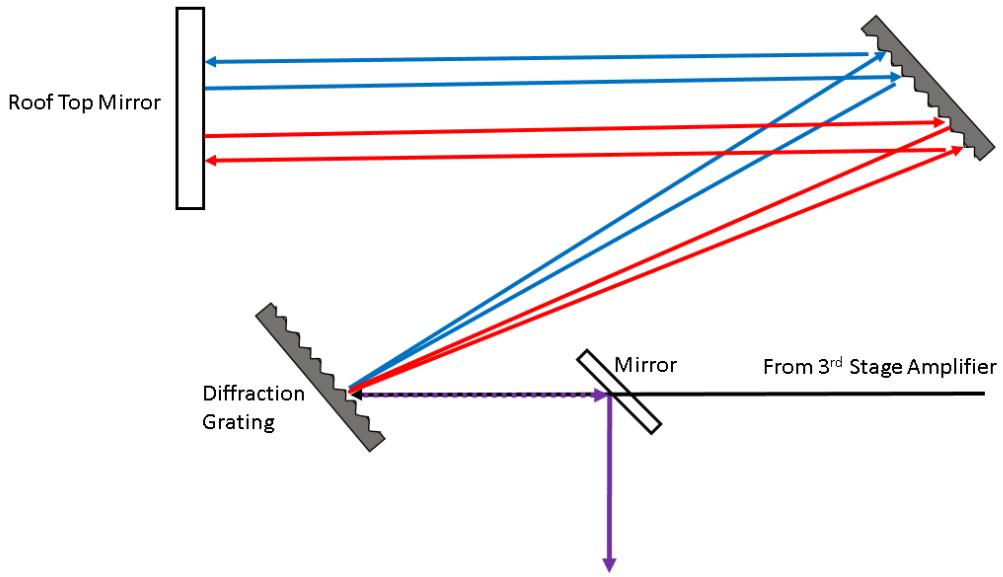

Figure 2.8: Experimental setup of the grating compressor. The chirped beam (black) passes above the mirror prior to being diffracted by the grating. The path length between the red and bluer frequency components can be adjusted by changing the separation between the gratings. The compressed beam (purple) is reflected out to the main experimental setup.

2.2 Laser Pulse Diagnostics

After compressing the stretched pulse back into an ultrashort laser pulse, measuring the laser pulse duration is the next step toward fully characterizing the laser pulse. Since electronic-based detectors are unable to measure changes on the femtosecond time scale, the best method to probe the pulse duration is to use the pulse itself. The following methods are employed for full temporal characterization of the compressed laser pulse.

2.2.1 Intensity Autocorrelation

Interfering two identical copies of laser pulses in a nonlinear-optical crystal and measuring the cooperative signal pulse energy while scanning the delay yields the scanning intensity autocorrelation (A), defined in equation 11.

$$A(\tau) = \int_{-\infty}^{\infty} I(t)I(t-T)dt, \tag{11}$$

where I(t) is the intensity of one pulse, I(t-T) is the intensity of second pulse with a relative time delay, T. The autocorrelator systems in our lab use second harmonic generation (SHG) from a BBO (Type I) nonlinear crystal. The autocorrelation temporal width (τ_a) is related to the pulse duration (τ) through this following relation (assuming a gaussian shaped pulse) :

$$\tau = \frac{\tau_a}{\sqrt{2}} \tag{12}$$

The single-shot autocorreletor is a quicker but less quantitative method for determining the pulse duration. It utilizes a cross beam geometry as shown in Figure 2.9. SHG is visible for the two incident fundamental beams; however, when the two fundamental beams are spatially and temporally overlapped, a third beam forms between the two incident beams.

The third beam is then imaged by a CCD camera, whereby temporal information of the red pulse is reflected in the spatial intensity distribution of the SHG beam. The diameter of the SHG beam (Δx) is related to the temporal width of the autocorrelation (τ_a) by,

$$\Delta x = \frac{\tau_a v_g}{sin\varphi} \tag{13}$$

where v_g is the group velocity of the fundamental in the BBO.

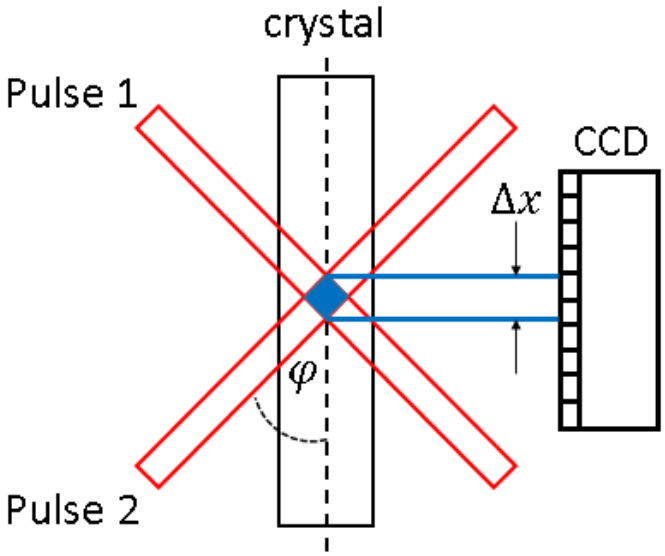

Figure 2.9: Single Shot Autocorrelator

2.2.2 FROG

Frequency Resolved Optical Gating (FROG)[47] is a diagnostic tool that provides pulse duration and spectral phase information. Spectral phase information provides insight into whether the pulse is at its transform limit or has additional nonlinear dispersion. We have both single-shot and scanning SHG FROG setups. Experimentally, replacing the CCD camera with a spectrometer is required for creating a setup for acquiring FROG traces. The FROG, Dazzler, and compressor are all used in unison to quantify the pulse duration and spectral phase to achieve the shortest pulse duration. A typical scanning SHG FROG trace is shown in Figure 2.10.

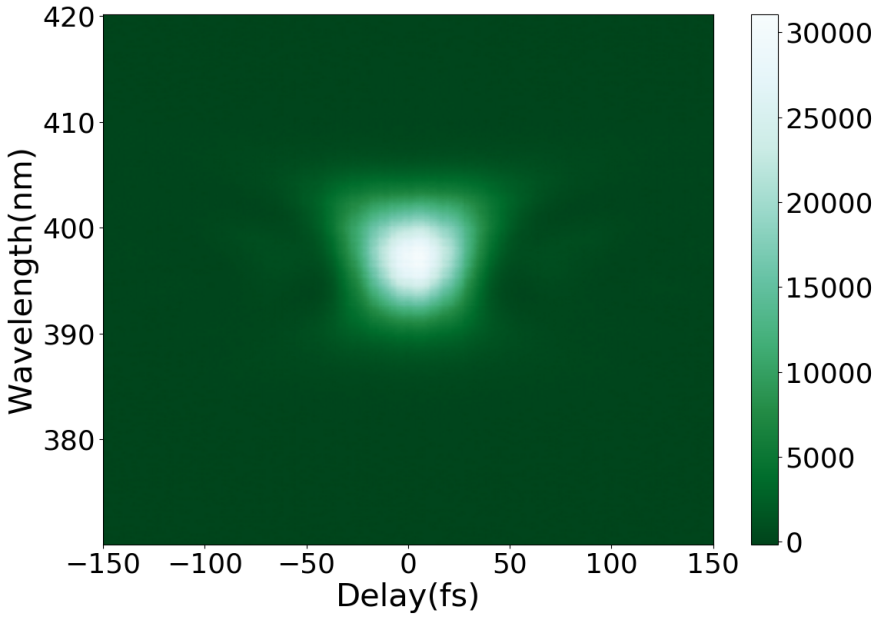

Figure 2.10: Measured SHG FROG Trace.

2.3 Vacuum Hardware

All experiments are performed under a high vacuum environment. This section will describe the principle vacuum components and chamber configurations utilized in this dissertation.

2.3.1 Roughing Pumps

Rotary vane roughing pumps are used throughout the lab. These roughing pumps can bring a chamber or gas line down to a few mTorr in pressure, so their primary use is for clearing gas inlet lines and to back turbomolecular pumps.

2.3.2 Turbomolecular pumps

High vacuum environments are needed to perform molecular rotational dynamics experiments. This ensures that the mean-free path of the gas molecules is sufficiently large compared to its size over the observation time window. This prevents collisions and other molecular interactions from perturbing the laser-molecule interactions. Various Varian Turbopumps are used to achieve base pressures as low as 5×10^{-9} Torr. A

high frequency motor drives a turbine with a series of tilted fan blades forcing air through the blades and into the intake of the rotary vane roughing pump. The pumps are driven by a turbo pump controller. The controller is equipped with a soft start feature that slowly ramps the turbine rotation rate and monitors the power drawn and temperature of the pumps.

2.3.3 Ion Pumps

A Gamma Vacuum ion pump (with a speed of 25L/s)[48] is used in the vacuum chamber housing the LN_2 cooled Ti:Sapphire crystal. After initial roughing and turbo pumping, the chamber is sealed off and pressures below 1×10^{-9} Torr are achieved with the ion pump working alone. Ion pumps have magnets located outside the vacuum, which contains and guides electrons within circular anode rings. Upon engaging the ion pump, high voltage is applied to an anode assembly enabling free electrons to rotate freely. As gas moves freely into the anode assembly, electrons can strike the gas molecules creating positively charged ions. These ions are then accelerated toward grounded cathode plates creating a vacuum and an electric current that is proportional to the pressure inside the chamber.

2.3.4 Thermocouple Gauges

Thermocouple vacuum gauges are used in the lab for measuring rough vacuum pressures in gas inlets and the pressure backing the turbo pumps[49]. Thermocouple gauges measure pressure based on the amount of heat an ambient gas will carry from a hot wire. A thermocouple is placed on the wire and converts its temperature to a voltage reading, which is calibrated to specific pressures. Lower pressure will results in less heat being dissipated by the gas, so a higher temperature and voltage output from the thermocouple.

2.3.5 Nude Ion Gauge

After engaging the turbomolecular pumps, pressures can drop well below the operating range of thermocouple gauges. Nude ion gauges are used for measuring these lower pressures. The ionization gauges are based on the Bayard-Alpert design [50], whereby a hot filament produces electrons and accelerates them towards a positively charged cylindrical grid. During that travel, the electrons can collide with gas molecules and ionize them. The resulting molecular cations are attracted to a wire along the center of the grid. The ensuing

current flow is directly proportional to the number of molecules present. This design is capable of measuring pressures below 1×10^{-9} Torr.

2.3.6 Vacuum Interlocks

The turbopumps and gauges are connected by interlock circuitry to shut down these components in the case of a power outage, vacuum leak, or component failure. This is done via a series of voltage relays which control AC power to the turbo pumps, pneumatic valves, and gauge controllers. For short term power outages, UPS systems were added to sustain power for the turbo pumps.

2.4 Experimental Vacuum Chamber

2.4.1 Supersonic Molecular Beam Expansion Chamber

The molecular beam expansion section of the vacuum chamber enables the creation of a rotationally cold molecular beam for experiments studying strong field ionization of aligned and oriented molecules. Rotational cooling is accomplished by creating a supersonic molecular beam by expanding a high pressure gas through a small nozzle diameter[51]. When the mean free path length is significantly smaller than the nozzle diameter, numerous collisions between molecules occur during their transit from source into vacuum. The collisions are responsible for the cooling process, so it is common to the seed the target gas species with a lighter buffer gas such as helium to increase the collision frequency. The experiments described in this dissertation employ a pulsed Even-Lavie (EL) valve [52]. The EL valve can accommodate gas backing pressures as high as 100bar, while the small nozzle diameter and short valve opening times reduce the gas load in the chamber and enable operation at a 1kHz repetition rate. With the EL valve engaged, the valve opening time set to $\approx 13\mu$s such that the background gas pressure in the expansion chamber reaches 5×10^{-6} Torr. As the target gas enters vacuum, it expands adiabatically, where its final temperature is related to the initial pressure, p_0, and temperature, T_0, by,

$$\frac{T_f}{T_0} = \left(\frac{p_f}{p_0}\right)^{\frac{\gamma-1}{\gamma}} \tag{14}$$

where γ is the heat capacity ratio $\left(\frac{C_p}{C_v}\right) = 1.29$ for OCS [53]. Equation 14, qualitatively, illustrates how a large pressure gradient between the source and vacuum region can significantly reduce the translational

and rotational temperature of the molecules. Since the molecular beam travels at supersonic speeds, cooling with respect to translation motion refers to a highly direction molecular beam with the molecules being rotationally "frozen". In practice, there are several factors that can limit the degree of rotational cooling. Since the rotational energy levels are discrete, the energy lost from the molecule due to a collision must match the separation between the intial and final rotational energy levels. As the molecular beam travels, its density is reduced, limiting the collisional energy transfer. When the molecular beam density approaches the background density, randomly directed collisions with background molecules (i.e. N_2, H_2O, O_2) can occur, further limiting the rotational cooling. As illustrated in Figure 2.11, a cone-shaped skimmer connects the expansion and detection sections of the experimental chamber, allowing for differential pumping and selecting only the central, coldest portion of the molecular beam for the experiments (see Figure 2.11). Since the molecular beam expands beyond the skimmer diameter in the interaction region, the molecular beam is diverging, which indicates that there are likely collisions between the molecular beam and background molecules. Gas temperatures on the order of 20K are readily achieved for few atom molecules like those that are the focus of this dissertation.

2.4.2 Detection Chamber

The detection chamber has an ambient pressure of 5×10^{-9} Torr and contains a Time-of-Flight (TOF) spectrometer with a microchannel plate (MCP) based charged particle detector.

2.4.3 Time of Flight Mass Spectrometer

An externally applied electric field in the laser-molecule interaction region of the spectrometer pushes positively charged ions created in the laser focus towards the ion detector. The acceleration of a charged particle due to the applied electric field is proportional to the particle's charge-to-mass ratio. Along the spectrometer axis, which we can denote z,

$$F_z = ma_z = qE_z \tag{15}$$

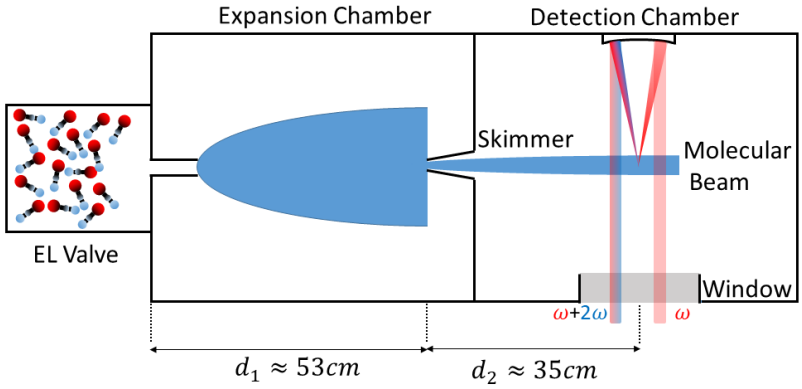

Figure 2.11: Top view of supersonic expansion and detection chamber. Turbo pumps that enable differential pumping of the two sections of the chamber are not shown. A fused silica window allows the laser beams to enter the detection chamber, where they are focused by a spherical enhanced aluminum mirror onto the molecular beam. EL: Even-Lavie pulsed valve. d_1 is the approximate distance from the EL valve to the skimmer. d_2 is the approximate distance from the skimmer to the interaction region. The skimmed molecular beam diameter in the interaction region is approximately 6mm.

where F_z is the force felt by the particle, m and q are the particle's mass and charge, respectively, and E_z is the externally applied field. Rearranging the expression and solving for a_z.

$$a_z = \frac{qE_z}{m} \tag{16}$$

Assuming that the particle initially has no initial velocity in the direction of the applied field, its subsequent motion can be determined from the following kinematic expression,

$$z = \frac{1}{2} a_z t_0^2, \tag{17}$$

where z is the distance traveled by the ion and t_0 is the time over which the particle is accelerated by the external field. Substituting our expression for a_z and solving for t_0, we obtain the following expression,

$$t_0 = \sqrt{\frac{2z}{a_z}} = \sqrt{\frac{2mz}{qE_z}} \propto \sqrt{\frac{m}{q}}. \tag{18}$$

The time, t_0, shown in (Eq. 18) does not include the field-free region the particles passes through prior

to reaching the detector. The total time of flight, t, can be represented as,

$$t = t_0 + \frac{L}{v} = \sqrt{\frac{2mz}{qE_z}} + \sqrt{\frac{mL}{2qE_z}} \propto \sqrt{\frac{m}{q}}, \tag{19}$$

where L is the distance from the beginning of the field-free region to the charge particle detector, and v is velocity of the charge particle at the beginning of the field-free region. After neglecting gravity ($a_z >> g$) and substituting for v, the total time of flight portrayed in Eq. 19 demonstrates that the total time of flight is proportional to the square root of the mass to charge ratio. Effectively, this acts as a charged particle spectrometer, separating species based on this ratio.

2.4.4 Microchannel Plate Detectors

The charged particle detectors utilized for these experiments are microchannel plate detectors (MCPs). They are composed of many small glass capillaries, fused together, and sliced into thin plates. Upon applying a voltage across the MCP, charged particles incident upon a channel are accelerated and collide with the walls of the channel. These collisions create secondary electrons, and the subsequent cascading electrons create a current that can be subsequently amplified by an additional MCP. This configuration is known as a chevron configuration. A bias voltage drop of $\approx$ 1kV across each plate is required to achieve sufficient sufficient signal (10mV) for the experiments.

2.5 Data Acquisition and Analysis

The time-dependent electron current from the MCPs is directed into an SRS DC-350 MHz pre-amplifier prior to being digitized by an Agilent u1071A. There are several LabView 2015 programs written by current and previous members of the lab with oscilloscope features that allow one to see and record the time-of-flight spectrum of positive ions in the detection chamber. These LabView programs enable one to determine the following: focused laser intensity at the molecular beam, correct timing between multiple laser pulses, and two-color phase calibration. Additional LabView programs were also written to perform laser pulse temporal diagnostics (FROG, autocorrelation, etc). Separate LabView programs were written for conducting the pump-probe molecular alignment and orientation discussed in this dissertation. The details of the pump-probe program will be discussed in more detail in the the next chapter.

3 Detecting Transient Orientation of OCS

After discussing the experimental apparatus, we move to describing the pump-probe technique used for detecting and characterizing molecular orientation. Typically, for these type of experiments, a pump laser pulse initiates the rotational dynamics, and a second time-delayed probe pulse reads out the orientation of the molecular ensemble.

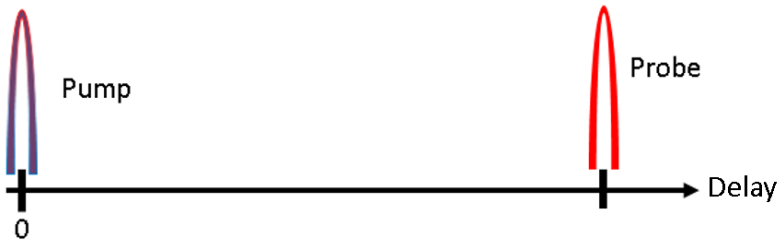

Figure 3.1: Cartoon of the pump-probe scheme.

3.1 Probing Field-free Orientation of OCS

Determining the net orientation of a molecular ensemble requires measuring a quantity that can distinguish its head and tail ends. For a linearly polarized single-colored probe pulse with more than one or two cycles, the negative and positive electric field cycles of the laser pulse have roughly equal amplitudes. Accordingly, the net yield of any strong field ionization process, integrated over the multi-cycle probe pulse, will be independent of the molecular orientation in the lab frame. However, detection of charged molecular fragments, resulting from strong field multi-electron dissociative ionization (MEDI), can reveal preferential orientation of the sample. Figure 3.2 depicts the time-of-flight (TOF) configuration for detecting S^{+3} produced via "Coulomb explosion". Coulomb explosion describes the rapid separation (due to mutual repulsion) of positively charged ion fragments following the removal of multiple electrons from a molecule in an intense short laser pulse, and the subsequent positive charge localization on different ends of, or sites within, the molecule. S^{+3} ions are well suited for the orientation measurements because they are highly directional, i.e. they are primarily produced when the molecular axis is within a narrow cone centered on the probe laser polarization[7], and within our spectrometer, their time-of-flight distribution is not contaminated by other species with identical or similar, charge to mass ratios. For OCS molecules preferentially aligned along

the probe laser polarization, the explosion propels S^{+3} ions either directly toward or away from the MCP detector. A static electric field of a few hundred V/cm applied to the interaction region pushes all positive ions produced in the interaction region toward the MCP detector. Ions ejected away from the detector have their momentum reversed and arrive at the detector a few tens of ns after the ions that are ejected toward the detector.

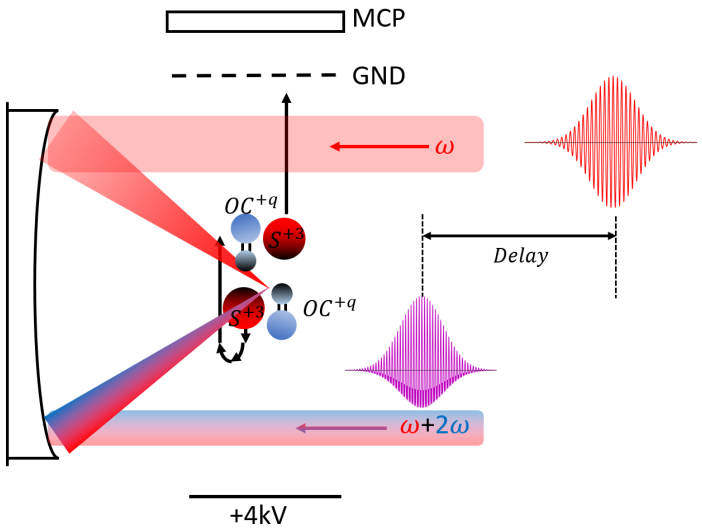

Figure 3.2: Schematic of the time-of-flight configuration for detecting S^{+3} generated via Coulomb explosion. The temporal profiles of the laser field of high intensity probe and two-color pulse are shown, where the black lines for each indicate zero field amplitude. For OCS molecules aligned along the probe laser polarization, S^{+3} ions are ejected toward or away from the MCP detector. A static field applied to the interaction region guides all the positive ions toward the detector.

Accordingly, preferential orientation of the S-atom in OCS toward or away from the detector can be discerned by observing the two distinct S^{+3} TOF peaks as shown in Figure 3.3. We define an asymmetry parameter ζ to quantify the direction and magnitude of the orientation as follows:

$$\zeta = \frac{Y_f - Y_b}{Y_f + Y_b}, \tag{20}$$

where Y_f and Y_b are the forward and backward yields normalized to the respective S^{+3} yields with the two-color pulse blocked. This normalization for each S^{+3} fragment yield helps to minimize changes in the yield due to neighboring ionic species (C^+), slightly different detection efficiencies for forward and backward ions, and electronic noise.

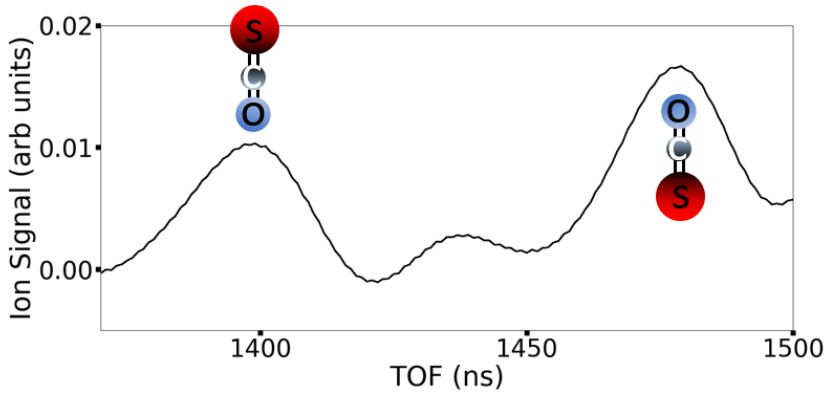

Figure 3.3: Measured S^{+3} time-of-flight signal. The early (late) S^{+3} peaks correspond to molecular orientations with the S-atom closer to (further from) the MCP detector. The small peak centered near 1440 ns is an electronic artifact from the detection system.

3.2 Two-Color Phase (ϕ) Calibration

By combining a linearly polarized 800nm (ω) pulse with its colinearly polarized 400nm (2ω) second harmonic, we can generate a two-color pulse with an asymmetry in the maximum field in the positive and negative directions along the laser polarization axis. Changing the direction of the field maxima, and the ratio of the maxima in the forward and backward direction, is routine by varying the relative phase (ϕ) of the 800 and 400nm component pulses. This can be accomplished by tuning the relative optical path length of the two beams. After the 800nm pulse passes through a 100μm thick BBO doubling crystal, there is a $\approx$ 20fs delay between the intensity maxima of the 800nm and newly generated 400nm pulses due to differences in the group velocities of the 800nm and 400nm components. Since the pulses pass through a vacuum chamber window, additional delay is added between the red (800nm) and blue (400nm). We exploit the birefringence in an additional calcite plate to compensate for the group delay walk off between the red and blue pulses as they propagate toward the interaction region. Specifically, we orient the calcite crystal such that its index of refraction is smaller for the blue pulse than the orthogonally polarized red pulse as shown in Table 1.

Calcite exhibits extraordinary and ordinary crystal axes. Light polarized along the extraordinary and ordinary axis will experience an index of refraction of n_e and n_o, respectively. From Table 1, having the 400nm (800nm) pulse polarized along the extraordinary (ordinary) axis allows for compensating the group

	n_e	n_o
400nm	1.5395	~~1.7737~~
800nm	~~1.4920~~	1.6737

Table 1: Group indices of refraction for calcite at $\lambda = 400$, 800nm[54] at normal incidence. Note that n_e changes by a factor of 1.0003 for a 1 degree deviation from normal incidence.

delay offset between the red and blue pulses. Small variations of the calcite angle alter the relative optical path length between the red and blue allowing for control of the relative two-color phase (ϕ). A diagram of the optical setup is shown in Figure 3.4.

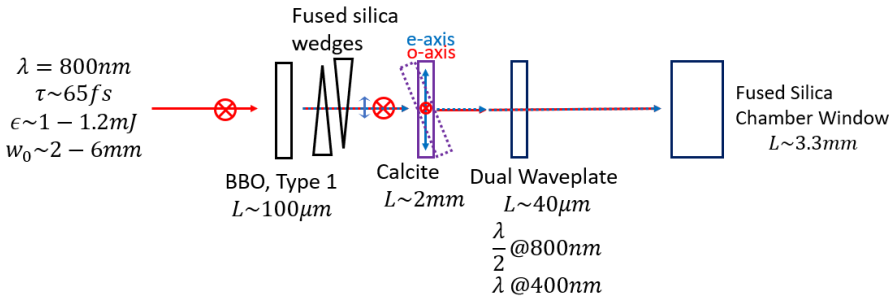

Figure 3.4: Schematic of approach used to create two-color phase-locked asymmetric laser fields. The calcite plate is mounted on a precision rotation stage, which enables fine control of the two-color phase (ϕ). The change in path length by tilting the calcite crystal is sufficiently larger compared to the change in path length due to the change in the extraordinary index of refraction. Typical single-color laser beam characteristics (central wavelength: λ, pulse duration: τ, pulse energy: ϵ, and d_0: incident beam diameter) are shown. The dual waveplate alters the polarization of the two beams as noted, and ensures that the polarization of the two-color laser pulse is nearly linear and lies along the axis of the time-of-flight spectrometer. The 400nm exiting the dual waveplate is slightly elliptically polarized with the amplitude along the axis of the spectrometer reduced by $\approx$ 5%[55]. The red circle with an X and the blue double-ended arrows shown prior to the calcite plate indicate the polarization directions of the 800nm and 400nm pulse, respectively. L represents the thickness of the specified optical element.

To calibrate ϕ for the two-color pulse, we measure the change in the single ionization yield of helium from its average and the asymmetry parameter for the production of N^{+2} fragments in the $N_2(2,1)$ channel via Coulomb explosion of N_2, and S^{+3} from OCS, as a function of ϕ (Figure 3.5). Note that the $N_2(2,1)$ channel is defined as:

$$N_2(2,1) = N^{+2} + N^{+1}$$

The relative change in the He^+ yield shows clear maxima (minima) corresponding to ϕ of 0,π,2π (π/2,3π/2), where the two-color field asymmetry and the strong-field ionization rate are the largest (smallest). Previous ϕ-dependent measurements of N^{+2} from $N_2(2,1)$ determined that positive (negative) extrema $\zeta_{N(2,1)}$ correspond to $\phi = 2M\pi((2M+1)\pi)$ for integer M[56, 57]. This calibration indicates that the negative extrema in ζ for S^{+3} corresponds to $\phi = 0$ ($2M\pi$). With respect to the laboratory fixed frame, $\phi = 2M\pi((2M+1)\pi)$ produces a two-color field maxima toward (away) from the MCP detector. For convenience, in measurements with fixed phase, we assume M=0 such that the asymmetry parameter maxima toward (away) from the detector define $\phi = 0(\pi)$. To ensure the same relative phase between the red and blue fields throughout

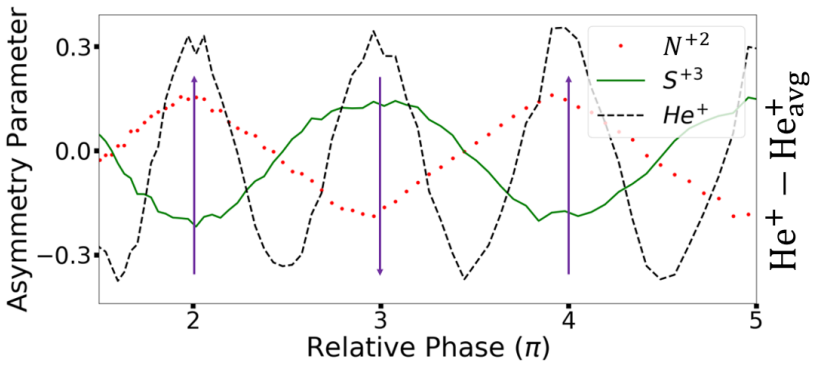

Figure 3.5: Two-color phase (ϕ) calibration. Positive (negative) values of ζ indicate preferential fragment ejection toward (away) from the MCP detector. The black dashed curve shows the difference of He^+ yield from its average. The purple arrows indicate the direction of the two-color field maxima with "up" on the plot corresponding to the detector direction.

the pulse, it is important to use a sufficient thin and properly oriented BBO doubling crystal so that the bandwidth of the blue pulse is not limited by phase matching and that the center of the blue spectrum has a wavelength that is one-half that of the center of the red spectrum[11]

3.3 Intensity Calibration

To maintain a constant blue:red pulse energy ratio, the focused two-color intensity was varied by adjusting an aperture placed prior to the beam's entry into the TOF chamber. For a given aperture setting, the pulse energy (ϵ), incident beam diameter (d_0), and ion yields were measured. These measurements were first performed using a single color pulse (λ=800nm) to compare with previous intensity calibrations using

OCS[4] and O_2[58] gas targets. The pulse energy and beam diameter were used for computing a relative intensity of the focused beam, which scales as $\epsilon \cdot d_0^2$. Since the area of the focused beam decreases as $\frac{1}{d_0^2}$, the ion yield were scaled by d_0^2 to measure ion yield vs intensity. Following the method used in Sandor et al.,[4], we separately fit the high and low-intensity portions of the measured yields to curves of the form αI^β, where I is the peak intensity of the laser pulse. The saturation intensity is defined by the point of intersection of the two curves which takes the form of straight lines on a log-log plot of ion yield vs intensity. Using the O_2^+ yield (from background O_2 molecules in the chamber) as a function of relative intensity, we convert relative to peak intensity by scaling the intensity axis by a constant, so that the newly determined saturation intensity matches that from previous measurements of O_2^+[58]. Using that calibration, the saturation intensity of OCS is determined to be 74 ± 7 TW/cm^2 at λ= 800nm, in good agreement with the previous measurement of $70 TW/cm^2$[4] at λ= 800nm. After calibrating the intensity (at the laser focus) for each aperture diameter, the two-color saturation intensity can be determined after repeating the yield vs aperture diameter measurement with the two-color pulse as shown in Figure 3.6. We define the peak two-color intensity as the sum of the red and blue peak intensities. This yields a saturation intensity of 40±4 TW/cm^2 for OCS for $\phi = 0$(or π).

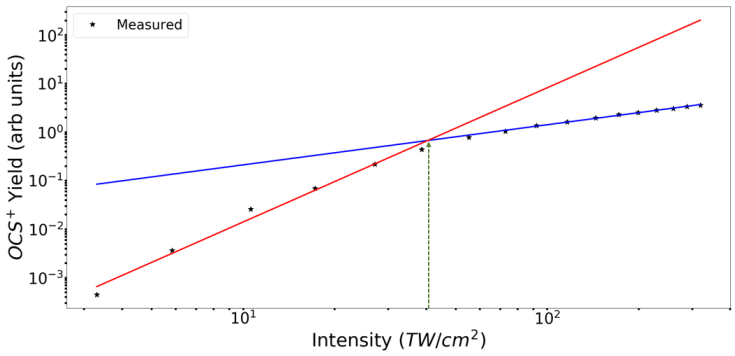

Figure 3.6: Measured OCS^+ yield vs. two-color (λ=400+800nm) laser peak intensity for an isotropic OCS target. The ratio of the 800nm to 400nm pulse energy is 3:1. The red and blue lines show the fits to the pre- and postsaturation slopes. The green dashed arrow shows the extracted saturation intensity.

3.4 Characterizing Transient Orientation of OCS

Following exposure to an intense laser pulse, the degree of alignment and/or orientation of a molecular ensemble changes with time due to the coherent evolution of the rotational wave packets excited within individual molecules. While the ensemble averaged time-dependent angular distribution provides the most complete description of the sample, specific moments of that distribution offer convenient metrics of the degree of alignment or orientation along a particular space fixed axis. For example, the ensemble averaged expectation value of $cos(\theta)$, which is proportional to the projection of the permanent dipole moment along the laboratory z-axis, is often used to quantify the degree of orientation at any given instant in time. Note that in the experiments described in this dissertation, the z-axis is defined by the spectrometer axis and the probe laser polarization, with +z pointing upward in the lab frame. Unfortunately, performing accurate measurements of $< cos(\theta) >$ is difficult and time-consuming. Accordingly, we use a different metric that, in principle, allows us to characterize (in a single laser shot) the probability of finding an OCS molecule with its dipole moment pointing up, rather than down, at a particular instant in time.

Specifically, we use the normalized yield difference of the S^{+3} fragment ions produced via Coulomb explosion, previously defined as the asymmetry parameter in Eq. 20, to quantify the degree of orientation in the OCS sample during the intense probe. Roughly speaking, only molecules whose axes are aligned within a narrow cone centered on the probe laser polarization undergo Coulomb explosion via enhanced ionization[7, 43, 56, 59], so the asymmetry or "orientation parameter" is a measure of the probability that OCS molecules aligned along the spectrometer axis have their S atoms pointing up (rather than down) during the probe pulse. But to enable direct comparisons between experiment and theory/simulation, we need a more precise mapping of S^{+3} signal to OCS orientation, taking into account: the angle-dependent Coulomb explosion probability; the angular acceptance of our time-of-flight spectrometer (S^{+3} fragments ejected perpendicular to the spectrometer axis do not necessarily impact the detector); the potential re-alignment of the molecules during the probe pulse; and the possible breakdown in the axial recoil approximation (S^{+3} fragment trajectories not parallel to the molecular axis due to the rotational velocity of the molecules prior to Coulomb explosion).

Fortunately, we do not need to characterize each of these factors separately. Instead, their combined

effect on the measured orientation parameter is contained in the angle-dependent S^{+3} detection probability, $\Sigma(\theta)$. We determine $\Sigma(\theta)$, for a probe pulse with the same intensity and pulse duration as those used in the orientation measurements, by measuring the S^{+3} signal as a function of delay following a non-ionizing single-color alignment pulse. Using the methods demonstrated in Sandor et al.[4], we fit the delay-dependent signal to moments of the (readily calculated) rotational angular distribution. Those fits determine the angle-dependent detection probability function, $\Sigma(\theta)$, which can be used to extract a simulated orientation parameter that can be directly compared to experiments.

3.4.1 Extracting the Angle-dependent Detection Probability of S^{+3}

Following the method outlined in Sandor et al[4], equation 21 defines the mathematical relationship between the normalized S^{+3} yield, $Y(t)$, and $\Sigma(\theta)$ as

$$Y(t) = \int_0^\pi \Sigma(\theta) S(\theta, t) \sin(\theta)\, d\theta, \tag{21}$$

where $S(\theta, t)$ is the delay-dependent ensemble average of the angular probability distribution and $\Sigma(\theta)$ is the angle-dependent detection probability, which we wish to extract from measurements of Y(t). To extract $\Sigma(\theta)$ from measurements of $Y(t)$, we calculated $S(\theta, t)$ for a thermal ensemble of rigid molecular rotors with rotational temperature, T_{rot}, exposed to an alignment pulse with a known time-dependent intensity. The diameter of the focused alignment beam is several times larger than that of the probe, so we assume all molecules experience the same peak alignment intensity. $\Sigma(\theta)$ can be expressed in terms of a set of real functions $f_k(\theta)$,

$$\Sigma(\theta) = \sum_k a_k f_k(\theta). \tag{22}$$

Thus $Y(t)$ can be written

$$Y(t) = \sum_k a_k M_k(t), \tag{23}$$

where a_k are real coefficients and the $M_k(t)$ moments of $S(\theta, t)$ with respect to expansion functions $f_k(\theta)$ such that,

$$M_k(t) = \int_0^\pi f_k(\theta) S(\theta, t) \sin(\theta)\, d\theta. \tag{24}$$

$M_k(t)$ can be calculated if $S(\theta, t)$ is known, allowing one to fit measurements of $Y(t)$ to obtain the expansion coefficients a_k and recover $\Sigma(\theta)$. Further details on the technique and its limitations can be found in Sandor

et al [4]. Since the OCS molecules were aligned and not oriented, $\Sigma(\theta) = \Sigma(\pi - \theta)$ for $0 \leq \theta \leq \pi$. For convenience, we select basis functions, $f_k(\theta)$, that exhibit a maximum in the ionization probability for molecules preferentially aligned along the laser polarization. Specifically, we write

$$\Sigma(\theta) = a_0 + a_1 \cos^2(\theta) + a_2 \cos^4(\theta) + ... \tag{25}$$

To perform the fits, $S(\theta, t)$ was first calculated by solving the time-dependent Schrödinger equation [2] with rotational constant $B_{OCS} = 0.2028cm^{-1}$[60], anistropic polarizability $\Delta\alpha$=27 a.u.[61], a temporal Gaussian envelope intensity profile with peak intensity I, and the initial rotational temperature T_{rot} of the thermal ensemble. The best fit coefficients, a_k, were determined using a least-squares fit for a grid of (T_{rot},I). To determine the minimum number of fitting coefficients (a_k) needed for the best statistically relevant fit, we performed the F-test[62]. The F-test yields the probability that any improvement in the fit with k+1 fitting coefficients is due to chance and not because it is a better description of the data. If the test probability is higher than a threshold value (set at 5%), adding the extra term is statistically relevant. After performing the F-test, we found that 3 terms are statistically relevant for fitting, so only 3 basis functions [1,$\cos^2(\theta)$,$\cos^4(\theta)$] were included in the fits. The results of the fit are shown in Figure 3.7. Values for each fitting parameter along with their corresponding uncertainties are shown in the caption. The data points in Figure 3.7 are the result of averaging five independent Y(t) measurements. The uncertainties in each fitting parameter were determined by computing an error or covariance matrix[62]. A polar plot of $\Sigma(\theta)$ is shown in Figure 3.8. The uncertainty in the probability at each angle is shown using a grayscale shading in the radial direction. The shading uses the fitting coefficients and their corresponding uncertainties to generate a large set of angular dependences using randomly varied coefficients following a Gaussian probability distribution about their best-fit values. Using the randomly generated angular distributions, a histogram at each angle shows the probability of various radial distances from the best fit as a gray-scale density plot. As expected, the detection probability is strongly peaked along the probe polarization axis. However, there is a non-zero probability of detecting S^{+3} fragments from molecules aligned off-axis, including those perpendicular to the laser polarization.

With the fitting coefficients for $\Sigma(\theta)$ determined, the measured orientation parameter can be directly compared with a calculated orientation parameter, ζ_c(t), defined as:

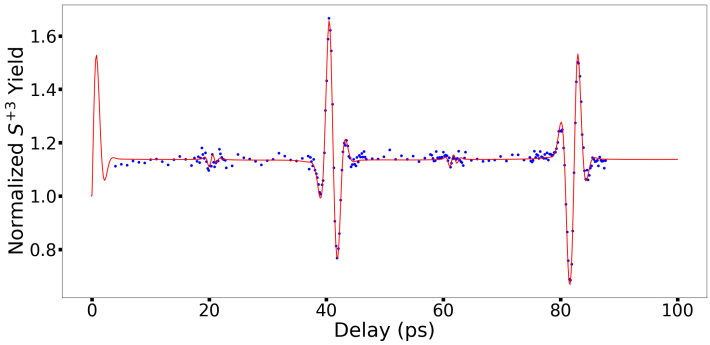

Figure 3.7: Normalized S^{+3} Yield [Y(t)] versus alignment-ionization pulse delay. The blue dots are measurements and the solid red curve is a best fit to the data. Best fit coefficients: a_0=0.52±0.03, a_1=0.51±0.35, a_2=1.58±0.41 for rotational temperature (T_{rot})=17K and peak intensity (I) = $27TW/cm^2$. The recovered values of I and T_{rot} are in reasonable agreement with those estimated from measured laser beam properties and from typical performance of the Even-Lavie valve, respectively.

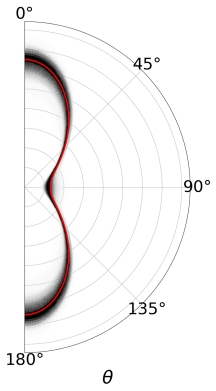

Figure 3.8: Extracted $\Sigma(\theta)$ from the fit in Figure 3.7. $\Sigma(\theta)$ indicates that S^{+3} emission peaks when the high intensity probe laser field is polarized along the molecular axes and is highly directional as we would expect from Coulomb explosion preceded by enhanced ionization. The grayscale shading represents the experimental uncertainty distribution associated with the errors of the coefficients, a_k.

$$\zeta_c(t) = \frac{\int_0^{\pi/2} \Sigma(\theta)|\psi(\theta,t)|^2 \sin(\theta)\, d\theta - \int_{\pi/2}^{\pi} \Sigma(\theta)|\psi(\theta,t)|^2 \sin(\theta)\, d\theta}{\int_0^{\pi/2} \Sigma(\theta)|\psi(\theta,t)|^2 \sin(\theta)\, d\theta + \int_{\pi/2}^{\pi} \Sigma(\theta)|\psi(\theta,t)|^2 \sin(\theta)\, d\theta}, \tag{26}$$

where $|\psi(\theta,t)|^2$ (not to be confused with $S(\theta,t)$) is the delay-dependent ensemble average of the rotational probability distribution through the interaction of an intense two-color laser pulse.

3.4.2 Measuring Field-Free Orientation of OCS

The pump-probe scheme outlined at the beginning of this chapter is the basis for measuring field-free orientation. An experimental schematic is shown in Figure 3.9. A 50/50 beamsplitter is used to create two

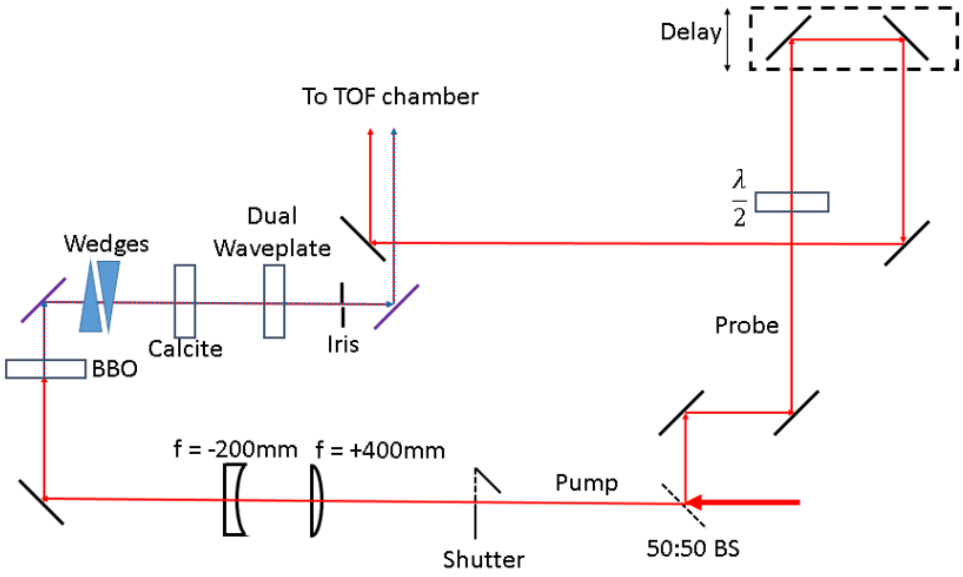

Figure 3.9: Schematic of the two-color orientation experimental setup. Typical pulse energy after the compressor: 2.5mJ; repetition rate: 1kHz; pulse duration: 35fs; and λ: 800nm. Focused probe intensity in the interaction region: $350 TW/cm^2$

beams, which we call the pump and probe. The probe beam goes through a halfwave plate to rotate its polarization to be parallel to the axis of the spectrometer. A pair of mirrors on a motorized stage (Thorlabs Z825B) varies the probe beam's optical path length, controlling the pump-probe delay. A mechanical shutter is inserted into the pump beam path, and data is collected with and without the two-color pump beam (in alternating 350 laser shot bins). The pump beam's diameter is reduced by a factor of two prior to entering the Type-1 BBO (SHG) crystal. The calcite plate and fused silica wedges are added to compensate for the group delay offset between the 400 and 800nm pulses after exiting the BBO crystal and passing through a vacuum window. The dual waveplate acts as a half-wave plate for the 800nm pulse and a full-wave plate for the 400nm pulse. Rotating the waveplate about the beam propagation direction rotates the polarization for the red (800nm) while leaving the blue's (400nm) polarization unchanged. Both the red and blue pulses are polarized along the axis of the time-of-flight (TOF) spectrometer. An iris is placed in the two-color

beam path to control the peak intensity of the focused beam. Reducing the iris aperture lowers the focused intensity by reducing both the pulse energy and increasing the focal spot diameter. Both pump and probe beams enter the TOF detection chamber parallel to each other and perpendicular to the molecular beam. They are focused onto the molecular beam by an UV enhanced aluminum(f = +250mm) concave mirror (see Figure 3.2).

A homemade LabView program is the central piece for recording the data, depicted in Figure 3.10. The

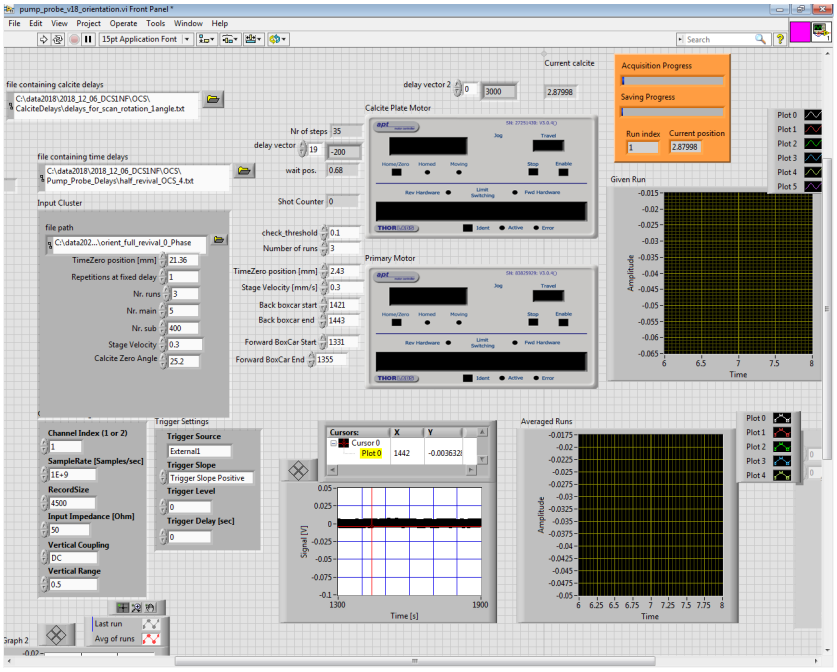

Figure 3.10: LabView pump-probe program for measuring field-free orientation. Under the "Input Cluster" section: TimeZero position refers to the stage position where the relative delay between the pump and probe is zero. Nr. runs: total number of delay scans to repeat. Nr. sub: total number of lasers shots to average (= 1 trace) at a given pump-probe delay. Nr. main: total number of traces to acquire. Calcite Zero Angle: Relative calcite angle in degrees.

program controls the motion of the delay stage in the probe beam line and records the digitized TOF traces from an Agilent u1071A at the specified pump-probe delay. The user can set the time delay values, number of laser shots to average at every delay to produce a single trace, the number of traces to average at each delay, and the number of delay scans to perform. An option for setting the relative calcite angle allows one to select the desired two-color phase. Finally, software based boxcar integrator gates are included, so the user can monitor the orientation parameter as a function of the pump-probe delay.

Figure 3.11 shows a measurement of the orientation parameter plotted as a function of the pump-probe delay near the second full revival time of OCS ($2T_{OCS}$). The red (dashed) and blue (solid) curves show two different two-color phases (ϕ). Mirror-like images of the revivals confirm that the rotational dynamics are sensitive to the direction of the two-color field maxima. Field-free orientation of OCS is observed near

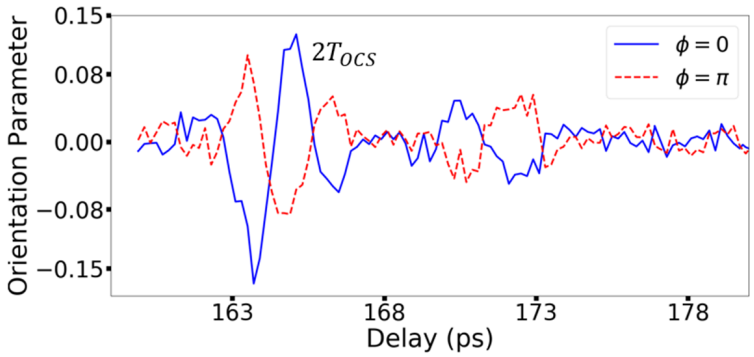

Figure 3.11: Field-free orientation measured near the second full revival time of $2T_{OCS}$. The insets illustrates the two-color phase.

its second full rotational revival time (≈164.4ps). Additional rotational revivals are observed centered near 171ps. Noteably, the minimum two-color intensity needed to observe field-free orientation of OCS near the expected revival times (i.e. T_{OCS}, $2T_{OCS}$,...) also produces measurable OCS ion signal. Accordingly, we know that the probe pulse interacts with both OCS and OCS^+. Indeed, as described in more detail below and in Chapter 4, the additional revivals can be attributed to probe induced Coulomb explosion of OCS^+ ions created during the two-color pump pulse.

To determine the molecular species contributing to these additional rotational revivals, we first compared the observed revival times to those expected from known (or estimated) rotational constants of different electronic states of OCS, OCS^+, OCS dimers, and OCS^+He clusters and simulated the field-free evolution of the rotational wavepacket following a two-color interaction. The experimental revival time best matches that expected for OCS^+ molecules in the $^2\Pi_{3/2}$ state. Figure 3.12 shows a simulation of the field-free evolution of a two component molecular ensemble, one with a constant equal to that for OCS ground state (B=0.2028cm^{-1}), and the other with a rotational constant equal to OCS^+ $^2\Pi_{3/2}$ X state. The two simulated curves shown in

red and black are distinct in that they adopt the rotational structure associated with a $^2\Pi$, $^1\Sigma$ molecular ion, respectively. A full description of the mathematical expressions used for performing the simulated two-color interaction of each type of molecular ion will be discussed in Chapter 4. Figure 3.12 compares measurements

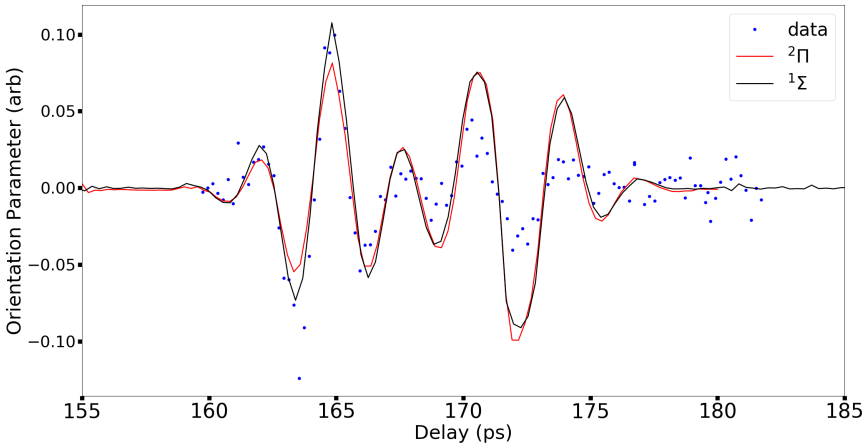

Figure 3.12: Field-free orientation measured near the second full revival time of OCS ($2T_{OCS}$). The red or black curves represent the calculated field-free evolution of the neutral and ion wavepacket assuming the ion is a $^2\Pi$ or $^1\Sigma$ molecular ion, respectively.

of the orientation parameter in blue points with the calculated parameter assuming a $^2\Pi$ or $^1\Sigma$ molecular ion. The phase and amplitude of the rotational revivals for both simulations near 171ps show reasonable agreement with the data. Indeed, this is expected as 171 ps corresponds to an integer revival for both $^1\Sigma$ and $^2\Pi$ molecular ion rotational states with the appropriate rotational constant. However, we also measured and performed simulations of the orientation parameter near T_{OCS} to see if the agreement between the two types of simulations and the measurement is preserved. For a $^1\Sigma$ ($^2\Pi$) molecule, its rotational revivals occur at time t=π/B ($2\pi/B$), where B is the rotational constant. Therefore at t=π/B, the relative phases of the rotational wavepackets in $^1\Sigma$ and $^2\Pi$ molecular ions differ by π, meaning their respective rotational revival structures should be π out of phase. Figure 3.13 shows the measured orientation parameter near T_{OCS} (blue dots) along with the simulation curves assuming the creation of $^2\Pi$ and $^1\Sigma$ molecular ions (with the same rotational constant corresponding to that of the $^2\Pi_{3/2}$ X state, B=0.1942 cm^{-1}). The simulated results confirm the π phase difference between the $^1\Sigma$ and $^2\Pi$ rotational revivals. The orientation revival structure associated with $^2\Pi$ molecules clearly exhibits better agreement with the data as compared to that of the $^1\Sigma$

simulation.

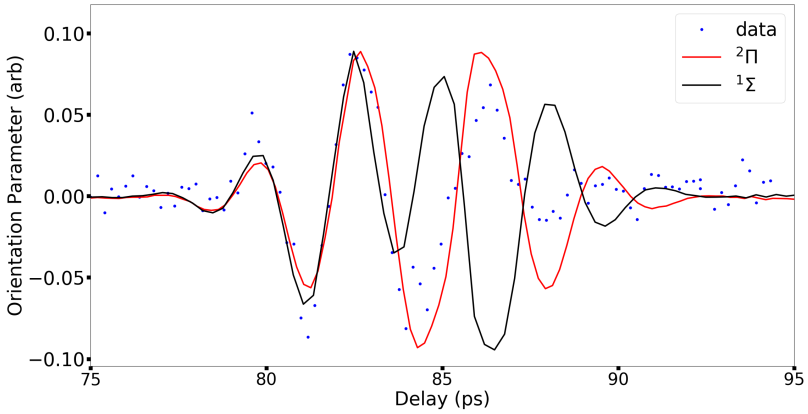

Figure 3.13: Field-free orientation measured near the first full revival of OCS (T_{OCS}). The red and black curves show the calculated orientation parameter for a mixed ensemble of neutral and ion wavepackets assuming the ion is in a $^2\Pi$ and $^1\Sigma$ electronic state, respectively. In both cases, the rotational constant of the ion is equal to that of the $^2\Pi_{3/2}$ state.

Recall from the introduction [section 1.4.2] that the X-state of OCS^+ has a non-negligible spin-orbit splitting. The two component states, $^2\Pi_{3/2}$ and $^2\Pi_{1/2}$, have different rotational constants, which are listed in Table 5. To determine the degree to which each ground state contributes to the orientation revival, a

Species	Rotational constant, B (cm^{-1})
OCS	0.2028±0.0001
$^2\Pi_{3/2}$ OCS^+_X	0.1946±0.0006
$^2\Pi_{1/2}$ OCS^+_X	0.1983

Table 2: Rotational parameters of the OCS ground state[60] and the X-state of OCS^+[36]. The quoted rotational constant and uncertainty for OCS^+_X is the average and standard deviation of the measurements listed in [36]. Note that only one measurement of the $^2\Pi_{1/2}$ rotational constant was reported, so no error bars were included in the table.

plot of the calculated orientation parameter for each component of the ground state doublet is shown in Figure 3.14. The rotational constant associated with the $^2\Pi_{3/2}$ state has a rotational revival time that best matches the experimental data. Based on our full analysis, we conclude that the additional orientation revival is associated with OCS^+, and that ions in the $^2\Pi_{3/2}$ state are predominantly produced via strong-field

ionization in the two-color field. Given that there is no evidence for appreciable creation of OCS ions in $^2\Pi_{1/2}$ or in any electronic state other than $^2\Pi_{3/2}$, unless otherwise state, for the remainder of this dissertation it is assumed that the molecules under investigation remain in the OCS electronic ground state, or have been ionized to the OCS^+ $^2\Pi_{3/2}$ X state.

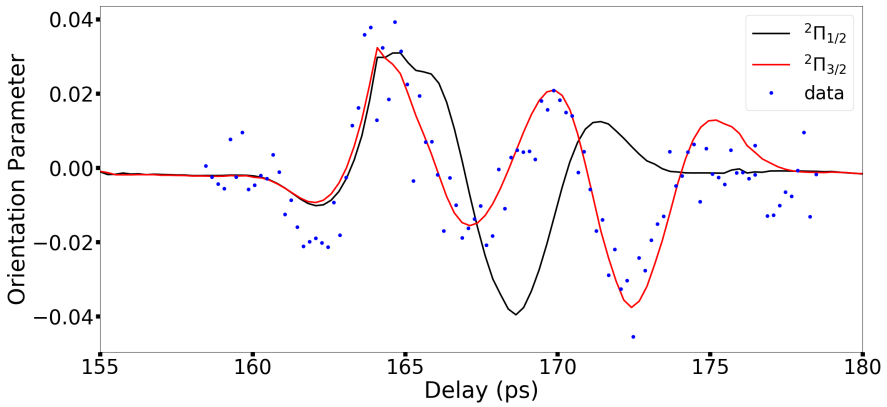

Figure 3.14: Field-free orientation of OCS and OCS^+ measured and simulated near the second rotational revival time of OCS (T_{OCS}). The red and black curves represent the calculated field-free evolution of the neutral and ion wavepacket assuming the ion is in the $^2\Pi_{3/2}$ ground state using the rotational constants for the $^2\Pi_{3/2}$ and $^2\Pi_{1/2}$ ground state, respectively.

When molecules are ionized by an intense, two-color laser field, the angle-dependent ionization probability is directly reflected in the angular probability distribution ($|\psi(\theta,t)|^2$) of the ions and surviving neutrals. By observing the evolution of the neutral and newly created ion rotational wave packets we can extract the angle-dependent single-ionization probability without directly measuring the single ionization yield for molecules with well-defined orientations relative to the ionizing field. The next chapter in this thesis will discuss our approach for extracting the angle-dependent single-ionization probability of OCS from the measured delay-dependent orientation parameter.

4 Modeling Transient Orientation of OCS and OCS^+

Two-color laser fields can induce field-free alignment and orientation via the field's interaction with the molecular polarizability, hyperpolarizability, and through angle-dependent ionization. These interactions can coherently redistribute population among the rotational states, impacting the time-dependent rotational distribution of molecules in the ensemble. The effects of the polarizability and hyperpolarizability interactions on the rotational distribution have been well documented[2, 3, 8, 33, 34], and we have developed a model of rotational redistribution due to angle-dependent single ionization for OCS and OCS^+. After including all three interactions, we compute a delay-dependent orientation parameter, $\zeta_c(t)$, as shown in equation 27, to directly compare with the corresponding measurements. We define

$$\zeta_c(t) = \frac{\int_0^{\pi/2} \Sigma(\theta)|\psi(\theta,t)|^2 \sin(\theta)\, d\theta - \int_{\pi/2}^{\pi} \Sigma(\theta)|\psi(\theta,t)|^2 \sin(\theta)\, d\theta}{\int_0^{\pi/2} \Sigma(\theta)|\psi(\theta,t)|^2 \sin(\theta)\, d\theta + \int_{\pi/2}^{\pi} \Sigma(\theta)|\psi(\theta,t)|^2 \sin(\theta)\, d\theta}, \tag{27}$$

where $\Sigma(\theta)$ is the experimentally determined angle-dependent S^{+3} detection probability (see section 3.4.1), $|\psi(\theta,t)|^2$ is the calculated angular probability distribution of the ensemble after the two-color ionizing field (composed of neutral OCS and newly created OCS^+), and θ is the angle between the molecular dipole moment and up in the lab frame (the direction of the maxima in the two-color field).

To calculate $|\psi(\theta,t)|^2$, we solve the time-dependent Schrödinger equation (TDSE) for each initial rotational state within a thermal distribution of neutral OCS molecules. The next section will introduce the Hamiltonian and discuss how the ionization model influences the angular probability distribution of the neutrals and ions. Unless otherwise stated, the equations and molecular parameters are expressed in atomic units.

4.1 Neutral Rotational Distribution Evolution

Recall from Section 1.4.1 that for a linear molecule in a $^1\Sigma$ electronc state (like the OCS ground state) the neutral rotational wavepacket, $\psi_n(\theta,t)$, created from a single or coherent superposition of initial rotational states by a two-color field can be expressed as,

$$\psi_n(\theta,t) = \sum_{J,M} d_n^{JM} e^{-iU_n^J t} \left|J,M\right\rangle, \tag{28}$$

where d^{JM} is the probability amplitude for occupying rotational state $|J, M\rangle$. U_n^J is the rotational energy of a neutral state, with total angular momentum (and total rotational angular momentum) J. The complex exponential, $e^{-iU_n^J t}$, describes the phase advance of each rotational state within the wavepacket, and the subscript, n, designates the neutral molecular species. Equation 29 gives the TDSE for the neutrals,

$$i\dot{\psi}_n(t) = [B_n J(J+1) + V_n^{pol} + V_n^{hyp} + iV_n^{ioniz}]\psi_n(t), \tag{29}$$

$$V^{pol} = \frac{-1}{4} E_\omega^2(t)(1+\gamma^2)(\Delta\alpha \cos^2\theta), \tag{30}$$

$$V^{hyp} = \frac{-1}{8}\gamma\cos(\phi)E_\omega^3(t)[3\beta_\perp \cos\theta + (\beta_\parallel - 3\beta_\perp)\cos^3\theta], \tag{31}$$

$$V_n^{ioniz} = \frac{-1}{2}K(t)[\Gamma(\theta) + 0.045\Gamma(\pi-\theta)], \tag{32}$$

$$K(t) = [I(t)/I_s]^{2.75}, \tag{33}$$

where $B_n J(J+1)$ is the rotational energy of the neutral molecule residing in state J, V^{pol} and V^{hyp} (equation 30 and 31) are the polarizability and hyperpolarizability interactions, respectively[2, 33, 34]. V_n^{ioniz} is the ionization interaction for the neutral. Table 3 provides descriptions of the parameters in equations 29-33. Ionization of the neutral depicted in equation 32 is simulated using a complex absorbing potential to model neutral population loss[33]. The complex potential removes probability amplitude as a function of θ, simulating the effects of population loss due to ionization. The $K(t)$ term, defined in equation 33, gives the ionization rate as a function of two-color intensity, I(t). To determine the correct scaling of the ionization rate with intensity, we measured the OCS^+ yield vs intensity (see section 3.3) and found that it increased as $I^{2.75}$, for I below the saturation intensity, i.e. at intensities where spatial volume effects do not affect the intensity dependent yield. The scaling factor, I_s, was chosen so that the calculated ionization probability saturates at the same intensity for which the onset of spatial volume effects were observed in the measured ionization yield. Scaling the measured yield by a constant allows direct comparison of the calculated and measured ionization probabilities. Figure 4.1 shows the measured and calculated (using Eqs. 29-33) ionization probability of OCS as a function of two-color intensity.

The angle-dependent portion of the ionization rate in equation 32 contains two terms. The first term defines ionization from a two-color field whose polarity, deemed (+), points up in the lab frame, and from the center of the molecule toward the S-atom for a molecule oriented with θ=0, as shown in Figure 4.2 .

Parameter	Description
$E_\omega(t)$	Laser field profile of the fundamental
$E_{2\omega}(t)$	Laser field profile of the 2nd harmonic $= \gamma E_\omega(t)$
γ	$\frac{E_{2\omega}}{E_\omega}$−Ratio of the 2nd harmonic to the fundamental maximum field amplitude
ϕ	Two-color phase
B_n	Rotational constant of the neutral
B_i	Rotational constant of the ion
$\alpha_\perp$	polarizability component $\perp$ to the molecular axis from a field polarized $\perp$ to its axis
$\alpha_\parallel$	polarizability component $\parallel$ to molecular axis from a field polarized $\parallel$ to its axis
$\Delta\alpha$	polarizability anistropy: $\alpha_\parallel - \alpha_\perp$
$\beta_\perp$	hyperpolarizability component $\parallel$ to the molecular axis from a field polarized $\perp$ to its axis
$\beta_\parallel$	hyperpolarizability component $\parallel$ to the molecular axis from a field polarized $\parallel$ to its axis
K(t)	Ionization rate scaling function
$\Gamma(\theta)$	Angle-dependent portion of the ionization rate
a	Constant factor for ensuring total population normalization
I_s	Ionization rate scaling factor
N	Total number of ion bins
I(t)	Intensity profile of the two-color field: $(1+\gamma^2)\lvert E_\omega(t)\rvert^2$
ΔT	time interval of a single bin

Table 3: Description of laser and molecular parameters used for solving the time dependent Schrödinger equation

Given the highly non-linear dependence of the ionization rate on the field, the positive polarity portions of the two-color field are expected to dominate the ionization yield. However, ionization from the negative polarity portions of the pulse are not completely negligible, particularly at high intensities. The second term, $\Gamma(\pi - \theta)$, in equation 32 accounts for ionization from the opposite polarity of the two-color laser field.

The 0.045 factor in front of $\Gamma(\pi - \theta)$ was determined from calculating the ratio of the time-averaged ionization interaction for the negative polarity and positive polarity portions of the two-color field used in

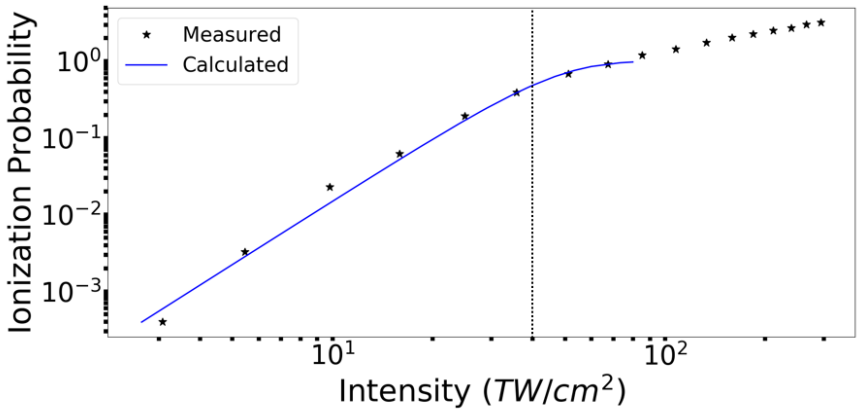

Figure 4.1: Calculated and measured ionization probability of OCS^+ vs. intensity. The intensity axis shows the peak intensity of the two-color laser pulse. The vertical dashed black line indicates the experimentally defined saturation intensity. For the measured probabilities larger than 1, a larger spatial focal volume, where additional molecules experiencing a lower peak intensity, contributes to the ionization signal.

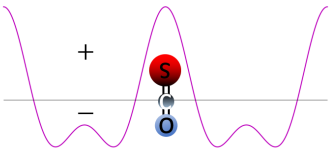

Figure 4.2: Cartoon of the polarity of the two-color field profile relative to the orientation of an OCS molecule with θ=0. The black horizontal line indicates zero-field amplitude. Positive (negative) fields point from the center of the molecule toward the S-atom (O-atom).

the experiments, i.e. for $\gamma = \sqrt{1/3}$ and $\phi = 0$, as shown in equation 34.

$$\frac{\langle E_-^{2*2.75}(t)\rangle}{\langle E_+^{2*2.75}(t)\rangle} \approx 0.045 \tag{34}$$

4.2 Ion Rotational Distribution Evolution

Figure 4.3 illustrates our strong field ionization model. Only non-dissociative single ionization is considered, since it was confirmed, experimentally, to be the dominant ionization channel at the two-color intensities used in this dissertation. Ionization is modeled by projecting the loss of the angular probability distribution from the neutrals ($|\psi_n(\theta,t)|^2$) to the newly created ions ($|\psi_i(\theta,t)|^2$).

The eigenstates of the neutral have total electronic angular momentum equal to zero and thus the molecules have only rotational angular momentum. The rotational angular momentum, j_r, and its projection on the lab z-axis, m_r, are equal to the total angular momentum, J, and projection of the total angular momentum on the lab z-axis, M, respectively. Ionization does not instantaneously alter the rotational angular probability distribution of the molecule, so the rotational state of the neutral, $|j_r, m_r\rangle$, must be projected onto the rotational angular probability distribution of the ion at each instant during the ionization process. The rotational states of the ion differ from those of the neutral due to the coupling of the remaining electrons' angular momentum to the rotational angular momentum upon ionization. The rotational eigenstates of the ion depend on the total angular momentum of the molecule, J', the projection of total angular momentum on the lab z-axis, M', and (since OCS^+ is a $^2\Pi$ molecule) Ω, the projection of the total electronic angular momentum on the molecular axis. Upon ionization, the ionized amplitude from each $|j_r, m_r\rangle$ in the neutral rotational distribution must be expressed as a product state of the ion ($|j_e, \Omega\rangle\,|j_r, m_r\rangle$)[38]. Implicitly, the departing electron carries away an angular momentum that is equal and opposite to the electronic angular momentum of the ion. We must then express the rotational part, $|j_r, m_r\rangle$, of each of those product states, in terms of the ion rotational eigenstates which are symmetric and antisymmetric linear combinations of states of the form, $|j_e, \Omega, j_r, J', M'\rangle$. The total ion angular momentum, J', and its projection in the lab frame z-axis, M', are half integer, with $|j_r - j_e| \leq J' \leq j_r + j_e$. Accordingly, ionization of a neutral rotational state populates a linear combination of ion states with different final total angular momentum (with the ionized electron carrying the difference between the total angular momentum of the ion and neutral). We only consider the coupling of an electron with angular momentum j_e=$|\Omega|$=3/2 because the revival structure indicates that only ion states with $|\Omega|$=3/2 are populated via strong field ionization (see Figure 3.14 in section 3.4.2).

The electronic eigenstates of the ion are defined in terms of the projection of total electronic angular momentum on the molecular axis, $\Omega = \pm 3/2$, i.e. in the molecular reference frame. The product state of the ion expressed as $|j_e, \Omega\rangle\,|j_r, m_r\rangle$, uses two different reference frames, the molecule and lab, for the electronic and rotational angular momentum, respectively. Since the calculation of the neutral angular distribution is in the lab frame, it is convenient to express the ion angular distribution in the lab frame as well. Therefore, we convert the electronic reference frame to the lab frame. For j_e=3/2, there are four possible projections of electronic angular momentum on the lab z-axis, m=$\pm 3/2, \pm 1/2$, for both Ω=3/2 and Ω=-3/2. Since the total electronic angular momentum of the neutral is zero (in the lab and molecular frame), there is no preferred direction of the ionized, or remaining electrons', angular momentum in the lab frame prior to ionization. Therefore, we set each of the amplitudes of the four constituent states with m=$\pm 3/2, 1/2$, such that a given molecular frame state $|j_e, \pm\Omega\rangle$ to 1/2, where each state contributes 25% to the probability distribution. Note that this implicitly incorporates any lab frame alignment of the electronic angular momentum of the ion into the angle dependent ionization probability, which is our principal quantity of interest.

We express each state of well-defined electronic angular momentum in the molecular frame in terms of a superposition of product states $|j_e, m, \Omega\rangle\,|j_r, m_r\rangle$ in the lab frame. Each of the product states in this uncoupled representation can be expressed as a superposition of states of well defined total angular momentum in the coupled representation, $|j_e, j_r, J', \Omega, M'\rangle$, using a standard 3J symbol for coupling two angular momenta into a third[38]. The coupling coefficients are:

$$\langle j_e, j_r, J', \Omega, M' | j_e, m_e, \Omega, j_r, m_r\rangle = (-1)^{(\overline{\Omega} - j_r - M')}\sqrt{2J'+1}\begin{pmatrix} \overline{\Omega} & j_r & J' \\ M'-m_r & m_r & -M' \end{pmatrix} \tag{35}$$

where $|J' - \overline{\Omega}| \leq j_r \leq J' + \overline{\Omega}$ and $\overline{\Omega}$ is the absolute value of Ω. The ion rotational eigenstates are then written in terms of their symmetric and antisymmetric combinations introduced in section 1.4.3 (see equation 8-9). At each instant, ionization typically transfers amplitude from each neutral rotational level into sixteen different ion rotational states, with four different values of M' for each of the four possible values of J'.

Figure 4.3 portrays the angular distribution lost from the neutral population and simultaneously transferred to ion population. At the bottom of Figure 4.3, a two-color laser field's temporal profile is shown, separated into 4 equal time bins. As the two-color field increases in strength, the OCS molecules begin

to experience the polarizability, hyperpolarizability, and angle-dependent ionization interactions. For simplicity and illustrative purposes, Figure 4.3 excludes the effects of the polarizability and hyperpolarizability on the angular probability distributions shown above the two-color field for the ions, Figure 4.3(a), and neutrals, Figure 4.3(b). Before the field interacts with the OCS molecules, the neutral's rotational distribu-

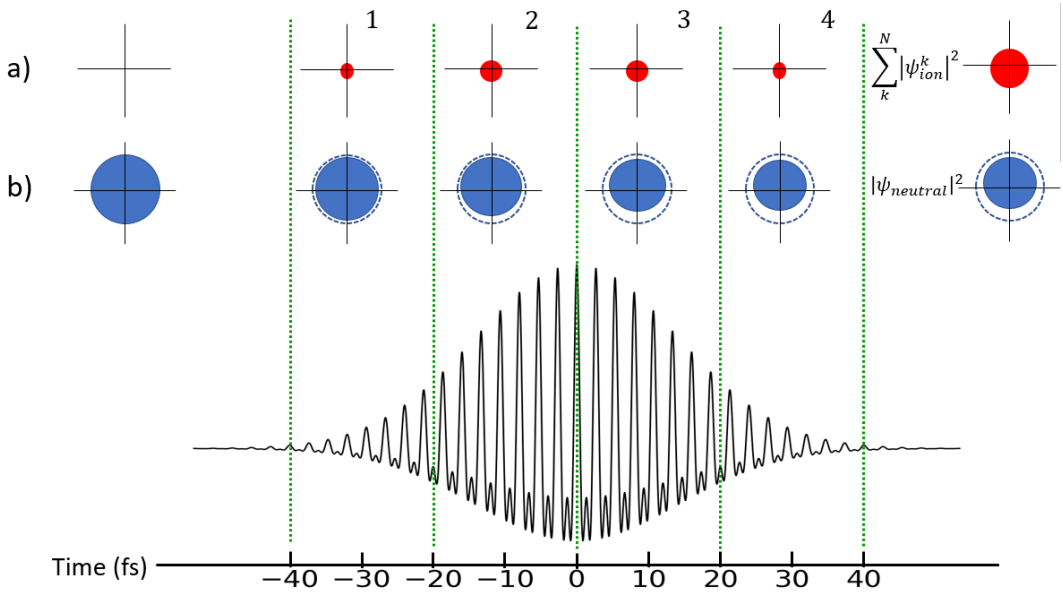

Figure 4.3: Adapted from R.R. Jones[63]. Cartoon illustrating the effect of angle-dependent ionization on the angular probability distributions of the ions (a) and neutrals (b). Prior to the two-color field interaction, the angular probability distribution of the neutrals (b) is isotropic. The calculation partitions the ionization interaction into separate time bins. The first time bin shows some degree of ionization as the rotational distribution of the neutral reduces. The loss from the neutral angular distribution appears as ion population. The neutral angular distribution evolves coherently through this process, while the total ion angular distribution is the incoherent sum of the ion angular distribution created during each time bin. Once created, probability amplitude in each bin is separately propagated according to the ion Hamiltonian.

tion ($|\psi_n(\theta,t)|^2$) is isotropic, with no initial ion population, as shown on the far left of Figure 4.3. As the field strength increases, angle-dependent ionization causes $|\psi_n(\theta,t)|^2$ to shrink anisotropically. The circular dashed lines represent the initial isotropic rotational distribution prior to the two-color interaction. The ion angular distribution depicted in a single time bin is equal to the loss of angular probability distribution from the neutral during that bin. The neutral angular probability distribution evolves coherently throughout the interaction with the two-color field, but special care must be taken to model the rotational evolution of the ions. In the experiment, the loss of neutral angular distribution is projected onto the ion angular probability

distribution at each instant in time with no coherence between ion probability created at different times. In the model calculation, we approximate the instantaneous loss of coherence by computing the ionization probability within a set of N time bins with brief, but non-zero durations. The duration of the time bins is roughly equal to three periods of the two-color field. The ion probability amplitude within each time bin is separately, and coherently propagated throughout the remainder of the laser pulse, subject to the polarizability and hyperpolarizability interactions. At the end of the pulse, the total ion angular probability distribution is determined by incoherently summing the probability distributions from all of the ion bins. The temporal binning, independent propagation of probability amplitude in different bins, and incoherent addition of the angular probability distributions from different bins at the end of the laser pulse allows us to conveniently use the TDSE rather than a density matrix approach to evolve both the neutral and ion rotational wave packets.

Since ionization can occur from both polarities of the two-color field, we solve the TDSE using separate time bins for each polarity. The ion TDSE for each polarity is shown in equation 36.

$$i\dot{\psi}_i(t) = [B_i(1 - \frac{2}{Y})(J' - \frac{1}{2})(J' + \frac{3}{2}) + V_i^{pol} + V_i^{hyp}]\psi_i(t) + (V_i^{\pm})\psi_n(t), \tag{36}$$

where J' represents half-integer units of total angular momentum of the ion, $Y = A_0/B_i$. A_0 is the spin-orbit constant and B_i is the rotational constant of the molecule. The functional forms of V^{pol} and V^{hyp} are shown in equations 30, and 31, respectively. Note that the neutrals and ions have different values for the rotational, polarizability and hyperpolarizability constants (see Table 4). Equations 37-39 give the explicit forms of the ionization interaction that couples neutral population into the ion channels for each polarity of the two-color field. The functional form arises from the application of Fermi's golden rule within each time bin with an ionization rate, $|V_i|^2$. For time bins of short duration ΔT, population lost from the neutral through ionization (Eqs 32-33) is equal to that transferred to the ion channels via the interaction terms given in equations 37-38.

$$V_i^{+} = \sqrt{a\frac{K(t)\Gamma(\theta)}{\Delta T}} \tag{37}$$

$$V_i^{-} = \sqrt{a\frac{0.045K(t)\Gamma(\pi - \theta)}{\Delta T}} \tag{38}$$

$$\Delta T = \frac{4\tau}{N} \tag{39}$$

The a-factor within the square root in equations 37, 38 is introduced to ensure that the total population of the ions and neutrals remains normalized. τ is the two-color laser pulse's temporal full width half maximum. As more time bins are introduced, we confirmed that the a-parameter approaches unity, as required. Table 4 lists the value of the a-factor and total number of time bins, N, used in the calculations.

Figure 4.4 shows a calculation using the above-mentioned method for computing the ion angular probability distribution. The red curve is the difference between the neutral angular probability distribution before and after a 5fs two-color laser pulse that induces only angle-dependent ionization. The blue curve is the ion angular probability distribution immediately following the laser pulse. With the polarizability and hyperpolarizability interactions turned off, Figure 4.4 shows good agreement between the neutral's loss and ion's gain in rotational distribution. This demonstrates the effectiveness of our model of neutral to ion population projection, temporal binning, and using Fermi's golden rule as the functional form of the ionization rate. In

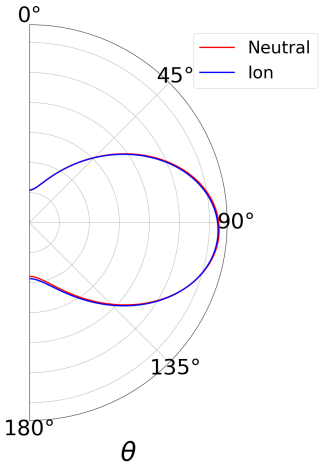

Figure 4.4: Calculated ion rotational distribution (blue curve) immediately following a 5fs two-color laser pulse that induces only angle-dependent ionization with c_1=-0.055, c_2=-0.3. Following two-color ionization, the solid red curve is the loss of rotational distribution from the neutral molecular ensemble.

the next section, we discuss the method for extracting $\Gamma(\theta)$ from the measured orientation parameter.

4.3 Extracting the Angle-Dependent Ionization Rate

The calculated orientation parameter ($\zeta_c(t)$ from equation 27) uses the molecular parameters listed in Table 4. Regarding the sign convention for this analysis, for positive applied fields, positive (hyper-) polarizability

values correspond to induced dipole directions that are parallel to the permanent dipole moment of OCS, which points from the center of the molecule to the S-atom. For example, negative hyperpolarizability components in Table 4 indicate that the induced dipole for a positive field points from the center of the molecule toward the O-atom.

To determine the angular dependence of the ionization rate, $\Gamma(\theta)$, we use Legendre polynomials as basis functions to construct its square root, $(\sqrt{\Gamma(\theta)})$, where $\sqrt{\Gamma(\theta)}$ can be expressed mathematically as,

$$\sqrt{\Gamma(\theta)} = [c_0 P_0(\cos(\theta)) + c_1 P_1(\cos(\theta)) + c_2 P_2(\cos(\theta)) + ...], \tag{40}$$

where P_l is the l^{th} order Legendre polynomial. Squaring equation 40 yields the angular dependence of the ionization rate $\Gamma(\theta)$, which we wish to determine. Using the polarizability and hyperpolarizability components in Table 4, the fitting coefficients, $c_k's$, in $\sqrt{\Gamma(\theta)}$ are varied to produce the calculated orientation parameter that best matches the experimental data. The reduced $\chi^{(2)}$ $(\chi_\nu^{(2)})$ is the figure of merit used for evaluating agreement between the calculation and measurement. To determine the minimum number of Legendre polynomials to include in the fits, we employed the statistical F-test[62] and concluded that terms up to $P_2(\cos(\theta))$ are statistically relevant. To perform the fits, the TDSE is solved for a grid of intensity (I), c_1, and c_2 values along with fixed laser and molecular parameters detailed in Table 4. We eliminated c_0 as a fitting parameter using the following normalization condition:

$$\int_0^\pi \Gamma(\theta) \sin(\theta)\, d\theta = 1 \tag{41}$$

This ensures that as the values of c_1 and c_2 are varied, the total ionization yield remains fixed. A sample

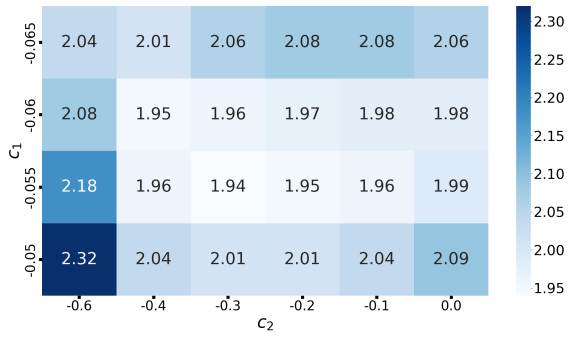

Figure 4.5: Example of a heat map portraying the reduced $\chi^{(2)}$ $(\chi_\nu^{(2)})$ as a function of c_1 and c_2

Parameter	**Value**
γ	$\sqrt{\frac{1}{3}}$
ϕ	0
B_n	$0.2028 cm^{-1}$[60]
B_i	$0.1942 cm^{-1}$
A_i	$370 cm^{-1}$[37]
$\Delta\alpha^n$	27 a.u.[61]
$\Delta\alpha^i$	25 a.u.[32]
$\beta_\perp^n$	-59 a.u.[61]
$\beta_\parallel^n$	-44 a.u.[61]
$\beta_\perp^i$	-18.2 a.u.[32]
$\beta_\parallel^i$	18.49 a.u.[32]
T_{rot}	20K
a	1.022
τ	65fs
I_s	$535 TW/cm^2$
N	30
ΔT	8.67fs
T_1	-2τ
T_N	2τ

Table 4: Values of laser and molecular parameters used in solving the time dependent Schrödinger equation to compute the angular distribution of the neutral and ion and determine ζ_c by fitting to the experimental orientation parameter. The value of B_i was chosen to best fit the experimental data. The value is within the uncertainty of the reported rotational constant for the $^2\Pi_{3/2}$ state in Table 2. T_1 is the start point of the first time bin, and T_N is the end point of the last time bin. ΔT is the duration of each time bin. There are $\frac{N}{2}$ time bins for each polarity of the two-color laser field.

grid depicted in Figure 4.5 contains a heatmap, which lists $\chi_{\nu}^{(2)}$ as a function of c_1 and c_2 for a dataset taken with a two-color intensity near OCS^+ saturation.

4.3.1 Comparing the Calculated and Measured Orientation Parameter

We measured the orientation parameter at three different intensities, which were below, near, and above $40TW/cm^2$, the measured saturation intensity of OCS^+ reported in section 3.3 of this dissertation. For each two-color intensity, the delay-dependent orientation parameter was measured for two phases, $\phi = 0$ and $\phi = \pi$. The $\phi = 0$ and $\phi = \pi$ measurements were combined (by subtraction) to produce an averaged $\phi = 0$ data run, since the strength of the two-color field maxima is the same for both phases, but the induced orientation directions are opposite. This sequence of measurements was repeated four times at each intensity. Figure 4.6 shows the average of the four data runs (blue points), for a two-color laser intensity near OCS^+ saturation, along with the calculated orientation parameter that best fits the data. The measured and calculated intensity are specified in the caption.

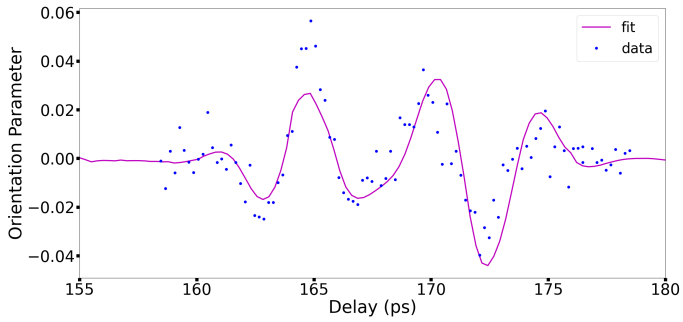

Figure 4.6: Measured vs calculated orientation parameter for c_1=-0.055, c_2=-0.30. The best fit intensity yielded $I_{calc} = 37\frac{TW}{cm^2}$, whereas the experimental intensity was measured to be $I_{exp} = 38\frac{TW}{cm^2}$.

To determine the relative importance of the various laser-molecule interactions on the orientation parameter, we performed calculations excluding ionization, hyperpolarizability, and polarizability in separate cases. Figure 4.7 shows the impact of ionization on the orientation revivals. Without ionization, the only orientation mechanism is through the field's interaction with the molecular hyperpolarizability. Clearly, with the hyperpolarizability interaction alone the agreement between the calculated and measured orientation pa-

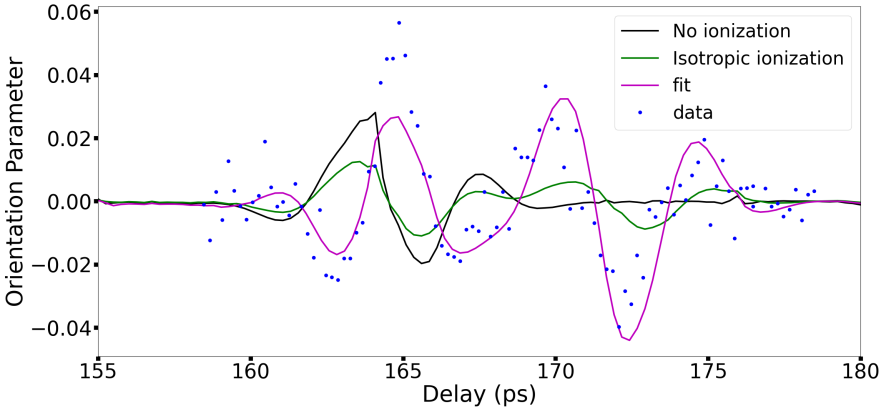

Figure 4.7: Measured vs calculated orientation parameter. The solid magenta curve is the best fit of the data ($c_1 = -0.055$, $c_1 = -0.30$). The blue dots are the measured data points, and the solid black and green curves are calculations assuming no ionization and isotropic ionization, respectively.

rameters is poor. Moreover, by removing the ionization rate anisotropy (see the green curve in Figure 4.7), we confirm its impact on the orientation revivals. We also tested the sensitivity of the orientation parameter to the hyperpolarizability interaction for both the neutral and ion. Figure 4.8 compares the original and modified orientation parameter after eliminating the hyperpolarizability interaction separately for the neutral and ion. The hyperpolarizability interaction has a minor effect on the overall shape of the calculated orientation parameter. We repeated the same tests for the polarizability interaction, as shown in Figure 4.9. Unlike the hyperpolarizability, the polarizability interactions exhibit a more noticeable effect on both the neutral and ion revivals. Elimination of the neutral polarizability anisotropy affects both the neutral and ion revivals, indicating that significant rotational redistribution occurs prior to ionization. As expected, elimination of the ion polarizability anistropy significantly impacts only the ion revival. In the next section, we will discuss the method for extracting the angle-dependent ionization rate from the measured data, and compare it with the theoretical result from the LSU group's TDDFT calculations.

4.3.2 Extracted Angular Dependence of Single Ionization

To determine the best fitting angle-dependent coefficients, $c_k's$, we produced $\chi_\nu^{(2)}$ maps for a range of c_1 and c_2 values. These maps were created for data taken at each of the three two-color intensities. Figures 4.10,

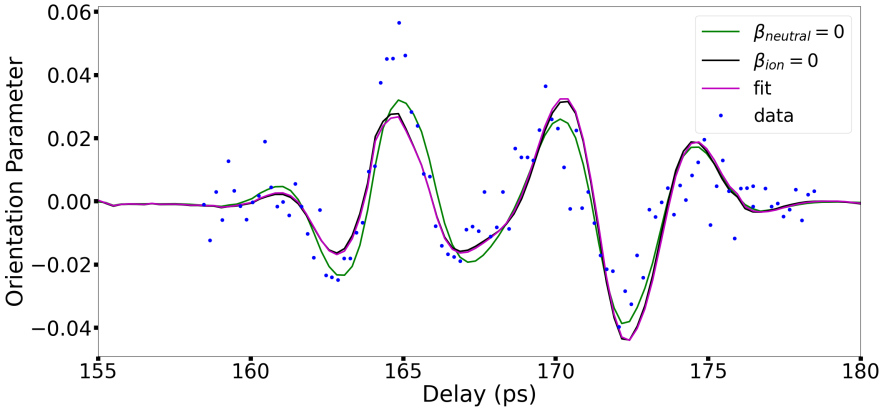

Figure 4.8: Calculated vs measured orientation parameter. The measurement is shown as blue points. The solid magenta line is the best fit to the data. The solid green (black) curve shows the result with the hyperpolarizability interaction turned off for the neutral (ion). The best fit intensity yielded $I_{calc} = 37\frac{TW}{cm^2}$, whereas the experimental intensity was measured to be $I_{exp} = 38\frac{TW}{cm^2}$.

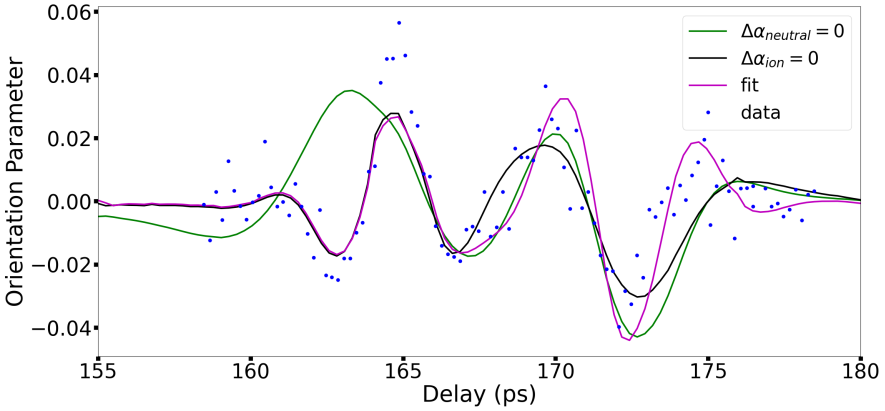

Figure 4.9: Calculated vs measured orientation parameter. The measurement is shown as blue points. The solid magenta line is the best fit to the data. The solid green (black) curve shows the result with the polarizability interaction turned off for the neutral (ion). The best fit intensity yielded $I_{calc} = 37\frac{TW}{cm^2}$, whereas the experimental intensity was measured to be $I_{exp} = 38\frac{TW}{cm^2}$.

4.11, 4.12 show the $\chi_\nu^{(2)}$ map for calculated two-color intensity below (28 TW/cm^2), near (37 TW/cm^2), and above (57 TW/cm^2) the saturation intensity of OCS^+, respectively.

Figure 4.10 shows that the $\chi_\nu^{(2)}$ minimum trend is toward the top right quadrant of the map, where $c_1 <$

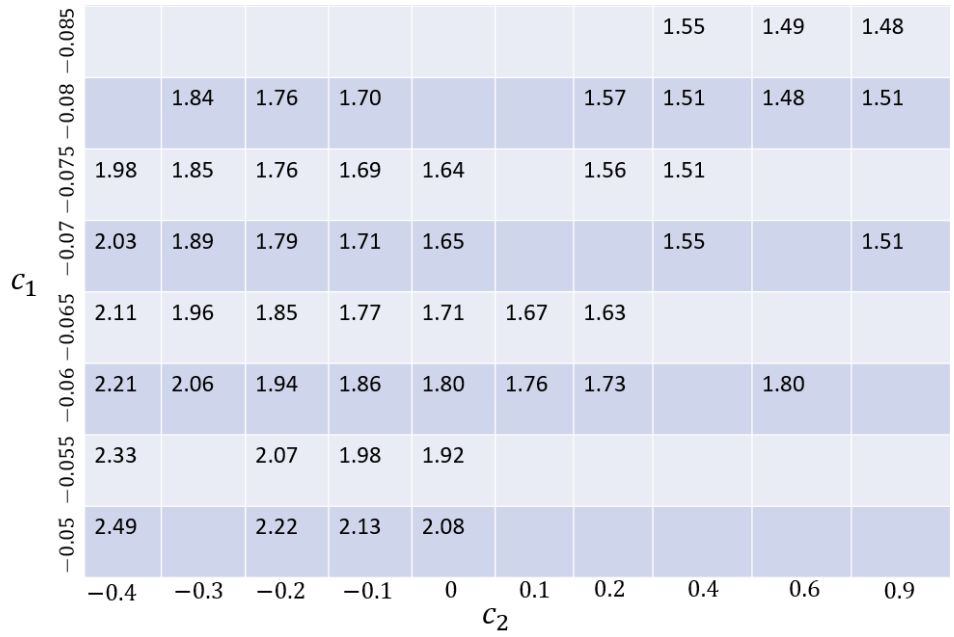

Figure 4.10: $\chi_\nu^{(2)}$ map at calculated two-color intensity of 28 TW/cm^2. I_{exp}=28TW/cm^2.

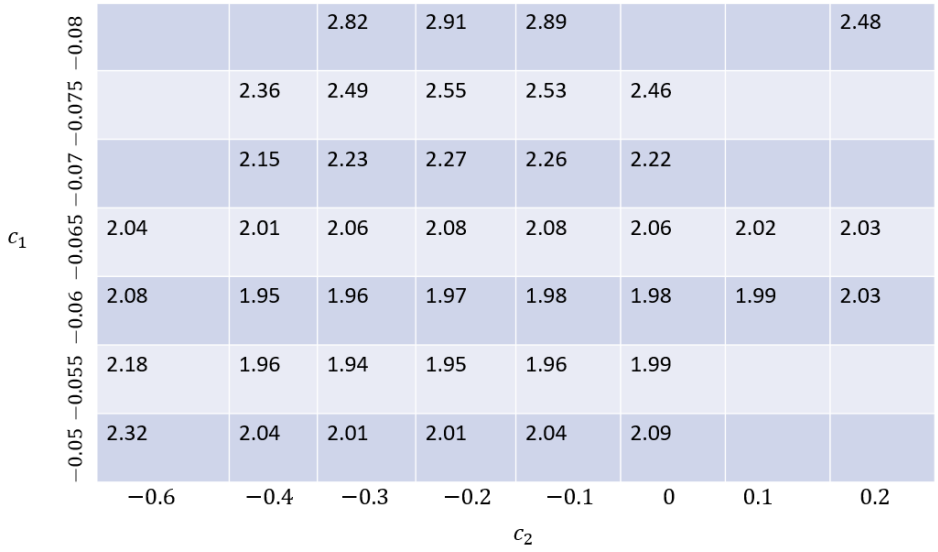

Figure 4.11: $\chi_\nu^{(2)}$ map at calculated two-color intensity of 37 TW/cm^2. I_{exp}=38TW/cm^2.

-0.07 and $c_2 > 0$. Figure 4.11 shows a broad range of local minima in the range c_1: -0.06 to -0.055, c_2: -0.1 to -0.4. Figure 4.12 shows a similar broad range of local minima, but also exhibits poorer agreement with the data given that its $\chi_\nu^{(2)}$ minimum is nearly double that of the other two data sets. These three maps indicate significant variation in the values of c_1 and c_2 that produce the best fit. Beyond evaluating the best fit c_1, c_2 values for each single intensity data set, we also determined the set of c_1, c_2 values that best fits

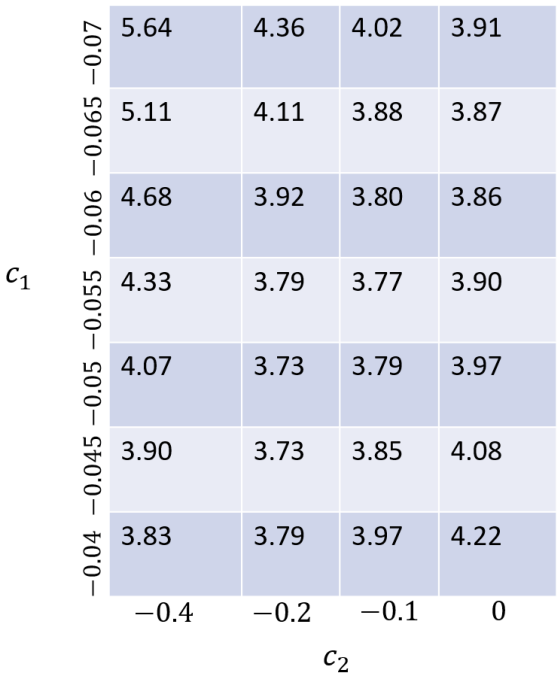

Figure 4.12: $\chi_\nu^{(2)}$ map at calculated two-color intensity of 57 TW/cm^2. I_{exp}=60TW/cm^2.

multiple intensities simultaneously. Since our model of ionization includes neutral population depletion and ion population saturation, and the measured data shows no additional revivals from other electronic states related to OCS^+, the angle-dependent ionization rate should be the same for all three intensities, at least in the absence of effects associated with the change in the laser focal volume above the saturation intensity.

To determine the $c_k's$ that simultaneously provide the best fit to the data at all three experimental intensities, we concatenate the measured delay dependent orientation parameters for each of the three two-color intensities to form a single data set. We then simulate the orientation parameter using the same values of c_1 and c_2 at the three different intensities, and create a concatenated simulated data set to compare with the experiment. The values of c_1 and c_2 are varied to determine the best simultaneous fit to all three datasets. Figure 4.13 shows an example of a fit in green with a concatenated data run as blue points.

Since the measured orientation parameter was repeated 4 times for each of the three different two-color intensities, there are 64 possible combinations of concatenating the data runs. To determine if the best fit parameters depend on which individual data runs are used to produce a particular concatenated data run, we created 16 different concatenated data set groups consisting of different combinations of the single intensity

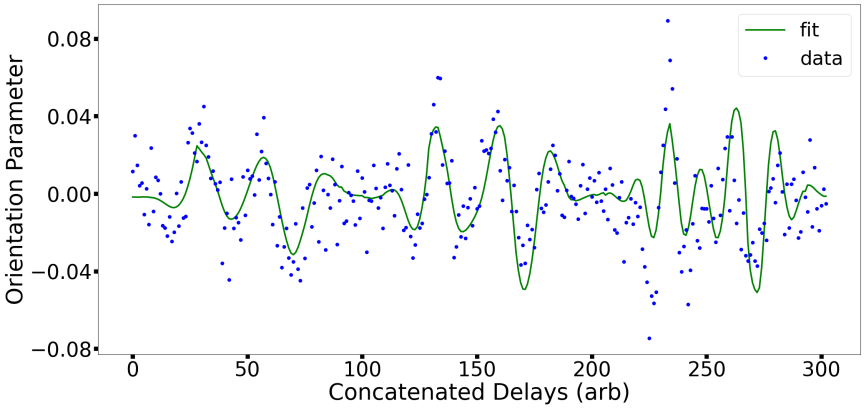

Figure 4.13: Plot comparing the calculated vs measured orientation parameter. The measured orientation parameter shown as blue data points is the concatenation of the orientation parameters for the three different two-color intensities (28,38,60 TW/cm^2). The method for concatenating the calculated curves is analogous to the measurement, where each calculated curve consists of the three best fit two-color intensities (28,37,57 TW/cm^2). The solid green line is a fit with c_1=-0.060, c_2=0.

data runs. Each concatenated data set group consisted of 4 concatenated data runs assembled from different combinations of the 4 single intensity data runs, with each of the single intensity data runs appearing only once in a concatenated data set group. Within a single group, the best fitting $c_k's$ are determined for each of the four concatenated data runs. The mean and standard deviation are collected for the group, and this process is repeated for all 16 groups. The reported best fit $c_k's$ are the average of the best fit $c_k's$ for each group, and the largest standard deviation for each c_k among all of the groups was assigned as the uncertainty. We also concatenated two data sets (I=28TW/cm^2 and I=38TW/cm^2) to compare with the $\Gamma(\theta)$ extracted using all three data sets. Any spatial volume effects should play a negligible role in the two lower intensity runs.

The resulting angular dependence, $\Gamma(\theta)$, is shown in Figure 4.14a (b) as a solid red line after concatenating 3 (2) data sets. The best fit coefficients and their uncertainties appear in the caption. The gray scale shading depicts the uncertainty in the extracted ionization rate. See section 3.4.1 for more information on the method for generating the gray scale shading. The blue curve is the calculated angle-dependent single ionization rate from the LSU group, which was introduced in section 1.2.3. Notably, the different best fit c_2 coefficient reported in 4.14 a,b and the large uncertainty in c_2 for $\Gamma(\theta)$ for both indicates that the measurements have

not determined the full angular dependence of the ionization rate with high confidence.

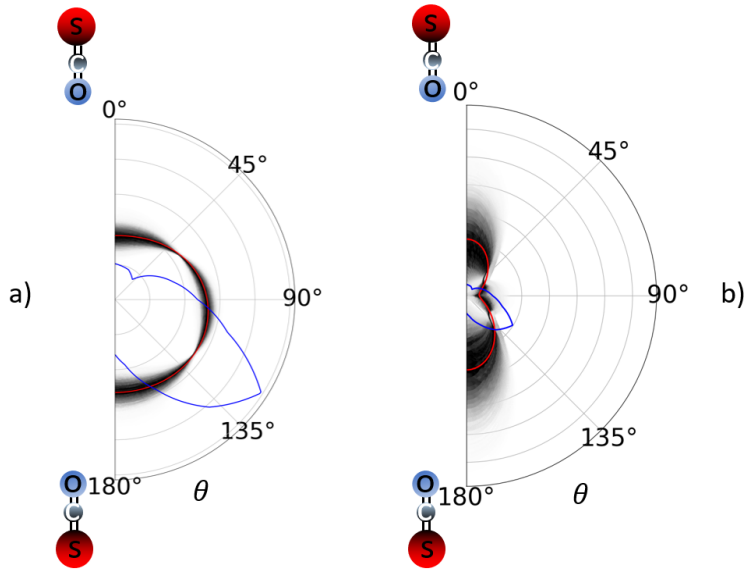

Figure 4.14: Extracted angular dependence of the ionization rate anisotropy, $[\Gamma(\theta)]$, using the result of a) all three data sets which yield c_1=-0.062±0.003, c_2=-0.04±0.04 b) only the below and near OCS^+ saturation data sets which yield c_1=-0.073±0.015, c_2=0.4±0.3. The grayscale shading represents the experimental uncertainty distribution associated with the errors of the coefficients, c_k. The blue curve is the result of TDDFT calculations performed by the LSU group for OCS in a linearly polarized 800nm field. In both cases, the field maximum is assumed to lie along $\theta = 0$.[4]

Figure 4.15 compares the orientation parameter that would have resulted from the ionization rate calculated by the LSU group (green curve) with the best fit of the data (magenta curve) for two-color intensity near OCS^+ saturation. The experimental and theoretically determined $\Gamma(\theta)$ show significant differences in the amplitudes of the orientation revivals; however, the phase of the orientation revivals are the same. Noteably, the TDDFT calculations performed by the LSU group do not include fine structure interactions. The fact that, experimentally, only one of the two spin-orbit split ground states of OCS^+ is populated via strong field ionization could impact the agreement between the predicted and actual ionization rate anisotropy.

As an additional test, we can use our extracted $\Gamma(\theta)$ to compute a symmetrized angular dependence $[\frac{\Gamma(\theta)+\Gamma(\pi-\theta)}{2}]$ to compare with the ionization anisotropy for a symmetric linearly polarized single color ionizing laser field[4]. Our extracted symmetrized rate using all three data sets shows qualitative agreement with P. Sandor's measurement[4] as shown in Figure 4.16a. Figure 4.16b compares the symmetrized rate when using only the below and at saturation data sets, which shows that OCS preferentially ionizes when the

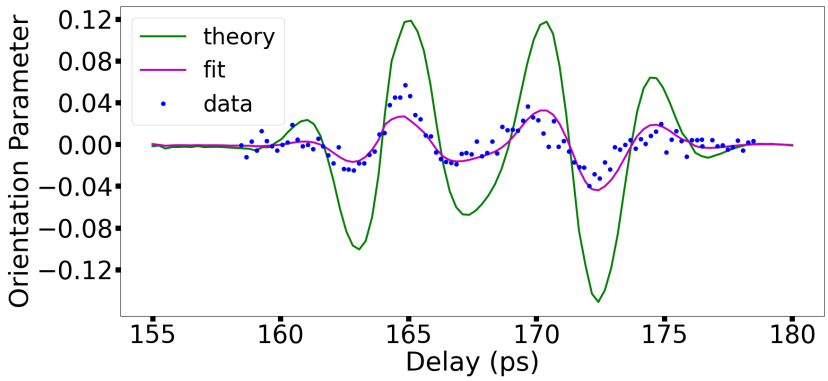

Figure 4.15: Plot comparing the orientation paramters obtained from the experiments, the calculated best fit to the measurements, and using the LSU group's calculated angle dependent ionization rate. The measured data taken with two-color intensity near OCS^+ saturation is shown as blue dots. The orientation parameters that are the result of the best fit and theoretically calculated ionization rate are shown as the magneta and green curve, respectively.

ionizing laser field is parallel to its molecular axis, which disagrees with previous measurements[4, 5] of the symmetrized rate.

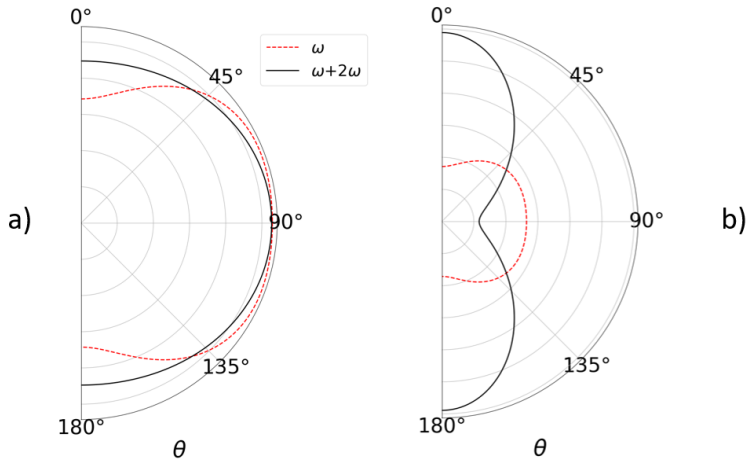

Figure 4.16: Symmetrized single ionization probability of OCS vs θ, the angle between the ionizing laser polarization and the permanent dipole moment. The dashed red curve is the measured ionization rate anisotropy for aligned molecules[4]. a) [b)] The solid black curve is the result of creating a symmetrized angular distribution from our extracted $\Gamma(\theta)$ using three [two] concatenated data sets acquiring with a two-color ionizing laser field.

Although the shape of the measured and calculated $\Gamma(\theta)$, symmetrized rates, and corresponding orientation revivals have significant differences, both the measurement and calculation performed by the LSU

group indicate that for an ionizing field directed along θ=0, OCS preferentially ionizes when the field points toward the oxygen atom. This result is opposite to that reported in [32], using circularly polarized ionizing field. It is unclear if the time-varying polarization might explain this difference.

It is worth noting that a recent paper published measured rotational constants for both fine structure of the X state of OCS^+ to be nearly identical and $\simeq 0.1947\ cm^{-1}$[64]. If these measurements are correct, then we would not be able to distinguish the two fine structure states based on the measured orientation revivals as depicted in Figure 3.14. However, we do not expect the potential population of the $^2\Pi_{1/2}$ state to alter the primary conclusions of this dissertation. The primary effect of the electronic angular momentum on the rotational structure is the establishment of both even and odd parity eigenstates for each rotational energy level and the change in the rotational revival time. Given the dominant contribution of rotational states with large angular momentum to the total rotational distribution, the rotational dynamics are not substantially influenced by the electronic degrees of freedom.

5 Summary and Future Outlook

Strong field molecular ionization continues to be an active area of study, particularly as a means for initiating and potentially probing ultrafast charge migration. Controlling molecular alignment and orientation in the laboratory and accurately simulating its effect on the electronic response to an intense laser field are crucial for understanding ultrafast electron/hole dynamics in molecules. To this end, we have used intense two-color asymmetric laser fields to induce transient orientation of OCS and the X-state of OCS^+. The observed rotational coherence of the neutral and ion wavepackets near their respective second and first full rotational revival times provided a pathway to determining the angle-dependent ionization rate using a model of angle-dependent single ionization. Using Legendre polynomials as basis functions for representing the angle dependence of the laser molecule coupling responsible for ionization, we used comparisons of simulated and measured delay-dependent orientation parameters to extract the angle-dependent ionization rate. The simulations utilize a novel approach for computing rotational coherence in the ion following ionization. Our analysis confirms that the direction of the two-color field that preferentially ionizes OCS points from the center of the molecule toward the oxygen atom, in agreement with the TDDFT calculations performed by our LSU collaborators. This is opposite to the result obtained by the Stapelfeldt group[5] based on ionization measurements using strong circularly polarized single-color laser pulses. An improved measurement signal to noise would be necessary to extract full angular dependence of the strong field ionization with high confience. Even so, the clear difference in the principal directionality of the strong field ionization rate in OCS observed for a two-color linear versus single-color circular polarization is interesting and prompts questions regarding the adiabaticity of the ionization process, and the influence of sub-cycle dynamics and the polarization of the ionizing laser field may have on strong field ionization.

Following the approach determined in this dissertation, in principle, rotational coherences can be used to extract the alignment and orientation dependence of essentially any strong field process, not just strong field single ionization. In addition, the variation in rotational constants and electronic angular momentum for different neutral and ion excited states allows one to distinguish the initial and final states for non-dissociative strong field processes, without requiring coincident detection of ions and electrons liberated by the strong field. As an example, we have preliminary results illustrating the potential of the technique for

probing angle dependent double ionization from different neutral and ionic states. Figure 5.1 shows the OCS^{+2} yield produced by an intense 800nm probe pulse, as a function of its delay after a 100 TW/cm^2 800nm aligning pump pulse. The OCS^{+2} signal is normalized to that produced in the absence of the pump. The clear variations in the normalized yield can be attributed to alignment revivals of neutral OCS and

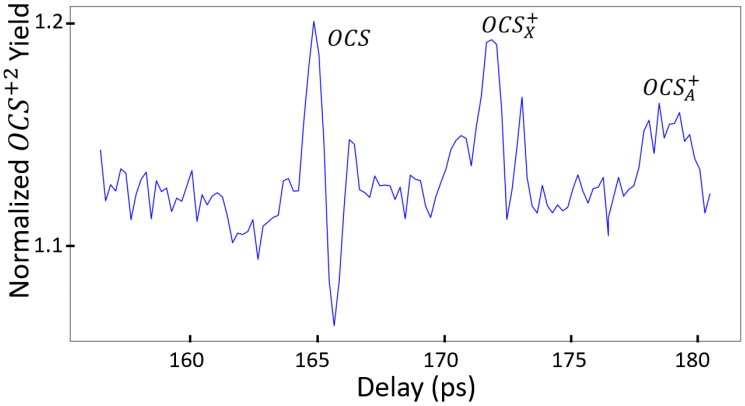

Figure 5.1: OCS^{+2} yield, normalized to the unaligned yield, versus alignment-ionization pulse delay. The intense alignment pulse, $I_{align} \approx 100\ TW/cm^2$, creates significant ionization. The alignment dependence of ionization to, and double ionization from, different neutral and ion states are reflected in the signal variations at the respective revival times.

OCS^+ ions in the X and A electronic states, which are created by the pump. The contributing neutral and ionic states are readily identified through their different rotational constants, which determine the revival times. In principle, the neutral and ion revival structures contain information on the branching ratio and ionization rate anisotropies into different ionic (and vibrational) states, as well as the angular dependences for direct double ionization from the neutral, and ionization from different initial states of OCS^+. Table 5 lists the rotational parameters for each molecular species.

As noted above, rotational coherences might be exploited to enable differential measurements of strong field processes, distinguishing contributions from neutral molecules and molecular ions in a variety of electronic and vibrational states.

Our studies exploring the use of surface second harmonic generation for probing enhanced terahertz (THz) fields from metallic surfaces (see Appendix C) used changes in optical second harmonic intensity for probing THz field enhancement. Our model for relating the optical second harmonic intensity and THz field assumed the surface polarization dynamics occur on a much faster timescale than temporal changes in the

THz field, thereby treating the THz field as "quasi-static". However, measurements of the optical surface second harmonic intensity indicate a dependence on the field polarity of the THz pulse and none for a true "quasi-static" field. Further experiments are needed to confirm the validity of our model of THz enhanced surface second harmonic generation.

Species	Rotational constant, B (cm^{-1})	Rotational Revival Times (ps)
OCS	0.2028	164.4(*)
$^2\Pi_{3/2}$ OCS^+_X	0.1946	171.3
$^2\Pi_{1/2}$ OCS^+_X	0.1983	168.1
$^2\Pi_{3/2}$ OCS^+_A	0.1869	178.4
$^2\Pi_{1/2}$ OCS^+_A	0.1907	174.8

Table 5: Rotational parameters of the OCS ground state[60] and the X-state, A-state of OCS^+[36].* indicates the second rotational revival time of OCS.

Appendix A Fast Pockels Cell Driver

Pockels cells are widely used in the lab as pulse pickers and amplitude modulators. This section will discuss assembly of a Behlke HTS 50-08-UF (Option 5ns) high voltage switch used to drive a pockels cell in quarter wave mode. The high voltage (HV) switch can tolerate a DC voltage up to $+5kV$ and outputs a high voltage pulse with an amplitude that is approximately half of the input voltage. The DC HV input was 4.7kV for this switch. These switches have a quoted rise time $< 2ns$ and a $5ns$ window.

A.1 Wiring Diagram

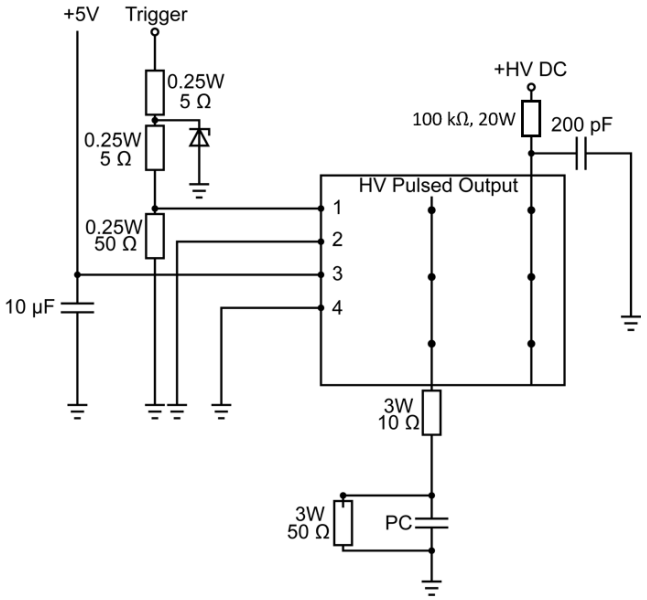

Figure A.1: Wiring Diagram for Behlke HTS 50-08 UF

The wiring diagram shown in Figure 1 details the additional electronic components required for safe and prolonged operation of the fast high voltage switch. A +5V AC-DC power adapter maintained a steady +5V with fluctuations $< \pm 0.05V$. In addition to the decoupling $10\mu F$ capacitor to ground, a Ferrite bead around the USB cable provides additional protection against high-frequency EMI (originating from the high voltage switching). The signal line is an external trigger that synchronizes the switch and the laser. This trigger signal is a TTL pulse (5V amplitude, 200ns width) from one of the 50Ω outputs of a SRS DG645 digital delay generator.

A.2 Box assembly and wiring

A photo of the exterior of the aluminum box holding the driver and pockels cell (PC) is shown in Figure 2. USB (powering the driver), MHV (+HV DC), and BNC (trigger) cables are connected to the box.

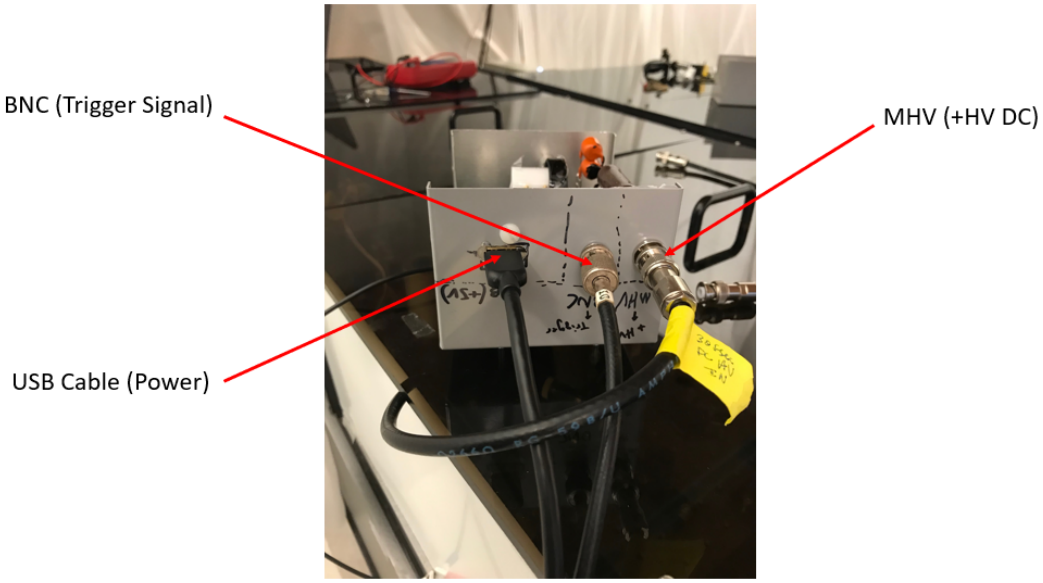

Figure A.2: Photo of the USB power, BNC (Trigger), and MHV (+HV DC) connections to the box.

The internal components of the box are shown in Figure 3. The driver rests on the base of the box with 2

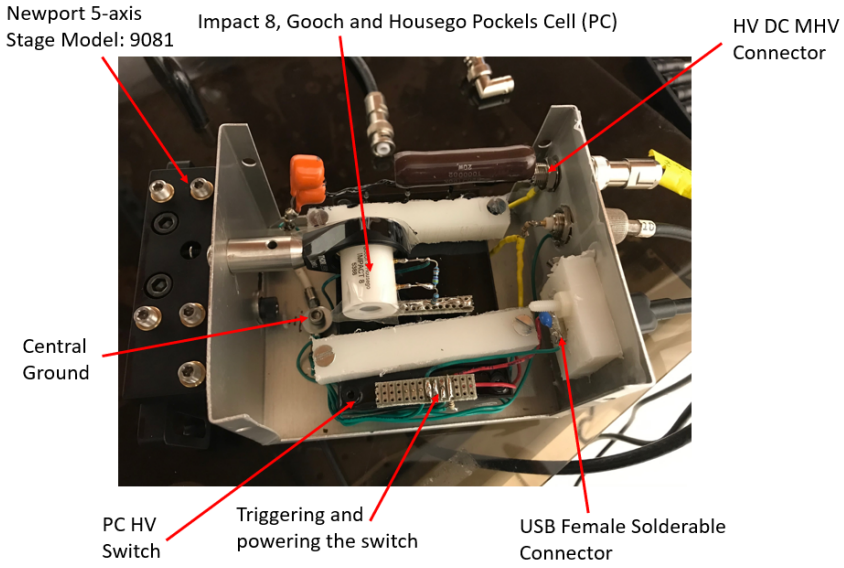

Figure A.3: Photo of the internals of the box containing the PC with labeled components.

Teflon bars, 4 8-32 screws, and nuts to secure it firmly in place. Proper shielding of the trigger is important

for ensuring the EMI does not significantly distort the trigger pulse profile. In addition, it is essential to adopt star-type grounding, which is a technique that ties every ground connection to the same point labelled "central ground" in Figure 3. This ensures that noise pick up from ground loops can be avoided. The HV and ground connections to the PC are facilitated by soldering the respective wire leads to pins, which are inserted into the cell. It is important to keep the connecting wires from the HV switch to the cell as short as possible. Longer connecting wires can result in reflections or attenuate high frequency content from the pulsed output thereby distorting or increasing the duration of the HV pulse.

To prevent a high voltage short, a few layers of Corona Dope were applied to the +HV DC connections for additional shielding. Corona Dope is a dielectric insulator with a $3.8kV/mil$ breakdown as shown in Figure 4. Corona Dope is in solution form and requires a curing time prior to applying high voltage.

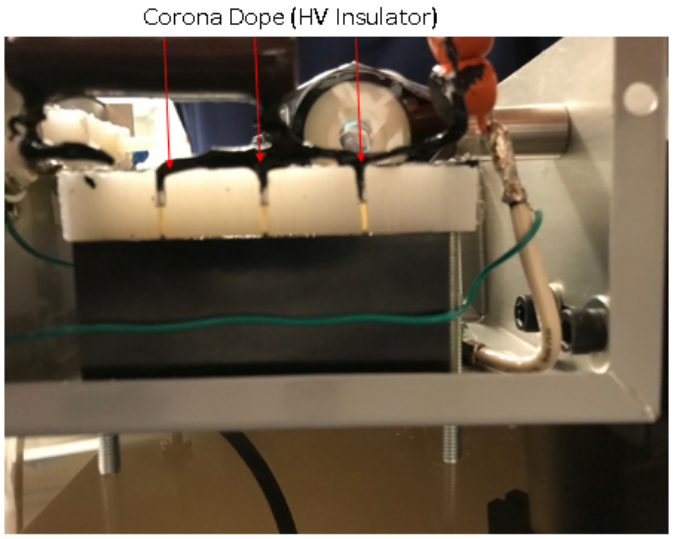

Figure A.4: Photo of corona dope for high voltage insulation

The pulsed voltage across the PC as measured using a Tektronix 75MHz high voltage probe is shown in Figure 5. Note that because the bandwidth of the high voltage probe is only 75MHz, so the measured waveform is distorted, with longer rise and fall times and significant post-pulse ringing. Qualitatively, we can see a high voltage pulse with the expected amplitude.

To directly test the performance of the PC, one can use a fast photodiode to view the double pass transmission of the mode-locked femtosecond seed laser pulse train through a pair of crossed polarizers as

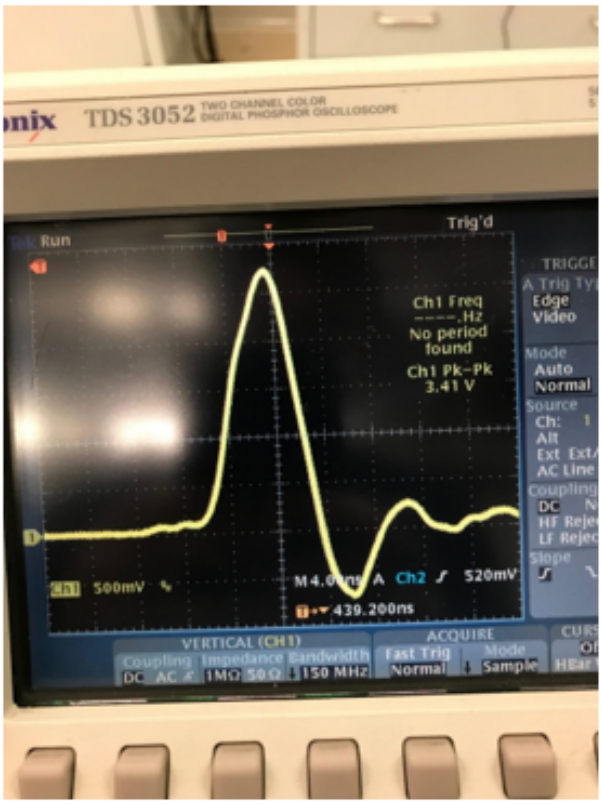

Figure A.5: HV probe measurement of the pulsed voltage across the PC. The probe attenuates the voltage 1000x.

the pulse train is delayed in sub-1ns steps.

Appendix B Transient Orientation of OCS at the Half Rotational Revival Time

In the introduction, we saw that for an equal number of initially populated even and odd rotational states, the initial orientation of an ensemble of $^1\Sigma$ molecules (such as OCS) created by a transient orienting field will revive near its rotational revival time, T. A calculation of $\langle \cos\theta \rangle$ for an OCS ensemble with a typical experimental rotational temperature (T_{rot}) and two-color intensity ($I_{\omega+2\omega}$) is shown in Figure B.1. The two-color orienting field is assumed to be non-ionizing and generates orientation via its interaction with the molecular hyperpolarizability (see Chapter 4 for more information on the functional form of the hyperpolarizability interaction). At a rotational temperature of 20K, there are nearly equal number of initially populated even and odd states. Figure 1 separately shows the calculated contributions from initially even (red dots+line) and odd (blue dashed line) rotational states to $\langle \cos\theta \rangle$. The net contribution is shown as the solid black curve, illustrating that preferential orientation is only found near the rotational revival time of OCS ($\approx$ 82ps). Interestingly, the separate contributions of the initial even and odd rotational states to the net orientation are significantly larger near the half-rotational revival time ($\approx$ 41ps) than at the full revival time. However, those contributions destructively interfere near $\frac{T}{2}$.

There are methods one can employ to suppress or reduce the perfect cancellation of the orientation revival near $T_{OCS}/2$. For example, with improved rotational cooling, one can produce ensembles with unequal distributions of even and odd populated states, with a greater fraction of the population in the ground rotational state. Figure B.2 shows the distribution of rotational states for $T_{rot} = 20K$ and $T_{rot} = 0.5K$.

With the unequal distribution of thermally populated rotational states for $T_{rot} = 0.5K$, some net orientation is predicted at the half-revival time (Figure B.3). The orientation revivals, structurally, appear quite different from those at $T_{rot} = 20K$, with more coherent oscillations for $T_{rot} = 0.5K$. This can be attributed to the fact that at lower rotational temperatures, the distribution of rotational states shifts to lower J and narrows, thus limiting the rotational velocity aberration[65], which exists for a distribution of initially populated rotational states. This can be seen visually by comparing delays from 0 to 10ps in both Figure B.1 ($T_{rot} = 20K$) and Figure B.3 ($T_{rot} = 0.5K$).

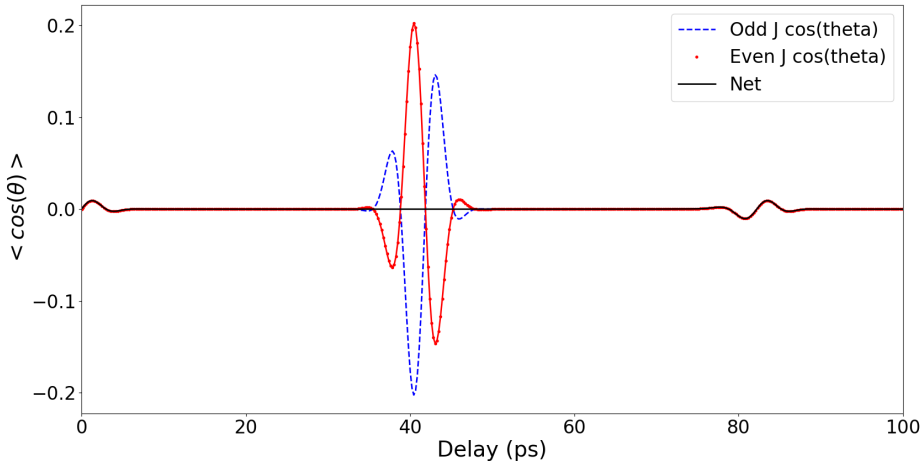

Figure B.1: Calculation of the $\langle \cos\theta \rangle$ in OCS ensemble after its interaction with a non-ionizing ω+2ω pulse for initially odd (blue hashed line), even (red dots+line), and total rotational state contributions (solid black line). All three probability distributions are separately normalized to one, so that the "total" distribution is the superposition of the even and odd distributions, each weighted by a factor of 1/2. Note that all 3 curves overlap near T_{OCS}. T_{rot} (Rotational Temperature)=20K, and $I_{\omega+2\omega}$ (Peak intensity of the two-color field)=35TW/cm^2.

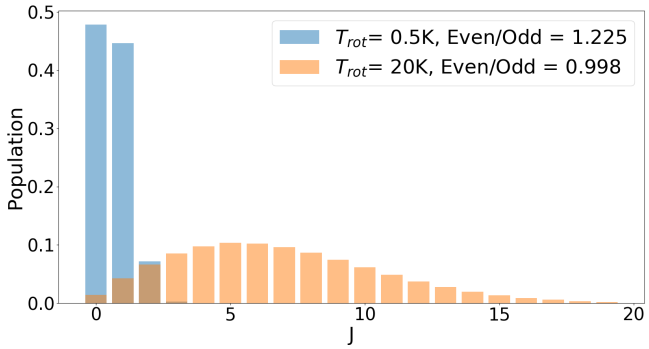

Figure B.2: Rotational state distribution at a rotational temperature of 0.5 and 20K. The ratio of even to odd initially populated rotational states is shown in the legend for the respective temperatures.

For OCS, achieving rotational temperatures <1K is required to produce an uneven distribution from which one can excite a rotational wave packet that will exhibit non-neglible orientation at the half-integer revival times. This can be a challenging endeavor and is currently not attainable with our current experimental setup. An alternative method exploits Raman rotational redistribution initiated by a control optical pulse to coherently prepare molecules in highly excited rotational states prior to two-color excitation. With an

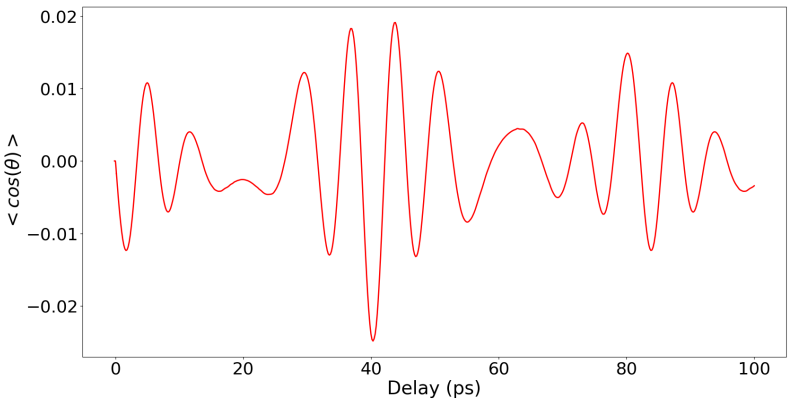

Figure B.3: Calculated $\langle \cos\theta \rangle$ for a single non-ionizing $\omega + 2\omega$ pulse at $T_{rot} = 0.5K$

appropriate time delay Δt between the single-color control and two-color pulse, the contribution from the even or odd rotational states can be suppressed. This can be seen in Figure 4 and understood from the following qualitative picture. Adopting the same angular probability distribution cartoons and $|+\rangle$,$|-\rangle$ superpositions from the introduction (see Figure 1.19), the $|+\rangle$ and $|-\rangle$ superpositions are in phase near the half-revival times, but the net even and odd contributions are out of phase. By introducing a single-color control pulse preceding the two-color pulse by a time $T_{OCS}/4$, the contributions to the coherences from the odd initial states can be almost entirely suppressed, leading to a net orientation at $T_{OCS}/2$. In that case, the maximum value of $\langle \cos\theta \rangle$ near $T_{OCS}/2$ is predicted to be up to 6 times higher than that at T_{OCS} (Figure B.4), making this method an attractive option for achieving higher degrees of orientation. Indeed, this has been experimentally realized[7, 8, 42].

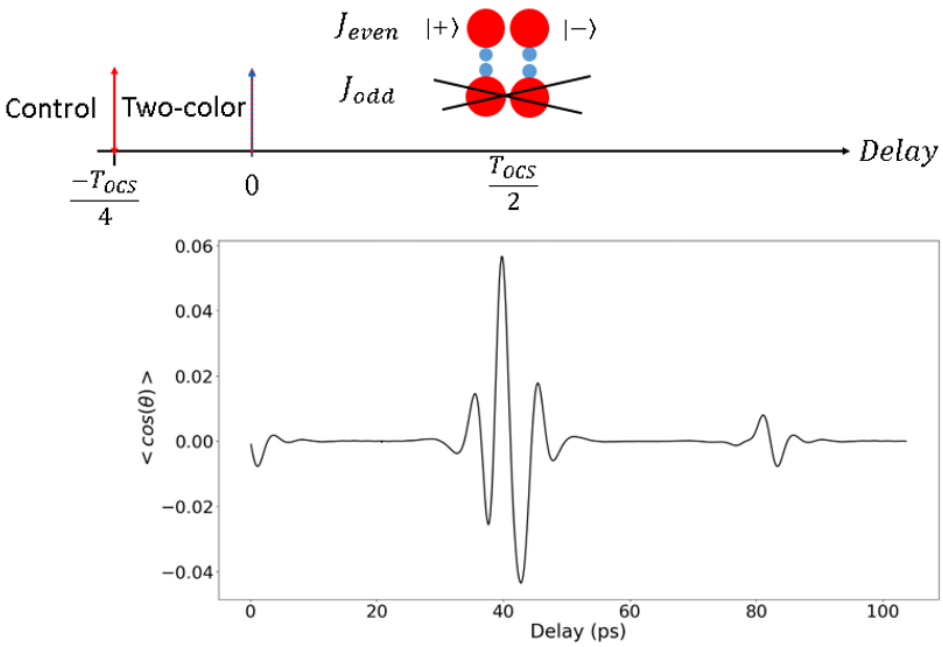

Figure B.4: Calculated $\langle \cos\theta \rangle$ for a control pulse (ω) and a two-color ($\omega + 2\omega$) pulse. Delay between the single color control and two-color pulse (Δt) = 20.7ps, rotational temperature (T_{rot}) = 20K, peak two-color intensity ($I_{\omega+2\omega}$)=35 TW/cm^2, and two-color pulse duration (τ)=65fs.

B.1 Measured OCS Orientation at $T_{OCS}/2$

To detect molecular orientation at $T_{OCS}/2$, we utilized Raman redistribution prior to two-color rotational excitation. The experimental setup in Figure B.5 is similar to that for detecting orientation at the second full revival time, except that we add an additional 20:80 BS in the pump arm prior to SHG in the BBO. The reflected beam from the 20:80 BS is used as the control pulse that precedes orientation. A mechanical delay stage is used to set the desired time delay between the control and two-color pulse, Δt. A half-wave plate rotates the linear polarization of the control pulse to be parallel to the axis of the TOF spectrometer.

Figure B.6 shows the measured orientation near the half-revival time plotted as a function of the two-color-probe delay. The red and blue curves represent two different two-color phases (ϕ) of the two-color field, which show mirror-like images of the revivals. Recall from the introduction (see Figure 1.11) that the two-color phase (ϕ) determines the direction and magnitude of the field maxima. A third black dashed curve shows the case where the control pulse is blocked. As predicted by the calculations, the orientation at the

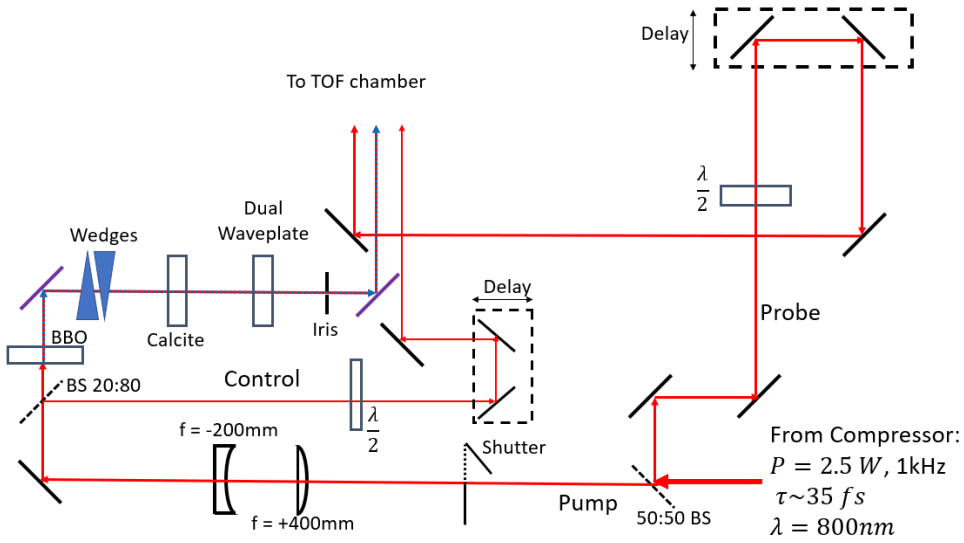

Figure B.5: Setup for probing two-color orientation at $T_{OCS}/2$. A 20R:80T beam-splitter is inserted into the pump arm prior to two-color generation. The control beam line also has a delay stage for controlling the relative Δt between the control and two-color pulse. The values on the bottom right corner of the figure specify the input pulse energy (ϵ), the pulse duration (τ), and the central wavelength (λ) at the output of the compressor.

half-revival time is negligible without the control pulse. However, the maxima in the orientation parameter are not as large as predicted, within a factor of two, or so, of that observed at the integer revivals (see Chapter 4).

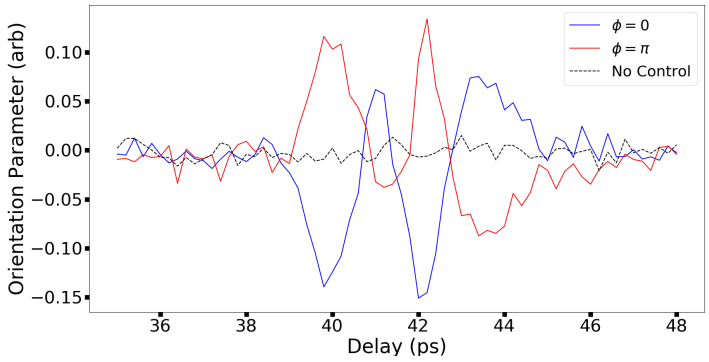

Figure B.6: Measured orientation near $T_{OCS}/2$ with the two-color orienting pulse preceded by a single-color control pulse with a delay, Δt = -20.7ps. The delay axis is the relative time delay between the two-color and probe pulses. The blue and red curves show orientation for two-color phase (ϕ) = 0, π, respectively. The black (dashed) curve shows the orientation parameter with the control pulse blocked.

Appendix C THz Enhanced Surface Second Harmonic Generation from Metallic Surfaces

C.1 Motivation

Single-cycle carrier-envelope phase-locked terahertz (THz) pulses are useful tools for studying strong field molecular physics. For example, they have been employed in the lab to induce field-free orientation in gas phase molecules[7, 10]. There is also interest in using intense single-cycle THz fields into strong-field physics experiments to explore the effect of quasi-static fields on strong-field interactions such as high harmonic generation. The principal limitation to using THz pulses in strong-field experiments is the available field strength. Thus, methods for enhancing, and quantifying the enhancement, of THz fields would be extremely valuable for exploring THz field driven molecular interactions. For more background and introduction on THz radiation and its uses in strong field atomic and molecular physics, refer to former PhD student, Sha Li's dissertation[12].

Local field enhancements in the vicinity of metal nano-tips provide one route toward generating extremely strong THz fields[12]. In the THz regime, the field enhancement mechanism can typically be attributed to the geometric lightning rod effect. The strong THz field induces a transient surface charge density near the sharpest feature of the nanotip. This aggregated charge is responsible for the enhanced field in the vicinity of the tip. The enhancement is localized roughly to within one tip radius away from the tip surface[66], producing a local THz field, F_{loc}^{THz},

$$F_{loc}^{THz} = \gamma F_0^{THz}, \tag{42}$$

where γ is the THz field enhancement factor, and F_0^{THz} is the incident THz field strength. The THz field enhancement factor, γ, for tungsten nanotips has been measured to be [67],

$$\gamma = 0.06\frac{\lambda}{R}, \tag{43}$$

where λ is the central wavelength of the THz pulse and R is the tip radius. Former lab member, Sha Li, measured γ as high as a 3000[67] for R$\approx$20nm and λ=2mm. The resulting fields could be useful for influencing dynamics initiated by strong optical fields in the vicinity of the tip. Unfortunately, the volume

spanned by the enhanced field is a small fraction of the extent of a typical visible or near infrared laser focal volume (Figure C.1). An alternative geometry might allow one to achieve some degree of field enhancement while covering a larger portion of the laser focal volume.

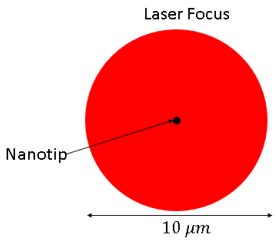

Figure C.1: A cartoon comparing the nanotip size against a typical laser focal spot size.

C.2 Razor blade for Enhancing THz fields

To this end, a razor blade with an edge radius (R) of ≈ 1 μm was investigated as an alternative geometry to produce THz field enhancement over a larger fraction of the laser focal volume. The field enhancement factor, γ_r for a razor scales as [68],

$$\gamma_r \propto \sqrt{\frac{\lambda}{R}} \tag{44}$$

Figure C.2 compares an estimated field enhancement using equation 44 against the measured field enhancement from a nanotip with a 20nm tip radius. We have been able to produce THz pulses at a 1kHz repetition rate and with field strengths of $\approx$ 50 kV/cm, via tilted pulse front optical rectification[69] of 1mJ, 800nm laser pulses. Accordingly, with an enhancement of a factor of 8, we could produce 400kV/cm THz fields. This would be a big step toward achieving the field strengths needed to influence nonlinear optical phenomena based on electron rescattering in gas phase molecules. Therefore, we explored the use of an all optical method for characterizing the THz field enhancement, as discussed in the next section.

C.3 Surface SHG for probing THz Field Enhancement

When a solid material is exposed to an intense laser field, the absence of inversion symmetry at the surface can result in the formation of a non-linear surface polarization and surface second harmonic emission[70].

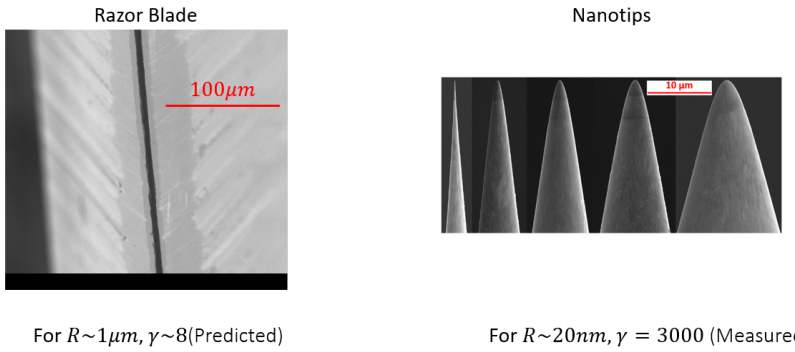

Figure C.2: Scanning electron microscope images of a razor blade and nanotips[12]. Below each image, the THz field enhancement is specified for a given edge or tip[67]. Note that the razor estimates the field enhancement using equation 3, and the nanotip's enhancement was measured by Sha Li[67].

Figure C.3 depicts a strong laser pulse grazing off a surface with an angle of incidence specified by φ.

Figure C.3: Cartoon of SHG generated from a strong 800nm (red) laser pulse grazing off a surface. Beyond non-linear optical processes on the surface itself, for air molecules residing on the surface, the air to surface interface breaks the local inversion symmetry, thereby permitting even-order nonlinear optical processes just above the surface. The arrows indicate the direction of propagation of the fundamental red and newly formed second harmonic blue.

The polarization ($\mathbf{P}$) in a material, induced by an intense laser pulse, can be represented as a Taylor series expansion of the laser field, $\mathbf{E}_\omega$, as

$$\mathbf{P} = \epsilon_0(\chi^{(1)}\mathbf{E}_\omega + \underline{\chi^{(2)}_{eff}\mathbf{E}^2_\omega} + ...), \tag{45}$$

where χ^n_{eff} are elements of the electric susceptibility of order n, and $\mathbf{E}_\omega$ is the electric field strength of the 800nm pulse. The underlined term in equation 45 is responsible for SHG. The energy level diagram for SHG is depicted in Figure C.4. The polarization term responsible for SHG can be understood as the 800nm pulse inducing 2 virtual excitations, where the virtual transition levels are represented by the dashed lines

in Figure C.4. $\chi^{(2)}_{eff}$ in Equation 45 is decomposed into bulk and surface contributions[71] such that,

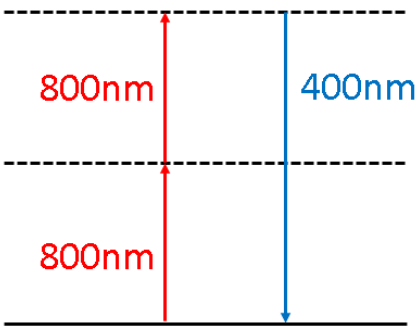

Figure C.4: Cartoon of an energy level scheme for optical second harmonic generation (SHG), where the dashed lines are virtual states.

$$\chi^{(2)}_{eff} = \chi^{(2)}_{bulk} + 3\chi^{(3)}E_{surf}, \tag{46}$$

where $\chi^{(2)}_{bulk}$ is the bulk contribution to the 2nd order susceptibility and $3\chi^{(3)}E_{surf}$ represents the surface contribution. E_{surf} is an intrinsic surface electric field[71]. For surface SHG from a metal, the surface SHG contribution dominates over that from the bulk, so $\chi^{(2)}_{eff} \approx 3\chi^{(3)}E_{surf}$. After including a THz pulse, $\mathbf{E}_{THz}$, along with the 800nm laser pulse, the induced polarization, $\mathbf{P}$ now becomes,

$$\mathbf{P} = \epsilon_0(\chi^{(1)}\mathbf{E}_{800nm} + \underline{\chi^{(3)}(\mathbf{E}_{surf} + \mathbf{E}_{THz})\mathbf{E}^2_{800nm}} + ...) \tag{47}$$

The intensity I_{400nm} of the surface SHG is proportional to the square of the underlined terms, where the intensity, I_{400nm} is the following,

$$I_{400nm} \propto {\chi^{(3)}}^2(\mathbf{E}_{surf} + \mathbf{E}_{THz})^2 I^2_{800nm} \tag{48}$$

where I_{800nm} is the intensity of the fundamental laser pulse. Local field enhancement of E_{THz} near nano- or micro-structure surface can be characterized by examining changes in I_{400nm}. Figure C.5 illustrates the energy level diagram describing THz enhanced surface second harmonic generation. Similar to Figure C.4, the red pulse induces virtual transitions. The THz photons with frequency Ω can further promote transitions to either a higher (lower) lying virtual state, where the central wavelength of second harmonic emission can

be smaller (larger) than 400nm. However, for typical experimental parameters, the 2Ω energy separation between the higher lying virtual states is well within the bandwidth of the 400nm laser pulse.

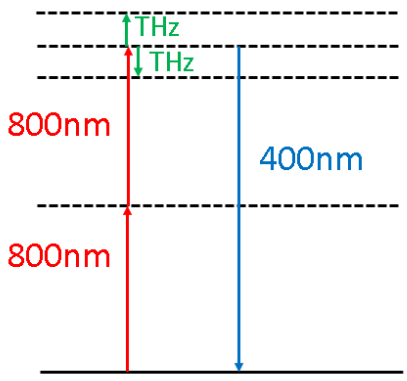

Figure C.5: Cartoon of an energy level scheme for THz field induced second harmonic generation.

C.4 THz Enhanced Surface SHG

Experimental Setup

In principle, by detecting changes in the intensity of the surface second harmonic emission in the presence of a strong THz field, the THz field enhancement can be quantified. To test this approach, we utilized the output of a Spectra-Physics Spitfire femtosecond laser system to generate single-cycle THz pulses and to provide the fundamental laser pulse for creating surface SHG. The beam path inside the Spitfire laser system can be found in Dan Pinkham's dissertation (see Figure 2.3a, p.20)[41]. Figure C.6 illustrates the experimental setup for measuring THz enhanced surface SHG. The Spitfire produced 800nm (red) laser pulses with duration, $\tau \approx 100fs$ and compressed output power of $P \approx 1.5 - 1.7W$ at a 1kHz repetition rate. A 30R:70T beamsplitter is used to create two beams, where the transmitted beam is used to make THz pulses via titled pulse front optical rectification in $LiNbO_3$[69] and the other serves as the intense fundamental probe pulse. The relative red-THz time delay can be varied with a pair of mirrors (M4,M5) attached to a motorized delay stage. After the THz pulses are produced using the titled pulse front scheme[69], a pair of off-axis parabolic mirrors collimate and focus the THz pulse onto the surface of interest. A hole in the second off-axis parabolic mirror (PM2) allows the red beam to pass through and graze off the sample co-linearly with the THz pulse. The grazing angle of incidence, φ, was $\approx 2°$. A 400nm mirror (M8) reflects the generated

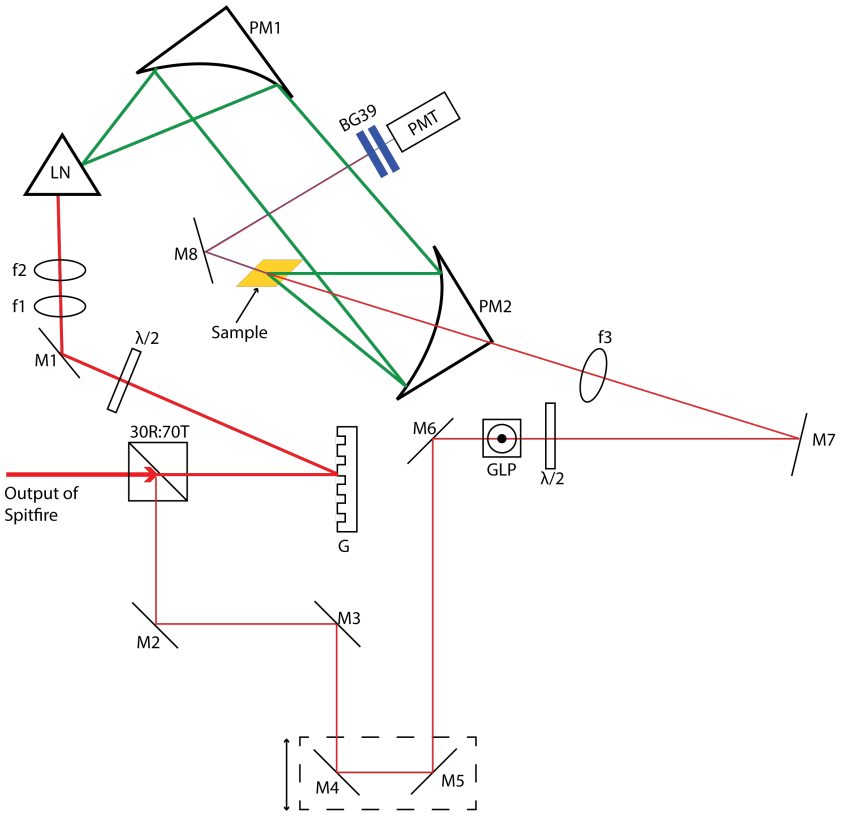

Figure C.6: THz enhanced surface SHG experimental setup. The Spitfire produced pulses with duration, $\tau \approx 100fs$ and compressed output power of $P \approx 1.5 - 1.7W$ at 1kHz repetition rate. The output is split by a 30R:70T beamsplitter. The higher energy beam path is used to generate THz radiation using the titled pulse front excitation scheme[69]. The other beam path is used as the pump to induce surface SHG. M1-7: 800nm mirrors, M8: 400nm mirror, PM1: 90° Off-axis Parabolic Mirror, RFL = 101.6mm, PM2: 90° Off-axis Parabolic Mirror, RFL = 50.8mm, G: Grating, f1: +500mm, f2: +300mm, f3:+200mm, $\lambda/2$: half-wave plate, GLP: Glan Laser polarizer, BG39: Blue-Green filters, PMT: Photomultiplier Tube

400nm light toward a detector. Since surface SHG is a weak nonlinear process (efficiency $\approx 10^{-14}$[72]), a photomultiplier tube is required for detection. BG39 filters are inserted to absorb the fundamental 800nm and transmit the 400nm light.

Given the mixed elemental composition of razor blades and uneven structure at the sub-micron level as shown in Figure C.7, we first characterized the THz field response for an optically flat surface to aid in distinguishing material versus surface effects on the SHG yield. A gold mirror was used for these measurements, due to its optically flat surface with a well defined material composition.

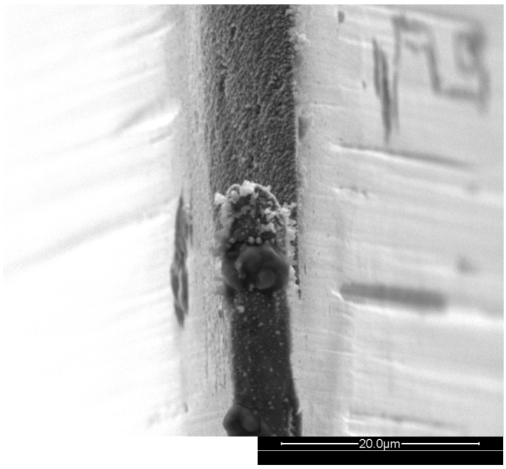

Figure C.7: Image of the shape edge of a razor blade acquired using a scanning electron microscope.

C.4.1 Gold mirror

An optically flat bare (no protective coating) gold mirror is a surface with known material composition without micron-level features. To characterize the surface response upon applying a THz field, the intensity of the 400nm light, I_{400nm}, on the gold mirror was measured as a function of the relative red-THz time delay. The THz (ε_{THz}) and red (ε_{800nm}) were set to have their polarizations mutually parallel and nearly parallel to the surface normal ($\hat{n}$) as shown in Figure C.8. Figure C.9 shows delay-dependent measurements of second harmonic yield from the surface of the gold mirror with the beam's propagation and polarization configuration depicted in Figure C.8. At relative delays beyond ±5ps, the red and THz pulses are not temporally overlapped; however, the yield is non-zero due to surface SHG generated solely by the interaction between the surface field and fundamental red pulse. The delay-dependent changes in the SHG yield indicate that, according to equation 48, the THz electric field polarity is either parallel or anti-parallel to the intrinsic surface field E_{surf}.

While keeping the relative THz-red time delay fixed at the peak of the second harmonic yield, we measured the dependence of the yield as a function of θ, the angle between the polarization of the red, $\hat{\varepsilon_{800nm}}$, and the surface normal $\hat{n}$. Figure C.10 shows a plot of this dependence with and without the THz field while keeping the THz polarization direction $\hat{\varepsilon_{THz}}$ fixed parallel to the surface normal. The yield is maximized when the THz and red pulses are polarized mutually parallel and parallel to the surface normal and can be enhanced

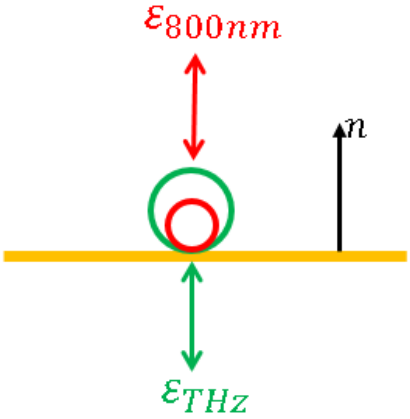

Figure C.8: Cartoon of the red and THz beam grazing geometry for an optically flat gold mirror. For ease of visualization, the THz and 800nm beams are vertically offset. Their centers are nominally overlapped when focused onto the surface. The green/red circles indicate the out of the page direction of propagation for the THz and red pulse, respectively. The black arrow indicates the surface normal, $\hat{n}$. The red and green double ended arrows indicate the polarization of the red and THz beam, respectively.

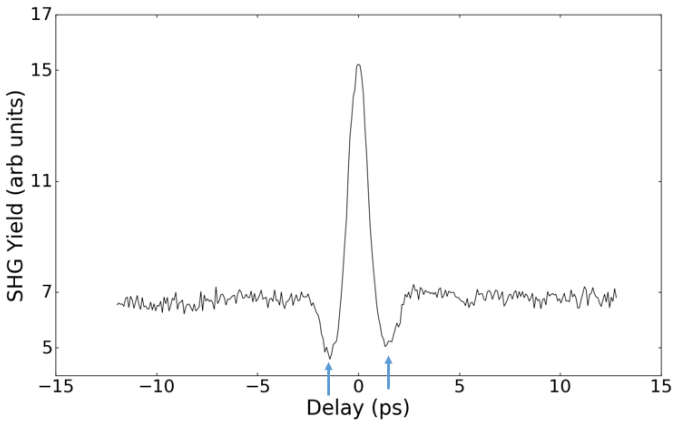

Figure C.9: THz enhanced second harmonic emission off the surface of a gold mirror. The delays beyond $\pm 5ps$ show a constant SHG yield, which is SHG generated from only the interaction between the surface field and red pulse. The blue arrows show the yield decreasing below the baseline at those two delays. According to equation 48, these dips in the surface SHG yield arise from the THz field polarity and direction of the intrinsic surface field being anti-parallel.

by as much as a factor of 3 in the presence of the THz field. To quantify the degree of THz induced SHG enhancement, we defined an SHG enhancement parameter (β) as,

$$\beta = \frac{I_{400nm}(THz)}{I_{400nm}(NoTHz)}, \tag{49}$$

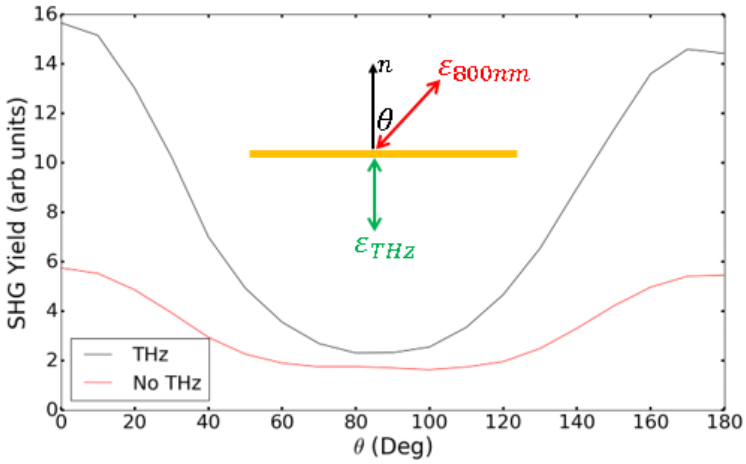

Figure C.10: Surface second harmonic yield measured off a gold mirror as a function of the angle between the surface normal ($\hat{n}$) and the polarization of the red ($\varepsilon_{800\hat{nm}}$) pulse. The polarization of the THz pulse ($\varepsilon_{\hat{THz}}$)is fixed parallel to $\hat{n}$.

where $I_{400nm}(THz)$ and $I_{400nm}(NoTHz)$ are the intensity of 400nm pulse with and without the THz interaction, respectively. The SHG enhancement is plotted as a function of θ in Figure C.11.

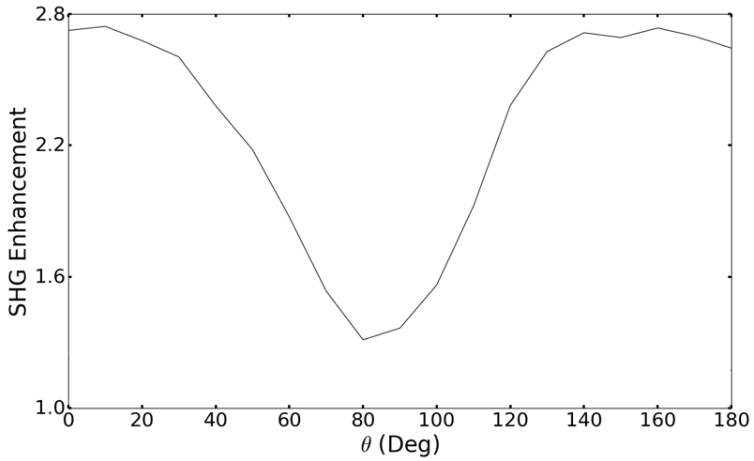

Figure C.11: SHG enhancement as a function of θ, the angle between the red polarization direction ($\varepsilon_{800\hat{nm}}$) and the surface normal, $\hat{n}$.

C.4.2 Fine pitched screw

After quantifying the SHG enhancement from an optically flat surface, we wanted to determine if the enhanced THz field near micro-structured surface features could lead to enhanced SHG efficiency. To that

end, we attempted to observe surface SHG from the edge of a razor blade. Unfortunately, insufficient SHG was observed to draw any quantitative conclusions. Therefore, we sought to increase the surface SHG generated by reflecting the red and THz beams from periodic arrays of micron and sub-micron structures. First we looked for SHG enhancement from a fine pitched stainless steel screw with sub-millimeter thread width and spacing. Figure C.12 shows a scanning electron microscope image of the surface of a typical screw used for these experiments. The measured delay-dependent THz enhanced surface second harmonic

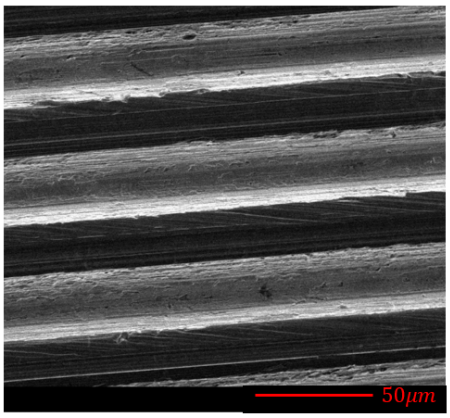

Figure C.12: Image of a fine pitched screw used for quantifying THz enhanced surface SHG enhancement.

yields from a fine pitch screw are depicted in Figure C.13, where the laser and THz pulses propagate parallel to the long axis of the screw, i.e. perpendicular to the screw threads. To isolate the effect of the thread structures from other surface effects, we repeated the delay scans using the same rod geometry and material but without threads (denoted as "Smooth" in the plot legend). The different runs correspond to nominally identical measurements with three threaded and "smooth" screws. Interestingly, the nominally "smooth" (which do exhibit nano-scale roughness) screws produced a larger second harmonic yield as compared with the threaded screws.

To determine the SHG enhancement for each type of screw, the SHG yield was divided by the average baseline yield from -8 to -5 ps. Figure C.14 shows the SHG enhancement as a function of the red-THz delay. For two of the three cases, the threaded and smooth screw show roughly equivalent SHG enhancements that are comparable to several times larger than that for the optically flat gold surface. However, *Smooth* 3's SHG enhancement of 50 is at least 5x larger than that of the other screws, and is $\approx$ 15x larger than that of the gold mirror. According to Figure C.13, the signal size of the SHG yield from *Smooth* 3 and *Smooth* 2

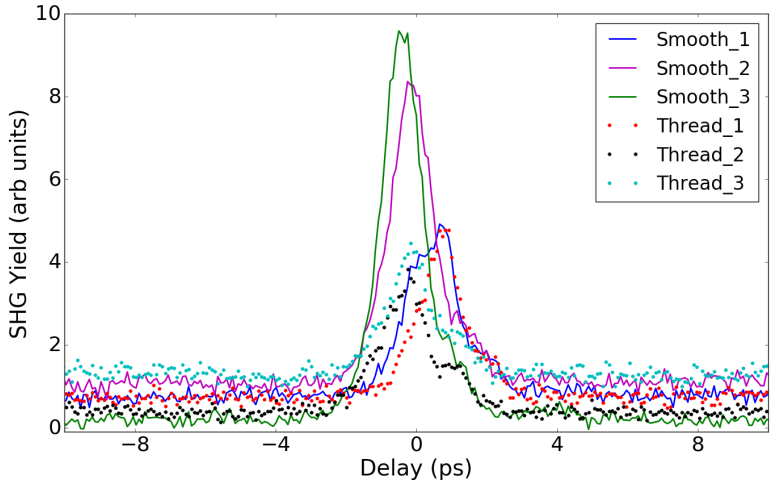

Figure C.13: Measured surface SHG yield as a function of red-THz delay. The legends with "Thread" and "Smooth" correspond to screws with and without the threads, respectively. Six different screws (three of each type) were used when conducting these experiments. The time shift between the peaks is due to slight differences in the spatial overlap position of the red and THz beams after manually switching between the different screws.

with the THz field present are within 15-20% of each other near a delay of 0ps. However, Figure C.13 also shows that the SHG baseline near $\pm$ 8ps is $\approx$ 5x lower for Smooth 3 as compared to that for *Smooth* 2. So, apparently, the reduced baseline for *Smooth* 3 is primarily responsible for the large SHG enhancement. Based on the data presented in Figures C.13-C.14, the threaded rods produce a THz field enhancement

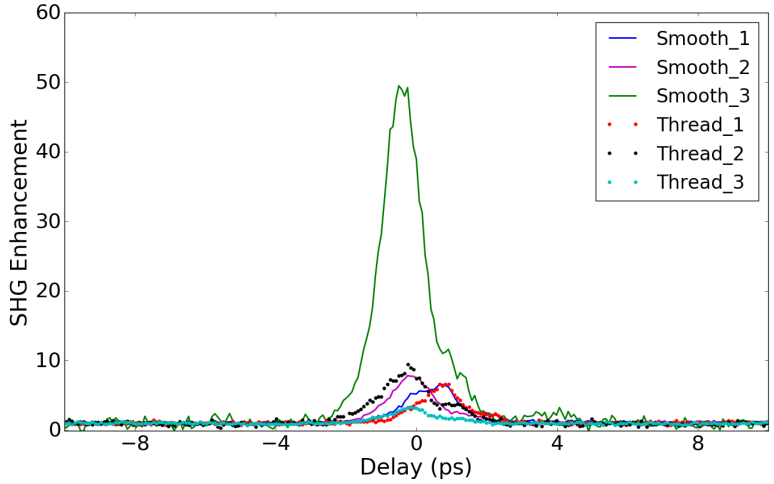

Figure C.14: SHG enhancement as a function of red-THz delay. The primary source of the large SHG enhancement for *Smooth* 3 is the reduced surface SHG induced by the red pulse alone.

that is less than, or comparable, to, that of a nanoscopically rough surface of the same material. Moreover, the primary source of the largest SHG enhancement observed for one of the "smooth" screws, is due to suppression of surface SHG in the absence of the THz. The fact that the signal is signicantly enhanced in the presence of the THz pulse does suggest significant field enhancement near micro- and nano-scopic surface features. Next, we describe measurements exploring whether the THz field contributes more to SHG enhancement after reducing the periodic surface features to the sub-micron level.

C.4.3 Gold reflective grating

Gold reflective gratings have a macroscopically smooth surface with periodic sub-micron surface features. To test the effect of surface grooves with separation $\approx$ 800nm on surface second harmonic emission, the second harmonic yield was measured for the beams propagating parallel ($\parallel$) and perpendicular ($\perp$) to the grating grooves. Figure C.15 illustrates the two different orientations of the grating relative to the propagation of the red and THz beams. Delay scans comparing the SHG yield for both the parallel (blue) and perpendicular

Figure C.15: Cartoon comparing the propagation directions of the red and THz pulses (colored green) grazing off the surface of gold reflective gratings with a) THz-red propagating (left to right) perpendicular ($\perp$) to the grooves and b) THz-red propagating (into the page) parallel ($\parallel$) to the grooves.

(red) orientations are shown in Figure C.16. The perpendicular grating orientation has a noticeable baseline, similar to that of the gold mirror. However, the dips in the SHG yield during the negative half-cycles of the THz field, which are observed for the gold mirror, are absent with both orientations of the grating. The parallel configuration has a noticeable decrease in surface SHG yield at larger delays, similar to that seen for the fine pitch screw, *Smooth* 3. The θ dependence of the SHG yield is plotted in Figure C.17 for the parallel configuration. Without the THz field, the second harmonic yield in the parallel orientation exhibits virtually

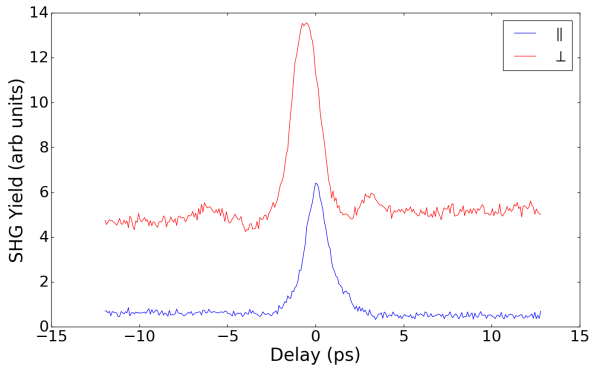

Figure C.16: Measured surface second harmonic emission as a function of the red-THz delay for both the parallel (blue) and perpendicular (red) grating orientations. The time shift between the peaks is due to slight differences in the spatial overlap position of the red and THz beams after manually switching between the two different grating orientations.

no dependence on θ. With the THz pulse present, the second harmonic emission peaks when both pulses are mutually parallel and also parallel to the surface normal as we saw with the mirror. When reorienting

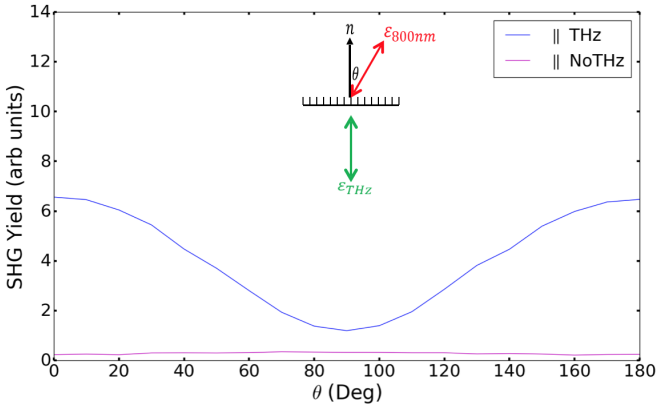

Figure C.17: Measured second harmonic emission versus θ, the angle between the red polarization direction and the surface normal, n for the ∥ grating configuration.

the grating so that the grooves are perpendicular to the direction of the propagation, the θ dependence of the SHG yield with and without the THz field appears as shown in Figure C.18. The perpendicular configuration results in a pronounced θ dependence in second harmonic emission, and an enhancement in SHG yield with the THz field present. The SHG enhancement for both grating orientations is plotted in Figure C.19. The substantial SHG enhancement in the parallel configuration is nearly an order of magnitude

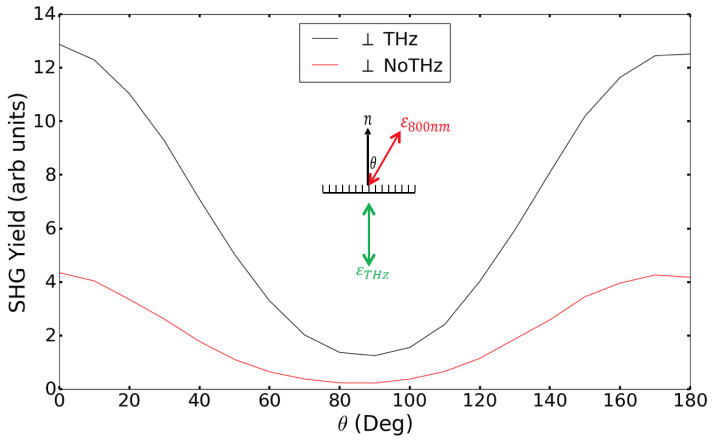

Figure C.18: Measured SHG yield versus θ, the angle between the red polarization direction and the surface normal, $\hat{n}$, for the $\perp$ grating configuration.

larger than that of the perpendicular orientation. Similar to the fine-pitched screw, the majority of the SHG enhancement in the parallel orientation is due to the lower surface second harmonic yield generated solely due to the interaction between the surface field and red pulse. Like the fine-pitched screw, the SHG yield is dramatically larger with the THz field present, which suggests some THz field enhancement could be present due to the sub-micron metallic features.

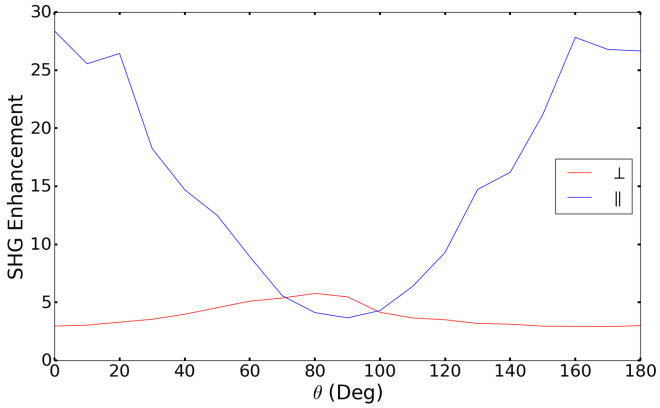

Figure C.19: SHG enhancement as a function of the θ, the angle between the red polarization direction and the surface normal, n, for both grating setups.

C.5 Comparing Quasi-static and THz field enhanced SHG

In Figure C.9, there were 2 clear instances (see arrows in Fig. C.9) where the SHG yield dipped below the baseline surface SHG yield, indicating (according to our expression for I_{400nm}, Eq. 47), $\mathbf{E}_{surf}$ and $\mathbf{E}_{THz}$ were anti-parallel. Given that Eq.47 implicitly treats the THz pulse as a quasi-static field relative to the time-scale of surface polarization charge dynamics, we explored the possibility of applying a true "quasi-static" field of known magnitude to a surface, and using the change in surface SHG yield as a method for calibrating the THz field strength as well as the effective characteristic surface field.

To this end, a high voltage 1μs pulse was created using a high voltage transformer. The high voltage pulse was applied across two parallel gold mirrors with $\approx$ a 2mm separation. The red pulse grazed off the surface of one of the mirrors and the second harmonic yield was measured as a function of the applied field strength. The SHG yield for quasi-static fields parallel and anti-parallel to the surface normal of the grazing mirror were recorded as a function of the field strength as shown in Figure C.20.

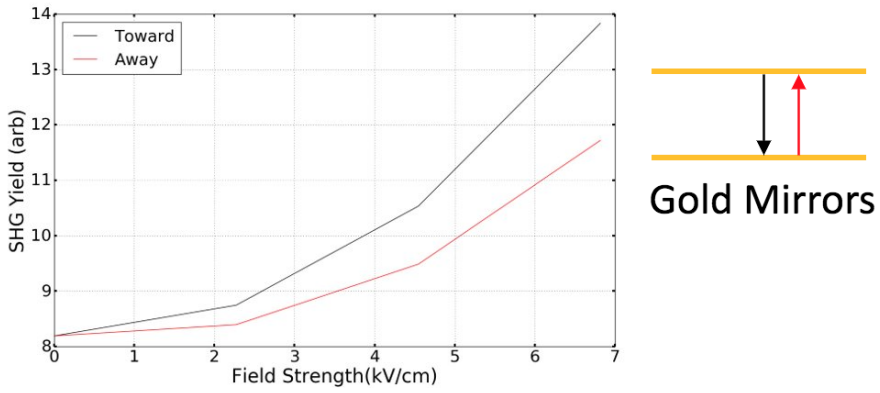

Figure C.20: Measured SHG yield as a function of quasi-static field strength for polarities toward (black) and away (red) from the grazing mirror surface. A cartoon of the field polarity relative to the grazing mirror surface is shown to the right of the graph. The arrows in the cartoon represent the polarity of the quasi-static field and are color coordinated with the respective colors in the plot legend.

Surprisingly, the suppression in the SHG yield observed during every other half-cycle in the presence of a THz pulse is absent with either polarity quasi-static field. The different results suggests that the time-scales for surface polarization dynamics are non-negligible on a ps time-scale and/or that our simple model of field

enhanced SHG is incorrect. The simple model of enhanced SHG is routinely adopted describing electric field induced second harmonic generation (EFISH)[70, 73]. Further experiments may be needed to better understand our observations and the limitations on our model of THz enhanced surface second harmonic generation.

References

[1]Z. Chang, *Fundamentals of attosecond optics* (CRC press, 2016).

[2]D. Pinkham and R. R. Jones, "Intense laser ionization of transiently aligned CO", Physical Review A **72**, 023418 (2005).

[3]I. V. Litvinyuk, K. F. Lee, P. W. Dooley, D. M. Rayner, D. M. Villeneuve, and P. B. Corkum, "Alignment-dependent strong field ionization of molecules", Physical Review Letters **90**, 233003 (2003).

[4]P. Sándor, A. Sissay, F. Mauger, P. M. Abanador, T. T. Gorman, T. D. Scarborough, M. B. Gaarde, K. Lopata, K. J. Schafer, and R. R. Jones, "Angle dependence of strong-field single and double ionization of carbonyl sulfide", Physical Review A **98**, 043425 (2018).

[5]J. L. Hansen, L. Holmegaard, J. H. Nielsen, H. Stapelfeldt, D. Dimitrovski, and L. B. Madsen, "Orientation-dependent ionization yields from strong-field ionization of fixed-in-space linear and asymmetric top molecules", Journal of Physics B: Atomic, Molecular and Optical Physics **45**, 015101 (2011).

[6]H. Stapelfeldt and T. Seideman, "Colloquium: aligning molecules with strong laser pulses", Reviews of Modern Physics **75**, 543 (2003).

[7]K. Egodapitiya, S. Li, and R. Jones, "Terahertz-induced field-free orientation of rotationally excited molecules", Physical Review Letters **112**, 103002 (2014).

[8]K. Sonoda, A. Iwasaki, K. Yamanouchi, and H. Hasegawa, "Field-free molecular orientation of nonadiabatically aligned OCS", Chemical Physics Letters **693**, 114–120 (2018).

[9]P. M. Kraus, A. Rupenyan, and H. J. Wörner, "High-harmonic spectroscopy of oriented ocs molecules: emission of even and odd harmonics", Physical Review Letters **109**, 233903 (2012).

[10]S. Fleischer, Y. Zhou, R. W. Field, and K. A. Nelson, "Molecular orientation and alignment by intense single-cycle THz pulses", Physical Review Letters **107**, 163603 (2011).

[11]K. J. Betsch, "Exploring ultrafast molecular dynamics in asymmetric laser fields", PhD Thesis, University of Virginia (2011).

[12]S. Li, "Field ionization and field emission with intense single-cycle thz pulses", PhD Thesis, University of Virginia (2016).

[13]G. Voronov and N. B. Delone, "Ionization of the xenon atom by the electric field of ruby laser emission", Soviet Journal of Experimental and Theoretical Physics Letters **1**, 66 (1965).

[14]L. Keldysh, Soviet Phys. JETP 2354 (1965).

[15]P. B. Corkum, "Plasma perspective on strong field multiphoton ionization", Physical Review Letters **71**, 1994 (1993).

[16]A. I. Kuleff and L. S. Cederbaum, "Ultrafast correlation-driven electron dynamics", Journal of Physics B: Atomic, Molecular and Optical Physics **47**, 124002 (2014).

[17]K. Schafer, B. Yang, L. DiMauro, and K. Kulander, "Above threshold ionization beyond the high harmonic cutoff", Physical Review Letters **70**, 1599 (1993).

[18]M. Ferray, A. L'Huillier, X. Li, L. Lompre, G. Mainfray, and C. Manus, "Multiple-harmonic conversion of 1064 nm radiation in rare gases", Journal of Physics B: Atomic, Molecular and Optical Physics **21**, L31 (1988).

[19]M. Lewenstein, P. Balcou, M. Y. Ivanov, A. L'huillier, and P. B. Corkum, "Theory of high-harmonic generation by low-frequency laser fields", Physical Review A **49**, 2117 (1994).

[20]F. Calegari, A. Trabattoni, A. Palacios, D. Ayuso, M. C. Castrovilli, J. B. Greenwood, P. Decleva, F. Martın, and M. Nisoli, "Charge migration induced by attosecond pulses in bio-relevant molecules", Journal of Physics B: Atomic, Molecular and Optical Physics **49**, 142001 (2016).

[21]P. M. Kraus, B. Mignolet, D. Baykusheva, A. Rupenyan, L. Horn, E. F. Penka, G. Grassi, O. I. Tolstikhin, J. Schneider, F. Jensen, et al., "Measurement and laser control of attosecond charge migration in ionized iodoacetylene", Science **350**, 790–795 (2015).

[22]S. Folorunso et al., Unpublished (2021).

[23]P. Sándor, A. Sissay, F. Mauger, M. W. Gordon, T. Gorman, T. Scarborough, M. B. Gaarde, K. Lopata, K. Schafer, and R. Jones, "Angle-dependent strong-field ionization of halomethanes", The Journal of chemical physics **151**, 194308 (2019).

[24]X.-M. Tong, Z. Zhao, and C.-D. Lin, "Theory of molecular tunneling ionization", Physical Review A **66**, 033402 (2002).

[25]D. Pavičić, K. F. Lee, D. M. Rayner, P. B. Corkum, and D. M. Villeneuve, "Direct measurement of the angular dependence of ionization for N_2, O_2, and CO_2 in intense laser fields", Physical Review Letters **98**, 243001 (2007).

[26]E. P. Fowe and A. D. Bandrauk, "Nonperturbative time-dependent density-functional theory of ionization and harmonic generation in OCS and CS_2 molecules with ultrashort intense laser pulses: Intensity and orientational effects", Physical Review A **84**, 035402 (2011).

[27]L. B. Madsen, F. Jensen, O. I. Tolstikhin, and T. Morishita, "Structure factors for tunneling ionization rates of molecules", Physical Review A **87**, 013406 (2013).

[28]A. Russakoff, S. Bubin, X. Xie, S. Erattupuzha, M. Kitzler, and K. Varga, "Time-dependent density-functional study of the alignment-dependent ionization of acetylene and ethylene by strong laser pulses", Physical Review A **91**, 023422 (2015).

[29]S. G. Walt, N. Bhargava Ram, A. von Conta, O. I. Tolstikhin, L. B. Madsen, F. Jensen, and H. J. Wörner, "Role of multi-electron effects in the asymmetry of strong-field ionization and fragmentation of polar molecules: the methyl halide series", The Journal of Physical Chemistry A **119**, 11772–11782 (2015).

[30]R. Johansen, K. G. Bay, L. Christensen, J. Thøgersen, D. Dimitrovski, L. B. Madsen, and H. Stapelfeldt, "Alignment-dependent strong-field ionization yields of carbonyl sulfide molecules induced by mid-infrared laser pulses", Journal of Physics B: Atomic, Molecular and Optical Physics **49**, 205601 (2016).

[31]V. Makhija, X. Ren, D. Gockel, A.-T. Le, and V. Kumarappan, "Orientation resolution through rotational coherence spectroscopy", arXiv preprint arXiv:1611.06476 (2016).

[32]D. Dimitrovski, M. Abu-Samha, L. B. Madsen, F. Filsinger, G. Meijer, J. Küpper, L. Holmegaard, L. Kalhøj, J. H. Nielsen, and H. Stapelfeldt, "Ionization of oriented carbonyl sulfide molecules by intense circularly polarized laser pulses", Physical Review A **83**, 023405 (2011).

[33]M. Spanner, S. Patchkovskii, E. Frumker, and P. Corkum, "Mechanisms of two-color laser-induced field-free molecular orientation", Physical Review Letters **109**, 113001 (2012).

[34]M. J. Vrakking and S. Stolte, "Coherent control of molecular orientation", Chemical Physics Letters **271**, 209–215 (1997).

[35]G. Herzberg, *The spectra and structures of simple free radicals: an introduction to molecular spectroscopy* (Courier Corporation, 1988).

[36]R. Weinkauf and U. Boesl, "Laser spectroscopy of molecular ions: The A–X transition in the OCS radical cation", The Journal of Chemical Physics **101**, 8482–8493 (1994).

[37]S. Stimson et al., "High resolution vacuum ultraviolet pulsed field ionization photoelectron band for OCS+(X $^2\Pi$): An experimental and theoretical study", The Journal of chemical physics **108**, 6205–6214 (1998).

[38]R. N. Zare and W. G. Harter, "Angular momentum: understanding spatial aspects in chemistry and physics", Wiley, New York (1988).

[39]R. Tehini et al., "Field-free molecular orientation of $^1\Sigma$ and $^2\Pi$ molecules at high temperature.", Physical Review A **85**, 043423 (2012).

[40]A. Meijer, Y. Zhang, D. Parker, W. Van der Zande, A. Gijsbertsen, and M. Vrakking, "Controlling rotational state distributions using two-pulse stimulated raman excitation", Physical Review A **76**, 023411 (2007).

[41]D. Pinkham, "Ultrafast control of the dynamics of diatomic molecules", PhD Thesis, University of Virginia (2008).

[42]P. M. Kraus, D. Baykusheva, and H. J. Wörner, "Two-pulse orientation dynamics and high-harmonic spectroscopy of strongly-oriented molecules", Journal of Physics B: Atomic, Molecular and Optical Physics **47**, 124030 (2014).

[43]T. Zuo and A. D. Bandrauk, "Charge-resonance-enhanced ionization of diatomic molecular ions by intense lasers", Physical Review A **52**, R2511 (1995).

[44]D. Strickland and G. Mourou, "Compression of amplified chirped optical pulses", Optics communications **55**, 447–449 (1985).

[45]K. Labs, "Model mts mini ti:sapphire laser kit", Instruction Manual (2001).

[46]S. Backus, C. G. Durfee, G. Mourou, H. C. Kapteyn, and M. M. Murnane, "0.2-tw laser system at 1 khz", Optics letters **22**, 1256–1258 (1997).

[47]R. Trebino, "Frequency-resolved optical gating: the measurement of ultrashort laser pulses", Springer Science Business Media (2012).

[48]G. Vacuum, "25s ion pump instruction manual", (2008).

[49]V. V. Technologies, "Sentorr gauge controller instruction manual", (1997).

[50]V. V. Technologies, "580 nude ionization gauge instruction manual", (1999).

[51]F. Dunning and R. Hulet, "Atomic,molecular, and optical physics: atoms and molecules", Academic Press (1996).

[52]U. E. et al, "Cooling of large molecules below 1 K and He clusters formation.", The Journal of Chemical Physics **112**, 8068–8071 (2000).

[53]G. Ondrey, S. Kanfer, and R. Bersohn, "The collinear photodissociation of OCS at 157 nm", The Journal of Chemical Physics **79**, 179–184 (1983).

[54]G. Ghosh, "Dispersion-equation coefficients for the refractive index and birefringence of calcite and quartz crystals", Optics communications **163**, 95–102 (1999).

[55]*Retardance curves at 400 and 800 nm*, https://www.newlightphotonics.com/Ultrafast-Components-and-Kits/Ultrathin-Dual-Wavelength-Waveplates, Accessed: 2022-05-04.

[56]K. Betsch, D. Pinkham, and R. Jones, "Directional emission of multiply charged ions during dissociative ionization in asymmetric two-color laser fields", Physical Review Letters **105**, 223002 (2010).

[57]J. Wu, A. Vredenborg, L. P. H. Schmidt, T. Jahnke, A. Czasch, and R. Dörner, "Comparison of dissociative ionization of H_2, N_2,Ar_2, and CO by elliptically polarized two-color pulses", Physical Review A **87**, 023406 (2013).

[58]C. Guo, M. Li, J. P. Nibarger, and G. N. Gibson, "Single and double ionization of diatomic molecules in strong laser fields", Physical Review A **58**, R4271 (1998).

[59]T. Seideman, M. Y. Ivanov, and P. B. Corkum, "Role of electron localization in intense-field molecular ionization", Physical review letters **75**, 2819 (1995).

[60]F. J. Lovas, "Microwave spectral tables ii. triatomic molecules", Journal of Physical and Chemical Reference Data **7**, 1445–1750 (1978).

[61]G. Maroulis and M. Menadakis, "Polarizability and hyperpolarizability of COS and NNO", Chemical Physics Letters **494**, 144–149 (2010).

[62]P. Bevington and D. Robinson, "Data reduction and error analysis for the physical sciences", McGraw-Hill New York (1969).

[63]R. R. Jones, "Exploiting coherences to probe strong-field molecular ionization dynamics", Division of Atomic Molecular and Optical Physics (2021).

[64]Y. Nakashima, K. Harada, K. Tanaka, and T. Tanaka, "High-resolution Fourier transform emission spectroscopy of the A-$^2\Pi$ X- $^2\Pi$ band of the OCS^+ ion", The Journal of Chemical Physics **146**, 144302 (2017).

[65]E. Gershnabel, I. S. Averbukh, and R. J. Gordon, "Enhanced molecular orientation induced by molecular antialignment", Physical Review A **74**, 053414 (2006).

[66]S. Thomas, M. Krüger, M. Förster, M. Schenk, and P. Hommelhoff, "Probing of optical near-fields by electron rescattering on the 1 nm scale", Nano letters **13**, 4790–4794 (2013).

[67]S. Li and R. Jones, "High-energy electron emission from metallic nano-tips driven by intense single-cycle terahertz pulses", Nature Communications **7**, 1–7 (2016).

[68]R. Miller, Y. Y. Lau, and J. H. Booske, "Electric field distribution on knife-edge field emitters", Applied Physics Letters **91**, 074105 (2007).

[69]J. Hebling, G. Almasi, I. Z. Kozma, and J. Kuhl, "Velocity matching by pulse front tilting for large-area thz-pulse generation", Optics Express **10**, 1161–1166 (2002).

[70]R. Terhune, P. Maker, and C. Savage, "Optical harmonic generation in calcite", Physical Review Letters **8**, 404 (1962).

[71]M. Reid, I. V. Cravetchi, and R. Fedosejevs, "Terahertz radiation and second-harmonic generation from inas: bulk versus surface electric-field-induced contributions", Physical Review B **72**, 035201 (2005).

[72]R. M. Corn and D. A. Higgins, "Optical second harmonic generation as a probe of surface chemistry", Chemical reviews **94**, 107–125 (1994).

[73]H. G. de Chatellus and E. Freysz, "Measurement of the third-order susceptibility of glasses by efish of femtosecond pulses", Optics Express **9**, 586–591 (2001).